IUSS
Scuola Universitaria Superiore Pavia

Istituto Universitario degli Studi Superiori di Pavia

Facoltà di Ingegneria

An automatic tool for thoracic aorta segmentation and 3D geometric analysis

A Thesis submitted in Fulfilment of the Requirements

for the Degree of Doctor in Philosophy in

Computational Mechanics and Advanced Materials

at Istituto Universitario degli Studi Superiori di Pavia, Italy

Supervisor: Professor

Ferdinando Auricchio

Co - supervisor: Author:

Elena Faggiano   **Chiara Trentin**

Michele Conti

Academic year 2014/2015

XXVIII PhD Course

A te

Anknowledgments

Three years ago I arrived in Pavia for the first time and the first impression was of loneliness. But soon the comp-mech group made me feel at home. I would like to thank everyone for the constructive conversations and the nice moments especially in front of sweets. First, I would like to thank my Supervisor, Prof. Ferdinando Auricchio, for the given opportunity to study in this group, where I increased my skills and knowledges, for his great guidance and professional support in the development of this thesis. I would like to thank Elena that since her first arrival helped and supported me with her precious advises, even though we know form such a small time I feel her more like a friend than a colleque/supervisor. I would like to thank Michele for his support for this research study.

I have greatly appreciated the discussions with the doctord and PhD students coming from the University Medical Center of Utrecht; I acknowl- edge their helpful clarifications and useful comments.

Then, I thank all my lab-mates for their friendship: Andrea, Giuseppe, Adrien, Josef, Simone, Mauro, Eli, Elisa, Alessandro, Marco, Paolo, Giulia, Marco, Rodrigo, Valentina, and Xi. Special thanks to my colleagues, Anna, Carolina, and Isabella for their nice conversations and friendship.

My deepest thanks go to my parents and my sister Anna, for their constant encouragement to improve and step forward.

Last but not least, I would like to thank Stefano for his constant defusing and smile.

II

Abstract

The impact of thoracic endovascular aortic repair (TEVAR) on the dynamic aortic environment remains unclear. In fact the introduction of a rigid metallic stent-graft into an elastic vessel exposed to high dynamic and cyclic loads can produce variation in the usual behaviour of the aorta and such a behaviour deserves to be investigated in a deep and exhaustive manner.

The aim of this thesis is therefore to supply an automatic tool, tailored on the thoracic aorta, to segment and geometrically analyse the vessel, trying to deepen the knowledge in the field of aortic dynamic changes particularly in the presence of thoracic aortic pathologies treated with TEVAR. The workflow to achieve our goal is mainly composed by three subsequent steps: segmentation, automatic identification of section of interest, and vessel geometric quantification through the computation of static and dynamic measures.

In detail chapter one will introduce the anatomy and the physiology of the thoracic aorta along with the main aortic pathologies and the recent surgical treatments.

Chapter two will focus on providing a summary of the literature concerning the morphological characterization of vascular networks exploiting both static and dynamic medical images.

Chapter three will describe the implemented pipeline used to pre-process and segment the images of our target dataset made up of 4D-CTA computed tomographic angiography of the thoracic aorta pre- and post-TEVAR. The method is based on a custom modification of the level set method and the colliding front initialisation, in order to let the thoracic aorta be segmented in one goal.

Chapter four is the core of this work and it describes the automatic tool to geometrically quantify the aortic dynamic changes. Sections and regions of particular clinical interest are automatically identified exploiting the concept of centerline and quantitative indexes related to sections and regions of interest such as: area, diameter and length are computed, these geometrical quantities are tracked to analyse the changes experienced by the aorta during an entire hearth cycle.

Chapter five shows the results obtained using the automatic tool on two type of dataset one composed of aneurysmatic patients and the other composed of dissected patients plus a healthy control case.

Appendix A contains a side work, the aim of this work is to reproduce a virtual TEVAR procedure based on pre-operative images and to validate this procedure through a computational fluid dynamics study.

Appendix B simply summarizes a series of definition of indexes used in the geometry quantification approach.

Contents

List of Tables

List of Figures

Chapter 1

Introduction

1.1   Aorta anatomy, physiology and pathology

The aorta is a large conductance blood vessel, often called the greatest artery, normally reaching $70\,cm$ in length and $3.5\,cm$ in diameter. It arises from the heart, arches anterocranially and then posterocaudally, and descends caudally, terminating as it bifurcates into the right and left common iliac arteries. Arises from the description just given that the aorta is a complex and dynamic environment, which is deeply affected by the hearth related cyclic changes.

The aorta is divided into six segments:

- the aortic root,

- the sinotubular junction,

- the ascending aorta,

- the aortic arch,

- the isthmus and descending thoracic aorta,

- the abdominal aorta.

1.1.1   The aortic root

The aortic root originates at the aortic valve annulus level and extends to the sinotubular junction, the sinuses of Valsalva, see figure 1.1, the aortic root is highlighted in a light blue color. The aortic root is intrapericardial and consists of three round dilatations (sinuses of Valsalva), that allow aortic valve leaflets to open up to 90° degrees. Normal diameter of the aortic root is $2.9 \pm 0.4\,cm$, with a variation depending on body size. The most common consequence of disease of the aortic
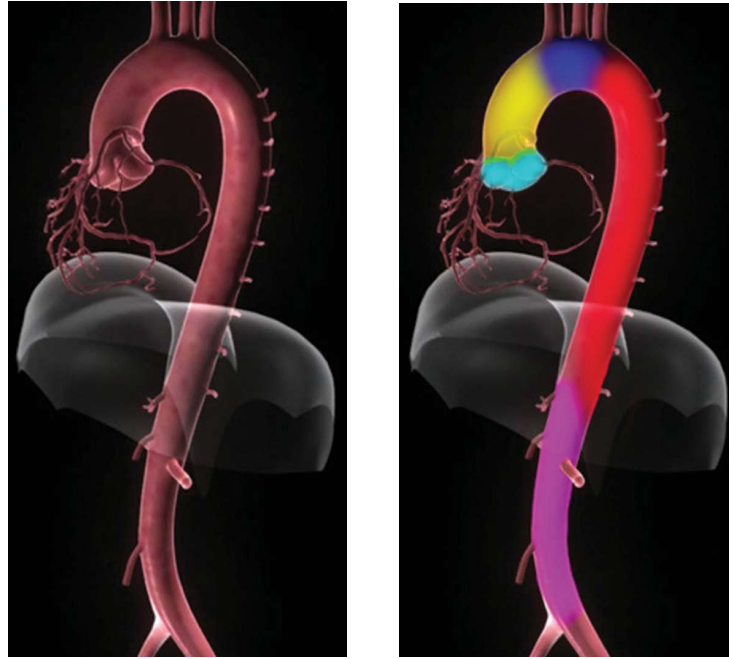
Figure 1.1: On the left side is represented a graphic depiction of the aorta. On the right side is depicted a segmental division of the aorta: the aortic root (LIGHT BLUE), the sinotubular junction (GREEN), the ascending aorta (YELLOW), the aortic arch (DARK BLUE), the isthmus and descending (thoracic) aorta (RED), and the abdominal aorta (PINK).

root is impairment of the valve; in fact dilation of the root reduces coaptation and an event like dissection reduces the suspension of the leaflets and lead to prolapse. From the aortic root branches the left and right coronary arteries.

1.1.2 The sinotubular junction

The sinotubular junction is normally a well-defined region at which the rounded and wider sinuses of Valsalva join the narrower tubule-shaped ascending aorta, see figure 1.1, the sinotubular junction is highlighted in green color. Normally, the sinotubular junction has the same dimension as the aortic annulus and constitutes a critical support to the superior part of the aortic valve commissures. Normal diameter of the sinotubular junction is $2.6\pm0.3\,cm$, with variation depending on body size. Effacement (marked dilation) of this junction suggests annuloaortic ectasia and often is seen in patients with Marfan syndrome. Loss of support of the commissure leads to leaflet prolapse. Dilation of the sinotubular junction confounds the correct spatial arrangement of the commissures and typically results in central malcoaptation and aortic insufficiency. Replacement of an aneurysmal ascending aorta and sinotubular junction with a tube graft of correct diameter often corrects aortic insufficiency by reestablishing the correct spatial suspension of the aortic valve. Similarly, reestablishing integrity of a dissected sinotubular junction by sewing the dissected root
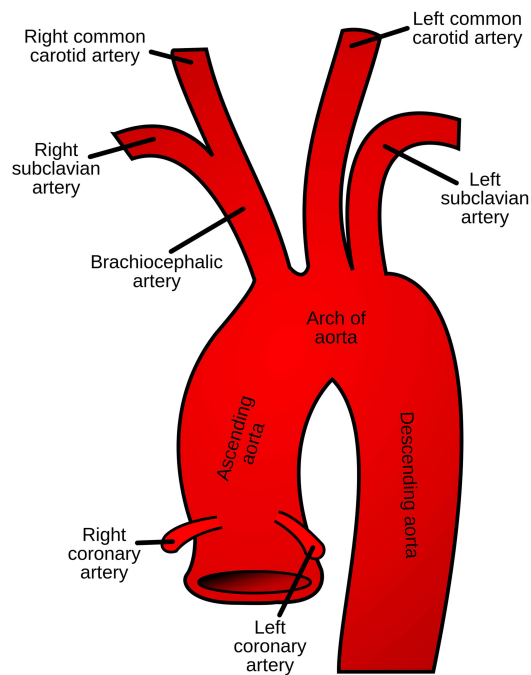
Figure 1.2: The thoracic aorta. In this picture are emphasized the three supra-aortic branches - i.e., the brachiocephalic trunk, the left common carotid artery, and left subclavian artery. The figure shows also the coronary arteries (left and right coronary arteries). Those arteries are responsible to carry the oxygenated blood to the heart.
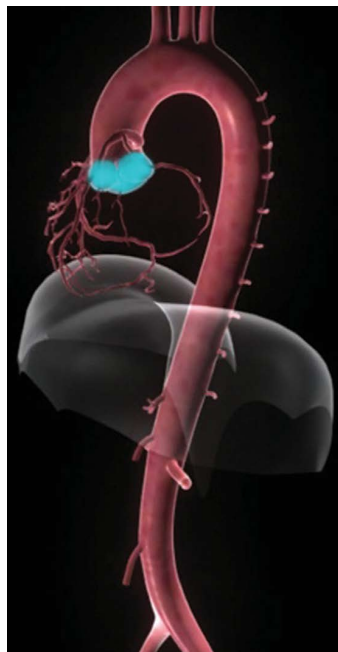
Figure 1.3: The aortic root.

components to a tube graft that supplies support to the repaired sinotubular junction may also correct aortic insufficiency from an aortic dissection.

Figure 1.4: The sinotubular junction highlighted with a green line.

1.1.3 The ascending aorta

The ascending aorta is the segment of the aorta from the sinotubular junction to the first great arch vessel, the brachiocephalic artery. See figure 1.1 where the ascending aorta is highlighted in yellow color. Identifying the distinction of the ascending aorta from the arch on the outside region is far easier than it is on the inside part of the aorta. The ascending aorta is often affected by dissections and aneurysms, it is intrapericardial, as the pericardium reaches distally the first supra-aortic vessel, see figure 1.2. The ascending aorta measures approximately $5\,cm$ in length and up to $2.6 \pm 0.3\,cm$ in diameter, with variation appropriate for body size.

1.1.4 The aortic arch

The aortic arch is the portion of the aorta from the first supra-aortic vessel (i.e., the brachiocephalic artery) to the left subclavian artery ostium. See figure 1.1 where the aortic arch is highlighted in a dark blue color. The aortic arch is mostly extrapericardial; normal diameter of the aortic arch is $2.5 \pm 0.2\,cm$, with variation appropriate for body size. The arch arcs over the right pulmonary artery, the left mainstem bronchus, the left recurrent laryngeal nerve, and the roof of the left atrium. Branch vessels include right brachiocephalic artery (right subclavian artery and right common carotid artery), left carotid artery, and left subclavian artery. Aortic arch branch variations are common.

1.1.5   The isthmus and descending thoracic aorta

The isthmus is the narrower portion of the aorta (by approximately $3\,mm$) between the left subclavian artery and ligamentum arteriosus, a remnant of the ductus arteriosus. Blunt traumatic deceleration injury, resulting in transection to the aorta often occurs at this site. The descending thoracic aorta begins at the ligamentum arteriosus and continues to the level of the diaphragm. In figure 1.1 the descending aorta is highlighted in red color. The esophagus runs alongside (within $0.5\,cm$) the descending aorta. Normal diameter of the descending proximal aorta is $3.0\,cm$. At the eleventh rib level, it is inferior to $2.3\,cm$. Branch vessels of the isthmus include the ductus arteriosus. Branch vessels of the descending aorta include intercostal arteries, spinal arteries, and bronchial arteries.

1.1.6   The abdominal aorta

The abdominal aorta starts at the hiatus of the diaphragm and courses retroperitoneal to its bifurcation, see figure 1.1 pink color highlight the abdominal aorta. Major branch vessels include inferior phrenic arteries, celiac artery branches, renal arteries, superior mesenteric artery, inferior mesenteric artery, lumbar and spinal arteries, and iliac arteries. Normal diameter of the suprarenal abdominal aorta is $2.0\,cm$, and normal diameter of the infrarenal abdominal aorta is inferior to $2.0\,cm$. From a practical point of view the abdominal aorta is reasonably equal to the size of the patient's thumb.

1.2   Histology of the aorta

The basic components of the aortic wall are intima, media, and adventitia.

1.2.1   The intima

Tunica intima is the layer at contact with the blood and it is made of a single layer of endothelial cells embedded in extracellular matrix and an underlying thin basal lamina, which is also referred to as basement membrane, providing structural support to the arterial wall. Such a layer provides a non-thrombogenic surface so that the blood can flow through the artery without forming thrombus. The basal lamina contains non-fibrillar collagen types, adhesion molecules laminin, fibronectin, and other extracellular matrix molecules. It has been observed that the orientation of the collagen fibers in the subendothelial layer through the thickness it is not uniform but dispersed. The intima is very thin, i.e., from 0.05 to $0.1\,mm$, and its contribution to the mechanical properties in healthy young human arteries is not significant. Whereas, ageing and in the case of pathological conditions, the intima becomes thicker (from 0.2 to $0.4\,mm$) and stiffer, and develops a more
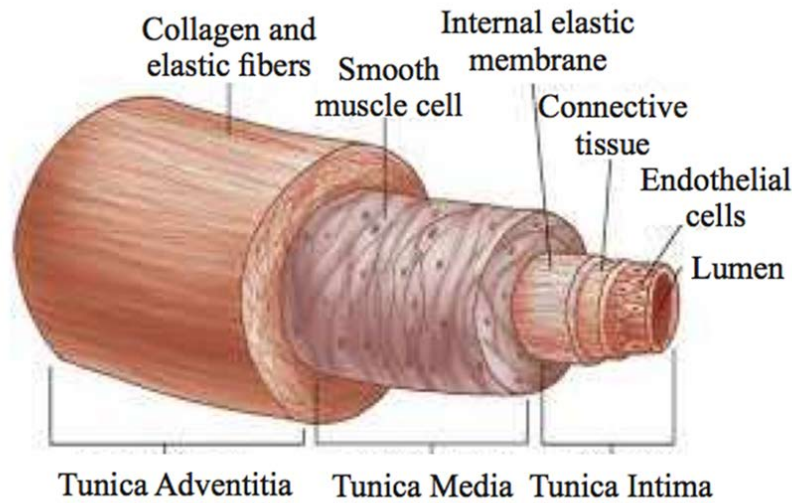
Figure 1.5: Structural organization and composition of the three different layers in the coronary vessel wall.

complex and heterogeneous structure. These pathological changes are associated with alterations in the mechanical properties, which differ significantly from those of healthy arteries. Finally, it is separated from the media by the internal elastic lamina, which is often considered to be part of it.

1.2.2   The media

Tunica media is the middle and thickest layer of the artery, i.e, from 0.1 to 0.5 mm, made of smooth muscle cells, elastin and collagen immersed into an aqueous ground substance containing proteoglycans, known as matrix. Such fibers are arranged in repetitive lamellar units separated by thin fenestrated sheets of elastin, forming concentric medial layers. The thickness of such units is nearly independent of the radial location across the wall, but their number decrease as the distance from the heart increases, so that the lamellar units found absent in small muscular arteries. The laminated structure confers high strength to the media and explains how such a layer determines the mechanical properties of the whole vessel wall. In the media, collagen fibers are aligned along the circumferential direction with a very little dispersion. This structural arrangement gives the media the ability to carry loads in the circumferential direction. Apparently, the distribution of collagen does not show changes in atherosclerotic arteries. The media is separated from the adventitia by the external elastic lamina.

1.2.3 The adventitia

Tunica adventitia is the outermost layer of the artery and consists primarily of collagen fibers, elastin, nerves, fibroblasts, fibrocytes. The thickness size of the adventitia is thinner than the media, i.e., from 0.25 to $0.40\,mm$. The adventitia is surrounded continuously by loose connective tissue, which often provides additional structural support. As for the intima, histological evidence have proven the dispersion of collagen fibers in the adventitial layer, which remains also in atherosclerotic arteries. Collagen fibers tend to maintain an axial orientation and remain slack at low pressures, but as the pressure increases they straightened, reinforcing the arterial wall and preventing the over-stretching and the rupture of the artery. The cardiovascular diseases are being addressed, as appropriate, through the prevention of risk factors, drug therapy and finally surgery.

1.3 Aortic pathologies

Acute aortic dissections, rupturing aneurysms, rupturing pseudoaneurysms, and the variants of intramural hematomas and penetrating ulcers of the aortic wall are all acute aortic syndromes. There is some potential overlap among them—an intramural hematoma may evolve into an acute aortic dissection, an aneurysm may dissect, a penetrating ulcer may lead to an intramural hematoma or to rupture. In the following we will introduce the aortic pathologies that we have studied in this dissertation and describe them in detail.

1.3.1 The dissection

Aortic dissection is a tearing through the intima into the aortic wall (intimal tear), figure 1.6, with entry of luminal blood into the wall, resulting in the formation of a false lumen partitioned from the true lumen by the intimal flap, figure 1.6. Acute aortic dissection is an aortic dissection occurring less than 2 weeks since the attributable pain episode.

Classification

There are several classifications of acute aortic dissection (AAD) based on where the disease develops. None is perfect, and all introduce some confusion and apply poorly in some cases. The Stanford classification emphasizes whether or not there is involvement by the flap of the ascending aorta. The logic of the classification is its simplicity and the ability of diagnostic testing to identify the presence or absence of a flap in the ascending aorta (which has the highest risk and is surgically treated). The intimal flap is the easiest component of an AAD to image, much easier than the intimal tear. The Stanford classification uses the location of the flap, which can be imaged by all imaging modalities, rather than the tear, which is less successfully imaged. Therefore, the
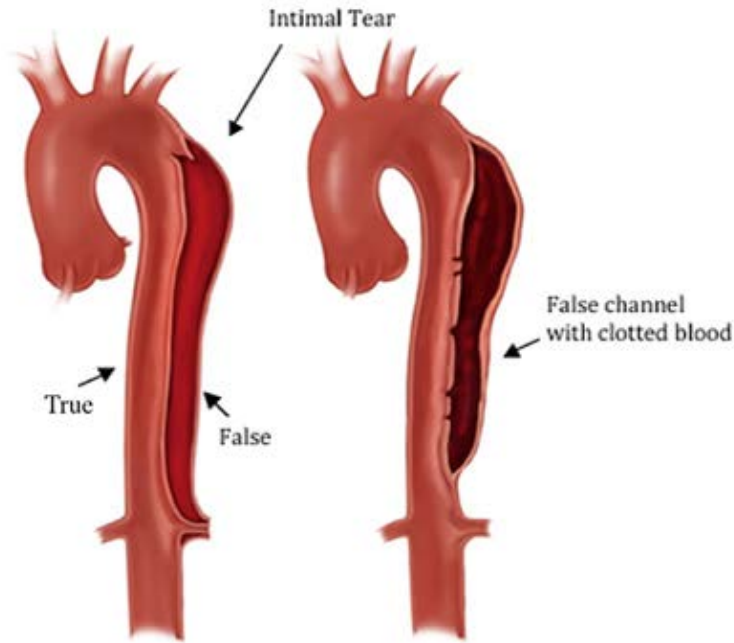
Figure 1.6: In figure is depicted an example of aortic dissection of the descending aorta. The picture highlights the entry tear, where the false lumen originates (left side) and the formation of a false and a true lumen after dissection has developed. In the false lumen the blood tends to clot as depicted in figure (right side).

Stanford classification's popularity and success are based on simple and generally quite reliable issues, as flaps are easily imaged. Stanford type A includes all dissections involving the ascending aorta, regardless of site of origin or the location of the intimal tear. Stanford type B includes all dissections not involving the ascending aorta

Type A patients are more likely to be younger than type B patients (average age, 60 years versus 70 years) and have a predisposing congenital (bicuspid aortic valve), hereditary (Marfan syndrome), or inflammatory (giant cell aortitis or Takayasu's aortitis) condition. Type A patients are less likely to have a history of hypertension than are type B patients (30% versus 71%).

Disease progression

The mortality related to AAD is a consequence of complications. Complications such as rupture, tamponade, acute aortic insufficiency (AI), and myocardial ischemia confer hemodynamic instability, which remains the dominant predictor of untreated and surgical mortality. Early diagnosis of and surgery for type A AAD is critical to avoid hemodynamic instability. Complications confer high risk and must be identified to manage cases appropriately: proximal AAD with complications must be considered for a hastened surgical repair; distal AAD cases with complications should be considered for prompt surgical (and potentially endovascular) repair, rather than ongoing medical management. Rupture is a dreaded occurrence with any form of aortic dissection. As both
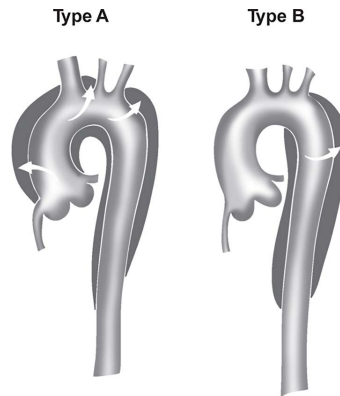
Figure 1.7: The Stanford classification of aortic dissection. Stanford type A includes aortic dissections that involve the ascending aorta (with or without involvement of the transverse and descending thoracic aorta. Stanford type B includes aortic dissections that originate in the descending (and thoracoabdominal) aorta, regardless of any retrograde involvement of the arch.
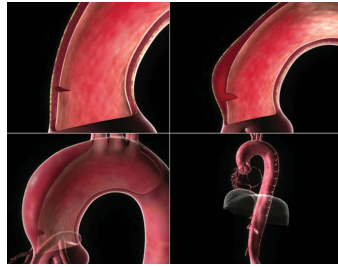
Figure 1.8: Type A AAD pathogenesis. The most common form of AAD originates in the aortic root; typically, a tear develops 2 cm above the right cusp of the aortic valve on the outside curvature of the aorta and allows entry of luminal blood into the wall, with formation and propagation of a false lumen that cleaves between concentric layers of elastin sheets, distally down to the aortic bifurcation, usually into the common iliac artery. The intimal flap is typically very mobile.
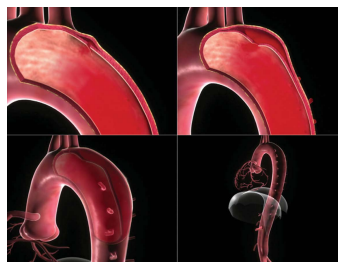
Figure 1.9: Type B AAD pathogenesis. The second most common form of AAD originates in the descending aorta; typically, a tear develops a few centimeters distal to the left subclavian artery origin and allows entry of luminal blood into the wall, with formation and propagation of a false lumen, usually down to the aortic bifurcation. The false lumen typically extends retrograde only a few centimeters to the left subclavian artery ostium. The intimal flap is typically very mobile.

proximal and distal dissection is likely to extend distally to the aorto-iliac bifurcation. Type A (proximal) AAD is more likely to become complicated and exposes the heart to the development

of life-threatening complications.

Incidence and mortality

Acute aortic dissection (AAD) is the most common catastrophic aortic disease. The estimated prevalence is 10 to 30 per million per year, greater than for any other disease of the aorta and twice that of abdominal aortic aneurysm rupture. Most cases involve people older than 40 years, typically with a background of hypertension.

Complication are likely to arise and their incidence is approximately equal between type A and type B AAD.

Mortality rate is high for aortic dissection. Even though the predominance is male, AAD in women has a higher mortality rate, operated on or unoperated on. Seven percent of AAD cases occur in persons younger than 40 years without gender predominance and are typically related to hereditary conditions (e.g., Marfan syndrome), congenital causes (e.g., bicuspid aortic valve), prior cardiac or aortic surgery, enlarged aorta, or pregnancy. Mortality among AAD patients younger than 40 years is comparable to that among patients older than 40 years. Encouragingly, the mortality from AAD has fallen by half during the last 20 years.

1.3.2   Thoracic and abdominal aortic aneurysm

An aneurysm or aneurism (from Greek words aneurysma - i.e., dilation - , and aneurynein - i.e., to dilate) is a localized, blood-filled balloon-like bulge in the wall of a blood vessel, see figure 1.10. Aneurysms can occur in any blood vessel, with examples including aneurysms of the circle of Willis in the brain, aortic aneurysms affecting the thoracic aorta, and abdominal aortic aneurysms. Aneurysms can also occur within the heart itself. Thoracic and abdominal aortic aneurysms, defined as more than 50% increase in aortic diameter, involve many permutations of location, length, morphology, branch vessel involvement, and complications.

Classification

Aneurysms are classified based on their position and shape.

Concerning position we can encounter thoracic aortic aneurysm - i.e., TAA - and abdominal aortic aneurysms - i.e., AAA. These aneurysms are located respectively in the region of the thoracic aorta (TAA) or in the region of the abdominal aorta (AAA).

The range of anatomic appearance begets the use of morphologic descriptive terms. The term tubular is used to describe a long length of aorta with all parts dilated similarly. The term fusiform describes a tapered beginning and end to the spindle-shaped dilated segment, with circumferential dilation. Saccular aneurysm describes a localized, shorter, round dilation. Thoracoabdominal
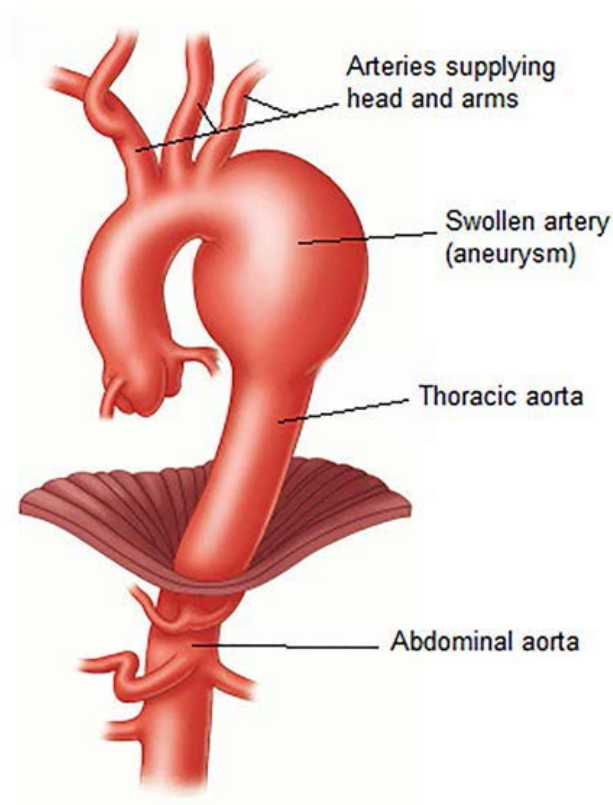
Figure 1.10: Thoracic or thoraco-abdominal aneurysm (TAA or TAAA). TAA are dilation of the thoracic aortic vessel similar to the more common abdominal aortic aneurysm. TAA and TAAA can get progressively larger, and if big enough, rupture with high risk of bleeding and subsequent hypovolemic shock, leading to death.

aneurysm describes an aneurysm extending across the diaphragm. These terms have more utility for recognition and planning of intervention than they do for establishing etiology. Many aneurysms are so complex, atypical, or extensive that they are not well described by any single term.

Disease progression

The natural history of aortic aneurysm is influenced by aneurysm size (diameter), rate of expansion, location, complications (aortic insufficiency, rupture, dissection, thrombosis), associated factors (bicuspid aortic valves, concurrent hypertension, smoking), and underlying causes (Marfan syndrome, Ehlers-Danlos syndrome, infection, inflammation, or atherosclerosis).

Potential complications of aortic aneurysm include rupture into an adjacent space (pericardial space, mediastinum, left pleural space, or retroperitoneum), into a cardiac cavity (fistula), into an adjacent vessel (pulmonary artery or inferior vena cava), or into another space (trachea); dissection; embolism of thrombus; compression of an adjacent structure, such as bronchus, bone, or recurrent laryngeal nerve; and distortion of the aortic valve and secondary aortic insufficiency

(sinus of Valsalva aneurysms, aortic root aneurysms, annuloaortic ectasia).

The yearly complication rate is influenced by thoracic aneurysm diameter. Assessment of aneurysm size by different modalities (echocardiography, transesophageal echocardiography [TEE], computed tomography [CT], magnetic resonance imaging [MRI]) may yield differences. There is invariably some degree of interobserver and intraobserver variation for each modality of testing, as evidenced by a reduction in size on follow-up testing. Sizing of aneurysms with respect to operative threshold applies only to asymptomatic aneurysms, not to symptomatic aneurysms. Aneurysms grow progressively at an approximate average overall rate of $1.2\,mm/year$. Larger aneurysms expand faster than smaller ones, the descending aorta expands faster ($0.19\,cm/year$) than the ascending aorta ($0.07\,cm/year$), and the abdominal aorta expands the fastest ($3.9\pm3.2\,mm/year$). Therefore, it is only an issue of time before aneurysms achieve a size of clinical risk.

Surgery for a thoracic aortic aneurysm is planned based on many factors. These include location of the aneurysm, such as the ascending or descending part of the aorta, the size of the aneurysm - i.e., repair might be recommended if an aneurysm is 5.5 to $6.0\,cm$ in diameter -, whether the aneurysm is part of a genetic problem, such as Marfan's syndrome, and whether the patient needs another heart surgery such as a heart valve replacement surgery. Open surgery and the less invasive procedure, called endovascular repair, are the two options for repairing a thoracic aortic aneurysm. The choice of repair can depend on the size and location of the aneurysm, but also on the patient age and clinical history.

Incidence and mortality

The true incidence of aneurysms of the thoracic aorta is unknown because of under-detection, but it is estimated to be 60 to 100 million. The mean age at diagnosis is 59 to 69 years. There is male gender predominance, with a ratio of two male for one female. The arch segment is less commonly involved (10%) and the ascending aorta is slightly more frequently involved than is the descending segment (40%). Abdominal aortic aneurysm remains an underdetected lesion of enormous cost in morbidity, mortality, and finance. AAA is the tenth leading cause of death in adult men. About 15.000 deaths per year in the United States are recognized to be due to AAA; the true number is higher because prehospital, often sudden death is often not accounted for. Although elective surgical repair in low-risk cases carries an average 6% mortality, the mortality of operating on ruptured AAAs averages 50% (40% to 95%), although survivors can do well. In the United States, 40.000 abdominal aortic reconstructions are performed per year, leading to more than a billion dollars of in-hospital costs. There is no universally accepted single definition of AAA. Most often, though, it refers to a localized dilation of the abdominal aorta (usually infrarenal) with an increase in diameter of 150% or more of expected (typical value used for defining an AAA is $\geq 3\,cm$, although some studies have used $\geq 3.5\,cm$ and even $\geq 4.0\,cm$). All layers of the wall are present.

The localized aspect of morphology is the most important feature. Some authors have indexed AAA diameter to body variables such as body surface area, weight, and height. Women are only one third as likely to have AAAs as are men; however, rupture is four times more likely in women and more likely to be fatal. AAA anatomy encroaching on the renal arteries is more common in women. Almost all women who present with AAA are older than 70 years. The actual incidence in asymptomatic individuals is still unknown, and the determined number is strongly influenced by both the study population and the definition of AAA. AAA incidence varies fourfold according to the definition and population studied. The more widespread use of ultrasonography and computed tomography (CT) for screening and non-screening purposes increased the detection rate of AAAs sevenfold during the last four decades. This change in clinical detection, coupled with an aging population, is responsible for an increasing number of cases. The majority of AAA patients (75% to 90%) have hypertension, and many are smokers (as many as 50% to 90% in some studies). Concurrent vasculopathies and comorbidities are common and are highly relevant with respect to surgical and percutaneous procedures, operative risk, and nonoperative risk. Vasculopathies include coronary artery disease, peripheral vascular (iliofemoral) disease, cerebrovascular disease, atherosclerotic renovascular disease, and other aneurysms (e.g., thoracic).

1.4   Imaging technique

1.4.1   CTA: computed tomography angiography

Modern day computed tomographic aortography angiography (CTA) has replaced diagnostic angiography for the evaluation of thoracic aortic diseases, see figure 1.12. CTA is a modality to assess diseases of the aorta and has essentially established itself as the principal advanced diagnostic test for diseases of the aorta. Computed tomography (CT) is a technique for imaging cross-sections of a subject using series of X-ray measurements taken at different angles around the subject. The intensity of X-rays passing through the body is attenuated according to the density of tissues encountered. The source and the detector rotate around the subject and collect a row of X-ray measurements for each rotation angle.

The sinogram is the signal resulting from the acquisition, and is represented as a series of matrices with detected attenuation on the x-axis and rotation angle on y-axis. The image is reconstructed by solving the inverse Radon transform on the image grid.

The reconstructed image contains attenuation values expressed by Hounsfield units (HU), for which water is conventionally represented by 0. Consequently, fat is associated with negative values, connective tissue by low positive values and calcium by high positive values. For vascular imaging, radio-opaque medium is injected intravenously. The HU values yielded by contrast agents
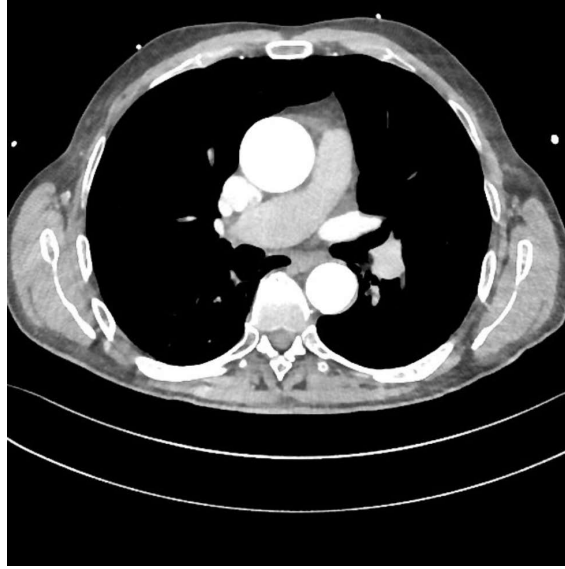
Figure 1.11: Modern day computed tomographic aortography angiography (CTA) of the aorta, transversal view. This image has been produced after injection of contrast medium to enhance thoracic aorta.

are positive values between that of connective tissue and that of calcium.

Scanners today available in the clinical context allow in-plane resolution $0.5\,mm$ and slice thickness of less than $1\,mm$ in a single breathhold, this is possible thanks to the high temporal resolution, CTA is acquired with a fast scanning times (15 to 20 seconds).

CTA is an imaging technique with advantages and disadvantages. Main advantages are non-invasivity of the technique, low scanning time that enable the usage of CTA in acute clinical settings and for old and painful patients, and the usage of a variety of imaging techniques such as multiplanar reconstructions, volume rendered (VR) images, and maximum intensity projections (MIP).

Although widely employed in the clinical practice, CT angiography presents also some disadvantages related to the X-ray dose absorbed by the patient and the contrast agents employed, which are iodinated and may include risks of nephropathy and allergy.

4D-CTA: time resolved computed tomography angiography

Radiological imaging is moving to full four-dimensional data acquisition. The development of CTA with retrospective ECG gating has been driven by coronary artery CTA, but it also provides significant benefits to imaging of the thoracic aorta. Retrospective ECG gating or ECG synchronization virtually eliminates cardiac pulsation artifacts and has therefore extended the clinical applicability of CTA to finally also include the aortic root. Moreover, ECG gating allows cardiac phase-resolved ('time-resolved') cine imaging and visualization, adding a 'fourth dimension' ($4D$)

to this technique - i.e., it is possible to obtain images at different time points during the cardiac cycle. A minimum temporal resolution of eight phases per cardiac cycle can give an adequate perspective of the aortic dynamics.
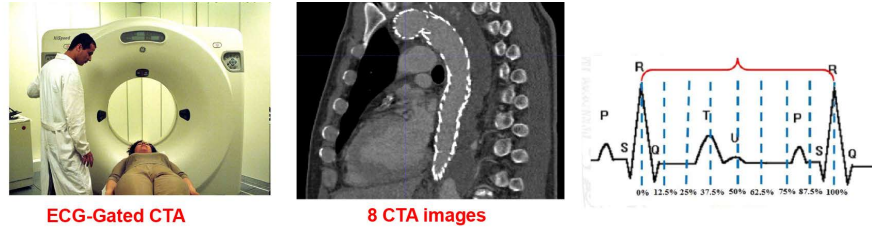
Figure 1.12: 4D computed tomographic aortography angiography (4D-CTA) of the aorta. ECG-gated image acquisition can help in gather aortic dynamic changes. In fact, as visible in the picture on the rigth side, it is possible to acquire multiple CTA of a specific patient at different point along the entire hearth cycle, carrying therefore information on specific time instant.

An immediate clinical benefit of motion-free 3D imaging of the thoracic aorta is improved visualization and thus characterization of acute aortic dissection and its variants. In addition to the ability to visualize a dissection flap all the way to the aortic root and into the coronary arteries, it has become possible to precisely localize the site of intimal tears, which is increasingly important in the stent-graft era. Furthermore, motion-free images allow the detection of less-common, subtle but clinically equally important intimal lesions, which have been notoriously difficult to detect in vivo with any imaging modality.

1.4.2 Image representation and handling

The 3D images acquired with different imaging techniques, usually in the form of stacks of 2D images, are stored on workstations linked to the scanners of the machine, and must be transferred to calculators for processing. This processing has to be done without loss of information. In fact, the number of gray levels, that represents medical images, is greater than 256, 8-bit image formats, and this type of images can not be held by a classical image extension, such as TIFF or PNG. Moreover the imaging machines offer the capability to give back lots of information: patient's name, date of acquisition, type of investigation, resolution, position and more. All those information need to be stored within the image and have to be easily accessible. The need of a consistent way to handle such amounts of data has led to the definition of a standard for communication and storage of medical image data, the DICOM (DIgital COmmunication in Medicine) format. DICOM is a standard for handling, storing, printing, and transmitting information in medical imaging. It includes a file format definition and a network communications protocol. The communication protocol is an application protocol that uses TCP/IP to communicate between systems. DICOM files can be exchanged between two entities that are capable of receiving image and patient data in

DICOM format. Images stored in the DICOM format contain an header which contain a number of tags organized into groups, followed by image data. By reading the tags and the image data it is possible to reconstruct the acquired volume from the image stack without the need of further information

1.5   Aorta lesion and endovascular treatment: TEVAR

Possible approaches used to face aortic pathologies repair include the traditional open laparotomy and newer minimally invasive methodologies, concerning the placement of endovascular stents. Endovascular aortic repair technique is a minimally invasive alternative to major open surgery for the repair of aortic diseases such as aneurysms and dissections. This technique results in reduced recovery times and potentially improved survival rates. It is performed through the deployment of an endograft that is a hollow, fabric-covered tube, surrounding a mesh metal cylinder (or stent), see figure 1.13.
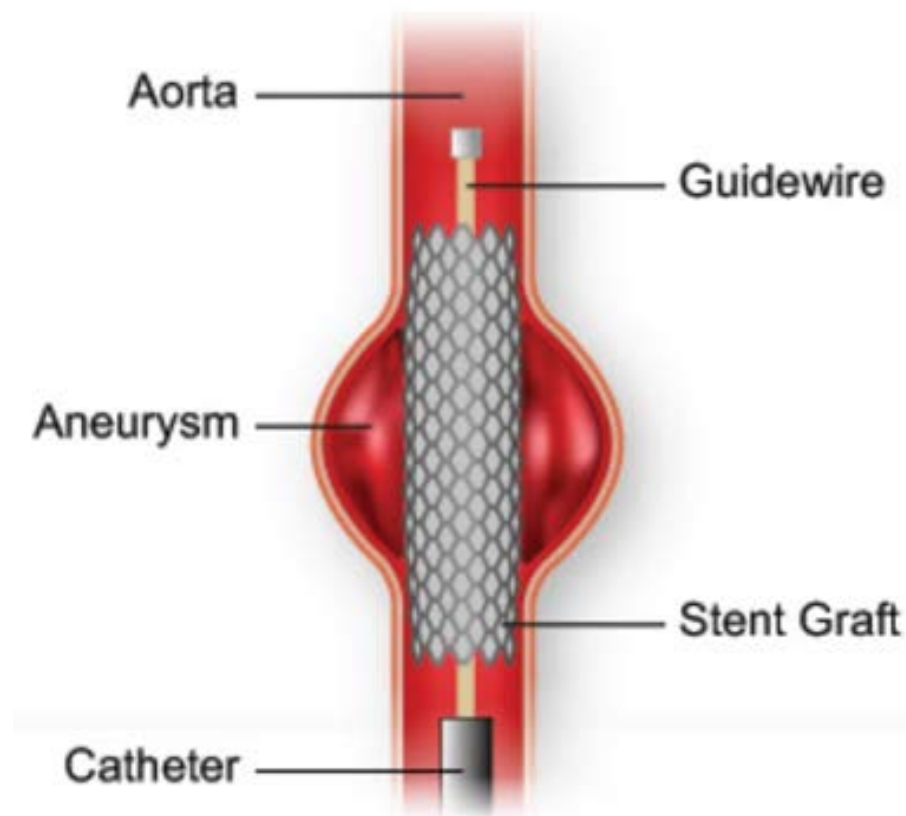
Figure 1.13: Modern day Magnetic resonance angiography (MRA) of the aorta, transversal view. Ascending and descending aorta are imaged here.

Until a landmark paper demonstrating the safe and effective treament of thoracic aortic

aneurysms with endovascular stent grafts by Dake and colleagues in 1994, conventional open surgery was the only effective treatment of thoracic aortic disease. During the last decade, the confluence of refined endovascular techniques and improved devices combined with widespread commercial availability of stent grafts has fueled an explosion of centers that offer endovascular stent grafting to treat a wide range of thoracic aortic disease. The desire to avoid the morbidity associated with traditional open repair has broadened both the spectrum of thoracic aortic diseases treated and the segments of the proximal and distal aorta deemed suitable for stent grafting. Endovascular surgeons currently have the ability to stent the thoracic aorta from the distal aortic arch down to the aortic bifurcation. Specialized centers are also gaining experience with stent grafting of the aortic arch and, in very select cases, the ascending aorta. The procedure is carried out in a sterile environment under x-ray fluoroscopic guidance. It can be performed under general, regional (spinal or epidural) or even local anesthesia. Access to the patient's femoral arteries can be with surgical incisions or percutaneously in the groin on both sides. Vascular sheaths are introduced into the patient's femoral arteries, through which guidewires, catheters and the endograft are passed. With most devices, the "main body" of the endograft is placed first, followed by the "limbs" which join the main body. The endograft acts as an artificial lumen for blood to flow through, protecting the surrounding regions. This in aneurysm reduces the pressure inside the sac, and helps the sac to thrombose and shrink in size over time. For the dissection the graft helps to restore perfusion to the true lumen and to cover the site of the primary intimal tear.

1.6 TEVAR: problems related and open issues

Although endovascular aortic repair seems promising, it has still some not negligible drawbacks and there are no prospective, randomized clinical trials comparing open surgical and endovascular repair for thoracic aortic diseases. Some example of introduced complications by stent graft apposition, distinct from those observed after open surgical repair, are: side branch coverage, endoleak, graft collapse, graft migration, retrograde aortic dissection, aortic rupture (stent strut), access complications, iliac rupture, iliac dissection, contrast-induced renal failure, and reintervention. The requirement for frequent postintervention imaging also exposes patients to both repeated high doses of radiation and intravenous contrast material. The long-term durability of stent grafts has also not been firmly established. In many cases, to allow a suitable proximal seal zone, the left subclavian artery is covered by the proximal end of the stent graft. These cases extend the limits of stent graft therapy because many of the patients are young with small aortic diameters, small access vessels, and a narrow inner radius of the aortic arch. If the side branches are covered then the revascularization, for example, of the left common carotid artery and/or the left subclavian artery from the innominate artery or the right common carotid artery need to be addressed.

These "extra-anatomic bypasses" can be performed without an invasive thoracotomy. Continued design improvement in stent graft including branched endografts will reduce but not eliminate multi-stage procedures.

1.7 Aim of the work

The elasticity of the thoracic aorta serves a critical role in damping and conducting the high pulsatile flow coming from the left ventricle. It allows for flow storage during systole and release during diastole, which is known as the "Windkessel effect". In this setting, aortic strain is traditionally described in the circumferential direction, which ranges between 8% and 11% in adults (Redheuil et al., 2010). But the thoracic aorta also extends longitudinally. A recent study showed that longitudinal strain of the ascending aorta in adults ranges between 6% and 9% and is higher in females (Bell et al., 2014).

Thoracic aortic diseases and their endovascular management, with the deployment of a rigid stent-graft (Kleinstreuer et al., 2008), can disrupt the biomechanical balance and functionality of the elastic vascular system (Raaz et al., 2015) (Tzilalis et al., 2012) (Midulla et al., 2012). TEVAR might lead to a compliance mismatch between the stent-graft and the aorta that can increase wall stress in the adjacent aortic segments to compensate for the stiffened segments (Raaz et al., 2015) (Midulla et al., 2012). This repeated process could determine arterial wall lesions and aneurysmal dilatation, stent-graft fracture or collapse, and stent-graft related complications such as endoleaks and retrograde/ante-grade dissections originating at the level of the proximal or distal end of the device (Raaz et al., 2015) (Muhs et al., 2006) (van Prehn et al., 2007). In addition, stent-graft induced stiffening elevates pulse wave velocity and cardiac after-load, leading to hypertension and cardiac remodelling (Tzilalis et al., 2012). Moreover both acute TEVAR related complications and long-term cardiovascular remodelling may determine outcomes after TEVAR.

Although thoracic endovascular aortic repair (TEVAR) has become the preferred treatment modality for several thoracic aortic pathologies, its impact on aortic strain remains unclear and despite the multiple adverse outcomes, the use of TEVAR increases and treated patients are becoming younger (Von Allmen et al., 2013) (Perera et al., 2014). In fact the introduction of a rigid metallic stent-graft inside an elastic tissue exposed to high dynamic and ciclic loads can produce variation in the standard beheviour of the aortic dynamic environment and such a behaviour deserves to be investigated in a deep and exhaustive manner.

The aim of this thesis resides therefore in clarifying the clinically relevant impact of aortic stent-graft on aortic elasticity in a quantitative, robust, and repeatable manner. The analysis of both circumferential and longitudinal aortic changes, based on pre- and post-TEVAR dynamic imaging, is addressed and might provide an important tool to quantify early- and long-term outcomes in

patients managed with TEVAR and might provide hints for future improvements in stent-graft design. 4D-CTA - i.e., time resolved computed tomography images -, acquired with contrast medium are exploited to gather diagnostic images before and after TEVAR. Those dataset ECG-gated are made of 8 CTA images of the patient covering the entire hearth cycle and thus giving the possibility to gather the dynamic changes of the aorta.

The tool described in this work is designed to provide a work-flow that in an automated and leaned fashion can process medical images, create 3D models, extract geometric features from a given aorta in a quantitative manner, and compare these quantities before and after TEVAR. The user interactions within the different assignments along the entire procedure has to be elevated at the highest level possible, in other words the potential users do not have to take decisions that can invalidate repeatability and reproducibility of the results. Precise and repeatable measures are a primary goal along with the formulation of dynamic quantities.

The tool has been set up specifically on the thoracic aorta and its qualities reside on the reduction of workload, reproducibility and time saving. The steps developed to achieve the aim are described extensively in the chapters that will follow. The level-set segmentation technique and the colliding front initialization are modified specifically based on the aortic topology and a specific workflow is defined to be efficient on a 4D-CTA dataset of a thoracic aorta. Geometric quantitative analysis is carried on exploiting the centerline as well as automatic recognition of clinical regions of interest for which geometric measures such as area, diameter and length are computed and tracked through time.

1.8 Implementation

The tool has been developed using an approach based on modules, each module is built independently from the others but they constitute a well defined pipeline to create a complete geometric processing of 3D thoracic aortic models. All the modules developed in this work follow an object-oriented approach and have been implemented in *Python* (interpreted high level language). The tool relies on three major open source efforts in the field of scientific visualization and medical image processing. The *VisualizationToolkit* (*VTK*) (W. Schroeder, 2005), the *InsightToolkit* (*ITK*) (L. Ibanez, 2005), and the *VascularModelingToolkit* (*vmtk*).

Chapter 2

Geometric characterization of the aorta from patient-specific images: State of the art

Morphological characterization of vascular districts while in principle may be available, most of the time is time consuming and laborious, especially in clinical settings, where is commonly performed by hand. This is a limitation that needs to be overcame since quantitative evaluation of 3D morphology has to rely upon solid computational geometry criteria in order to be able to deal with high inter-patient variability of vascular network and to return reliable results needed for clinical evaluation. The aim of this thesis is the development of a computational tool for the 3D segmentation and morphological characterization of vascular networks, in particular its application to 4-dimensional data-sets of the thoracic aorta in patients affected by aneurysms and dissections both in pre- and post-operative conditions. Before describing the single steps that form the whole pipeline we would produce and overview of the state of the art of available tool for the morphological characterization of vascular networks.

2.1 Morphological characterization of vascular networks exploiting static medical images

Common exploited images technique for produce static imaging of the aorta are computed tomography angiography (CTA) or magnetic resonance imaging (MRI). These techniques have been used to assess rupture risk of aortic aneurysm or to evaluate planning of (thoracic) endovascular aortic repair (TEVAR or EVAR).

Reviewing the literature a bunch of studies exists about surface topology characterization through static medical images. In particular these studies aim at producing advice concerning progression of the pathology, risk of rupture, and stent-graft sizing once endovascular surgery is chosen as treatment technique. Evaluating rupture risk is critically important as aneurysm rupture carries high mortality rates. Two-hundred thousand new AAA cases are diagnosed each year in the United States and 15,000 people die from AAA rupture each year. AAA rupture is the 13th leading cause of death in this country and affects 1 in 250 individuals over 50 years of age (Upchurch and Schaub, 2006). Actually the standard for estimating rupture risk and thresholds for elective repair are a maximum orthogonal to the centerline diameter of 5.5 cm or greater and an expansion rate of 1 cm/year are . However, it is known, that these considerations alone are not a reliable measure of individual rupture risk. AAA rupture risk may be influenced by biomechanical and biological factors, among those factors wall stress has been shown to be a more reliable parameter than maximum diameter, and the stresses exerted on the aneurysm wall are influenced by the aneurysm shape (Vorp, 2007).

For predicting individual rupture and operative risks in pre-operative planning, computing index thresholds for patient selection, and for customizing designs of stent-grafts it will be really helpful to quantify the shape and size of patient-specific AAA. Adequate geometrical characterization requires taking into account the 3D complexity of the shape, tortuosity, and asymmetry of the AAA sac. Some authors showed that AAA with an asymmetric geometry exhibit higher wall stress (Vorp et al., 1998) and that ruptured aneurysms show more out of plane growth than in plane (Pappu et al., 2008). High wall stress is related to complex AAA geometry and highest stresses is proven to be associated with regions of high curvature (Sacks et al., 1999). Fillinger et al. (2004) proposed that geometric parameters may be able to accurately predict wall stress distributions. Mean and maximum centerline curvature were highly correlated with peak wall stress by Giannoglou et al. (2006) high values of Gaussian curvature, a parameter that indicates the existence of concave and convex regions on the vessel surface have been related to maximum stress on the aortic wall (Leung, Nyilas, Ng, and Xu, Leung et al.). Moreover mechanical analysis requires the accurate quantification of 3D anatomic structures since the surface geometry can have a direct impact on their mechanical behavior in health and disease. To be cited is the work of Sacks et al. (1999). The purpose of this study was to develop a method for non-invasive quantification of the 3D AAA surface geometry and to demonstrate the utility of this method on clinically obtained AAA spiral CT image. In fact for membrane shell, surface geometry is an integral part of how wall tension are spatially distributed for a given loading condition and AAA can be treated mechanically as thin shell. Elger at al. stated that probably rupture of aneurysm is more due to surface curvature instead to bulge diameter. 6 patients with AAA evaluated for surgical repair were studied through the acquisition of CTA images of the abdomen. A single

volunteer was also enrolled. Multiple cross-sections of the AAA at 3mm intervals were obtained and saved as image files, these sections were then interpolated thanks to a distance minimization algorithm to reconstruct the 3D surface of the aneurysms. They introduced the following reduced bi-quadric surface patch:

$$S(u, v) = au^2 + 2buv + cv^2 \,, \tag{2.1}$$

since AAA is a complex surface but smooth and continuous and therefore it is possible to approximate it with 2.1, where a, b, and c are fit constants determined for each surface node, using a local u-v tangent plane coordinate system. At each point on the 3D surface correspond both a major and minor principal curvature. The principal curvatures are unique to the surface and represent the maximum and minimum curvature values along the associated principal directions. From equation 2.1, magnitudes k_1 and k_2 and vector directions e_1 and e_2 of the principal curvatures are computed with the following formulas:

$$k_1 = a + c + \sqrt{(a - c)^2 + 4b^2},$$
$$k_2 = a + c - \sqrt{(a - c)^2 + 4b^2},$$

$$e_1 = [a - c + \sqrt{(a - c)^2 + 4b^2}]\mathbf{e_u} + 2b\mathbf{e_v} \qquad if \, a \geqslant c,$$
$$e_1 = 2b\mathbf{e_u} + [a - c + \sqrt{(a - c)^2 + 4b^2}]\mathbf{e_v} \qquad otherwise,$$

$$e_2 = -2b\mathbf{e_u} + [a - c + \sqrt{(a - c)^2 + 4b^2}]\mathbf{e_v} \qquad if \, a \geqslant c,$$
$$e_2 = [a - c + \sqrt{(a - c)^2 + 4b^2}]\mathbf{e_u} + 2b\mathbf{e_v} \qquad otherwise,$$

where e_1 and e_2 are referred to the local u-v coordinate system, instead k_1 and k_2 are referred to as the major and minor principal curvatures, respectively. From the principal curvatures, the mean M and Gaussian K curvatures can be computed with $M = \frac{1}{2}(k_1 + k_2)$ and $K = k_1k_2$. K is a particularly useful curvature parameter, its sign indicates the general shape of the surface. In particular, $K > 0$ indicates an elliptical surface, $K = 0$ a cylindrical one, and $K < 0$ a hyperbolic (i.e., saddle shaped) one. Moreover they studied the effect of AAA tortuosity on spatial distribution of surface curvatures independent of the effects of dilation (bulging). They computed tortuosity dividing the total AAA length (along the centerline) by the AAA height (i.e., the difference between the uppermost and lowest contours' centroids). They found that the AAA

surface area increased on average by 56% from the estimated normal aorta surface area and that the aneurysmal aorta increases its length by 27%. For the investigated cases k_1 ranged from 0.25 to $1.25cm^{-1}$, while k_2 ranged from -0.5 to $0.5cm^{-1}$. On the contrary the normal abdominal aorta showed k_1 of $0.0731cm^{-1}$ and k_2 of $0.0023cm^{-1}$, i.e., nearly a straight tube with diameter of $2.8cm$. Moreover k_1 was predominant circumferentially orientated for all the cases and k_2 showed high circumferential asymmetry, see figure 2.1. The authors of this study suggested that the focal regions of high curvature may be associated with high wall tension or stresses. Since the regions of high curvature are associated with AAA tortuosity, it may be that the rupture risk is closely associated with its degree of tortuosity than with its bulge diameter.
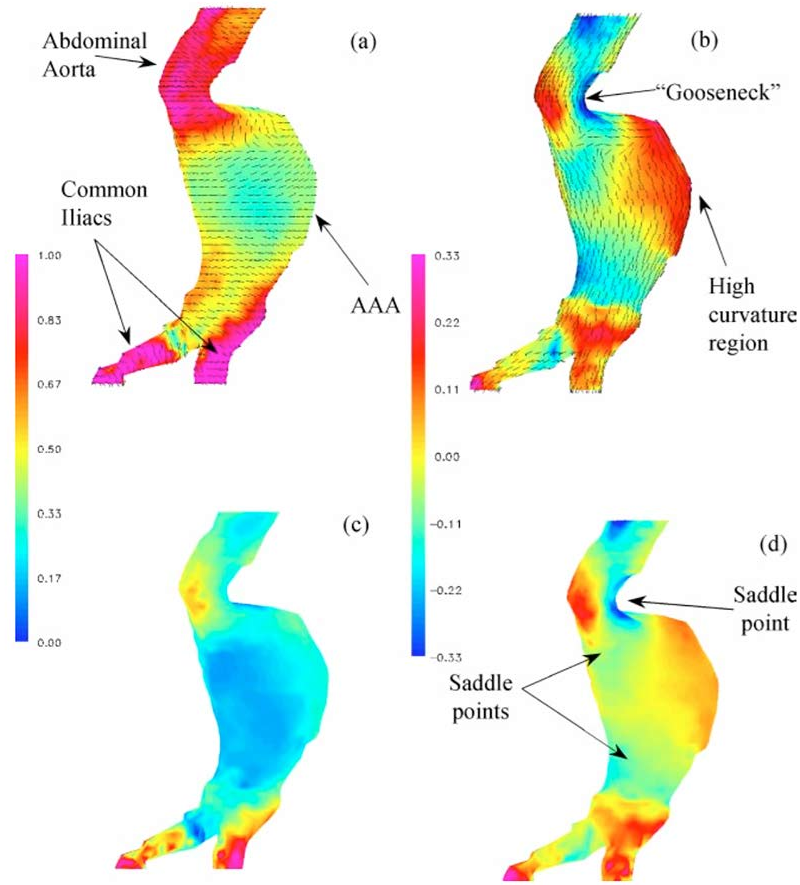
Figure 2.1: Spatial distributions of (a) k_1, (b) k_2,(c) M, and (d) K for an AAA which extended to the iliacs, with color indicating scalar magnitude and the vectors the principal curvature directions (e_1 and e_2). Over most of the AAA surface, k_1 was oriented circumferentially, while k_2 was oriented longitudinally. Most of the asymmetry of the AAA surface, particularly regions of curvature reversal, occurred along the longitudinal (k_2) direction. Changes in the sign of K indicated the occurrence of saddle (i.e., hyperbolic) regions (d). Figure is taken from the work of Sacks et al. (1999).

In a work of Shum et al. (2011), they proposed a simple framework to yield polygons of high

quality, and unstructured volume meshes. The surface topologies can be used to quantify geometric indexes exploited in this study as potential predictors of abdominal aortic aneurysm (AAA) rupture. In Shum et al. (2011) they segmented automatically the outer wall of the abdominal aorta using an intensity thresholding. The inner wall was detected by training a neural network to recognize regions where the inner wall was most likely to be. The study was preformed on 20 human subjects with AAA; 10 ruptured and 10 unruptured data-sets. Abdominal aortic images were acquired using contrast enhanced CTA. Nine indices were calculated to quantify the size, shape, and curvature of each AAA model. They computed three 3D size indices previously defined in Martufi et al. (2009): AAA volume (V), surface area (S), and intra-luminal thrombus volume (V_{ILT}), and two 3D shape indices based on V and S: the isoperimetrical ratio (IPR) and non-fusiform index (NFI). In addition, they also calculated four second-order curvature-based indices: area-averaged Gaussian and Mean curvatures (GAA and MAA) and the L2-norms of these curvatures (GLN and MLN), for extensive definitions of all the indexes refer to B. All indices are calculated for the 20 AAA geometries.

This study demonstrates that six of the ten reported indices, namely V, S, GLN, MLN, VILT, and GAA were statistically significant and higher for the ruptured aneurysms. Ruptured aneurysms generally tend to be larger than non-ruptured aneurysms, which could explain the strong relationship between the three size indices (V, VILT,, and S) and rupture. Also, the non-ruptured aneurysms chosen in this study were smaller in size than the ruptured AAA with respect to the maximum diameter.

In another work of Shum et al. (2011) they exploit the segmentation method already described in one of their previous work (Shum et al., 2011) and they applied it to a data-set consisting of 76 human AAA, 10 ruptured and 66 randomly selected unruptured aneurysms. Twenty-five size and shape indices were defined and calculated for each AAA model, as described by Martufi et al. (2009), for extensive definitions of all the indexes refer to Appendix B. They developed a method based on global geometric indexes of AAA size and shape and a learning algorithm that would be capable of discriminating between ruptured and unruptured aneurysms. The highest ranked features were chosen using a feature selection algorithm based on the χ_2-test. Results of their study showed that the average prediction accuracy of the decision tree model was 86.6% exploiting the highest ranked features, instead using only $D_{max} = 5.0cm$ as the predictive variable would correctly classify 19 unruptured aneurysms and all the 10 ruptured aneurysms; however, 47 of the unruptured aneurysms would be classified as ruptured, resulting in an accuracy of 38.2%.

The group of O'Flynn et al. (2007) designed a study to specifically characterize geometrically the arterial vascualture. In particular they aimed at determine branch origin and initial trajectory of the renal and anterior visceral arteries, calculate 3D branching angles and common iliac planarity at the terminal aortic bifurcation, quantify 3D curvature, non-planarity, and overall tortuosity of

the main renal arteries and infrarenal abdominal aorta and common iliac arteries, and demonstrate the magnitude of inaccuracy associated with planar analysis of 3D vascular geometry. They segmented MRI scans of 3 pts with Mimics software and calculated the centerline connecting the centroids of successive 2D cross-sectional lumen contours, normal to centerline itself. They defined branching angles analyzing two different types of 3D arterial branching sites, the visceral side branches and the terminal aortic bifurcation. They also investigated vessel tortuosity, curvature, and torision calculated using a standard formula from the Frenet–Serret theory of differential geometry. Although some errors exist associated with the reconstruction of vascular geometries they maintained the accuracy by minimizing the manual procedures and employing threshold based algorithms for lumen cross-section selection during image analysis. The results obtained from the reconstructed models showed mean 3D branching angles for the right and left renal arteries equal to 55.9 ± 7.2 and 62.6 ± 2.4 and mean aortic bifurcation 3D angle equal to 43.4 ± 9.0. They demonstrate that 2D measures of branching angle and trajectory are more prone to errors than 3D measures. This is due to the fact that the orientation of the branch axis relative to the viewing plane can greatly influence its projection onto that plane and consequently its perceived direction in space. In summary the parameters derived for 3D geometric characterization of the arterial vasculature overcome the limitations of planar analysis and may aid the standardization of 3D geometric definitions as well as the stent-graft design optimization.

2.2 Morphological characterization of vascular networks exploiting dynamic medical images

Dynamic aortic evaluation in planning thoracic endovascular aortic repair (TEVAR) is important to provide optimal stent graft sizing. The pulsatility of the aorta and its side branches during the cardiac cycle, the heartbeat related out of plane movement of the aorta and the other morphologic factors may all be of influence on the endovascular treatment for thoracic aortic pathology and not only (Van Keulen et al., 2009). Static imaging protocols do not consider normal aortic dynamics and may lead to stent graft to aorta mismatch, causing stent graft related complications, such as type I endoleak and stent graft migration (Van Keulen et al., 2009) (van Herwaarden et al., 2006). In fact, guidelines state that stent graft should be 10-20% oversized in comparison to the aortic diameter (van Prehn et al., 2009). However, a maximum aortic difference during the cardiac cycle has been reported around 18% in the ascending and descending thoracic aorta (van Prehn et al., 2007) (Muhs et al., 2006), and therefore the usage of static imaging for TEVAR planning may not be adequate. Dynamic imaging can assist in accurate stent graft selection and sizing pre-operatively, and evaluate stent graft performance during follow-up. In fact, it has been

demonstrated that the distensibility of the thoracic aorta is maintained after TEVAR, which makes adequate sizing even more important (van Prehn et al., 2009).

Need to be said that prior to study dynamics of thoracic aorta many studies focused on the dynamics of the abdominal aorta especially in those patients affected by abdominal aortic aneurysm (AAA).

In a study of 2009, Van Keulen et al. (2009) reviewed systematically a series of works to summarize the current knowledge concerning thoracic and abdominal aortic dynamics in patients affected by aortic aneurysms, both before and after endovascular repair procedure. In this review they included 25 studies: twenty-two studies investigated dynamic movement of the abdominal aorta, and three of the thoracic aorta. Ten of all these studies evaluated abdominal aortic changes both before and after (T)EVAR, instead all the other studies described aortic movements only before or after (T)EVAR. They described the results reported in the studies dividing them into groups based on measures analyzed. First they reviewed the works related to the dynamic changes of the proximal abdominal aortic aneurysm (AAA) neck as follows. Five studies were designed to study the influence of stent-grafts on aortic neck distension during the cardiac cycle (van Herwaarden et al., 2006) (van Herwaarden et al., 2006) (Teutelink et al., 2006) (Teutelink et al., 2007) (Arko et al., 2007). The mean aortic diameter change - i.e., $d_{systole} - d_{diastole}$ - per heartbeat 1 cm below the most distal renal artery was more than 1.6 mm in all studies. Maximum diameter increases of 14.0% (Teutelink et al., 2007) and 12% (van Herwaarden et al., 2006) were registered at this level. Measured values in between, or above, the renal arteries did not show differences with values 1 cm below the most distal renal artery. Post-operatively, the mean distension - i.e., difference between measured value at systole and at diastole - 1cm below the most distal renal artery was at least 2.0 mm in all studies. These values were not significantly different from pre-operative values in all studies (van Herwaarden et al., 2006) (van Herwaarden et al., 2006) (Teutelink et al., 2007). Arko et al. (2007) studied the displacement of the AAA neck per heartbeat, tracking the movements of the center of mass. There was significant displacement in both the anterior-posterior (AP) (mean 1.7 mm; standard deviation (SD) ± 0.6, range: 0.6 - 2.7) and lateral direction (mean 0.9 mm; SD ± 0.5, range: 0.3 - 1.5). Flora et al. (2001) demonstrated in four patients that during open surgery the AAA neck moves in the lateral (range: 1.0 - 1.5 mm) and longitudinal direction (range: 0.6 - 1.0 mm).

Van Keulen et al. (2009) moreover summarized the dynamic changes of the abdominal aortic side branches as follows. Two studies have reported on the movement of the renal arteries in patients with an AAA, both before and after EVAR (Muhs et al., 2006) (Muhs et al., 2008). The first study of Muhs et al. (2006), conducted on 15 patients, showed that the displacement of the center of mass of the renal arteries was up to 3 mm (mean 2.0 mm, SD ± 0.6), measured at a distance of 1.2 and 2.4 cm from the renal ostia pre-operative. After stent-graft deployment they

showed a decrease in displacement of the renal arteries at 1.2 cm from the renal ostia (mean 1.4 mm SD ± 0.7 (decrease of 31%)), instead the displacement at 2.4 cm from the renal ostia remained unaltered after stent-graft apposition. In the second study Muhs et al. (2008) collected eight patients pre-operative and sixteen patients post-operative to compare the influence of transrenal, infrarenal and fenestrated stent grafts on renal artery motion. Conversely from the previous study, neither transrenal nor infrarenal stent grafts altered renal artery motion. Fenestrated EVAR instead, with the placement of renal stent, reduced the renal artery motion more than 300% (mean 0.3 mm, SD ± 0.1).

They have reported also on the dynamic changes of the abdominal aortic aneurysm sac reviewing nine studies (Vos et al., 2002) (van Herwaarden et al., 2006) (Teutelink et al., 2006) (Malina et al., 1998) (Faries et al., 2003) (Lindblad et al., 2004) (Ganten et al., 2008) (Vos et al., 2003) (Long et al., 2004). Before EVAR, the mean distension of the maximum aneurysm diameter or area in the included studies were almost negligible. After EVAR, the mean distension of the sac decreased in three studies compared to preoperative values: from 1.0 mm to 0.3 mm (Malina et al., 1998); from 3.51 mm to 0.12 mm (Faries et al., 2003) and from 0.96 mm to 0.24 mm (Lindblad et al., 2004). Conversely, two other studies did not report a decrease of the median AAA distension after EVAR (Vos et al., 2002) (van Herwaarden et al., 2006). Finally, one study evaluated the displacement of the entire aneurysm sac during the cardiac cycle (Vos et al., 2003). The anterior-posterior (AP) movement of the aneurysm decreased from a mean value of 1.05 mm before EVAR to a value inferior to 0.5 mm after. Before surgery, the median cranio-caudal translation was 1.01 mm, and increased after surgery to a mean value of 1.69 mm.

In a study of Weber et al. (2009), they extracted a database composed by a sub-population of ten consecutive patients with chronic aortic dissection of type B - CADB - (8 men, 2 women). Inclusion criteria included: existence of chronic aortic dissection of the descending aorta with an intimal detachment arising immediately distally to the origin of the left subclavian artery and exclusively pharmacological treatment with antihypertensive. They acquired a three-dimensional scan volume at several time instances during the whole heart cycle and, therefore, providing a 4D-CTA data-set. Retrospective ECG-gating enabled the acquisition of 20 time points along the cardiac cycle, the time instances were transferred to a image processing workstation equipped with dedicated medical imaging software that permitted editing of this 4D data-set. On the basis of the first reconstructed time instance double-oblique multiplanar reformations (MPR) were generated perpendicularly to the vessel centerline at three segments of the thoracic aorta, see figure 2.2: ascending aorta between the origin of the coronary arteries and the brachiocephalic trunk (A), aortic arch between left carotid artery and left subclavian artery (B), and descending aorta 10 cm distal to the left subclavian artery (C).

For the three region of interests designated by the letters A, B, and C they calculated aortic
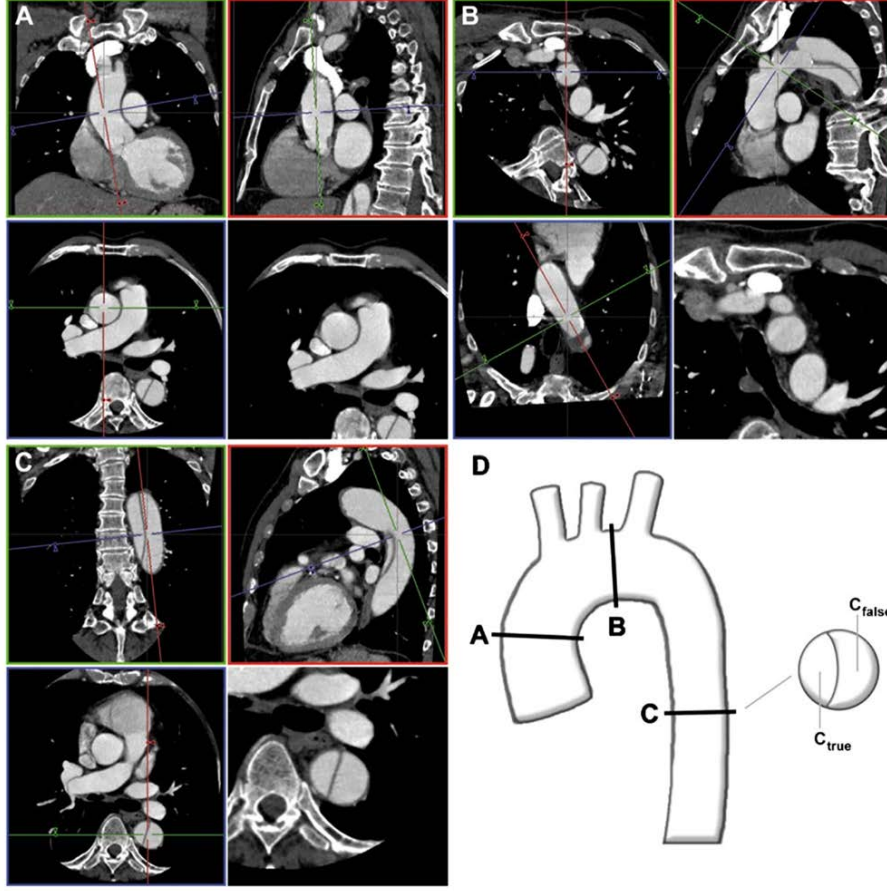
Figure 2.2: Adjustment of orthogonal aortic cross sections at defined aortic localizations. Double-oblique multiplanar reformations were adjusted perpendicularly to the aortic vessel course at ascending aorta (A), aortic arch (B), and descending aorta 10 cm distal to the left subclavian artery (C). Each target orientation is depicted at the bottom right. (D) Schematic illustration of the selected aortic localizations A, B, C, C_{false} and C_{true}. Figure is taken from the work of Weber et al. (2009).

area and aortic diameter along the major axis. The results highlighted that the true channel, which is significantly smaller than each of the other evaluated cross sections and represents the distal landing zone for EVAR, shows a greater amplitude of cross-sectional area variations compared with the false channel and the proximal landing zone. Moreover they demonstrated that the smaller the area of the true channel the higher the amplitude of its area pulsatility. The time progression of the observed measures showed a biphasic behaviour of each value that is consistent with the systolic and diastolic stages of the cardiac cycle. Whilst this trend is most obvious in non-dissected aortic segments and basically preserved in the true channel, the false channel exhibits a different behaviour no more characterized by systolic/diastolic phases.

Same research group investigated magnitude and direction of the heartbeat-related in-plane displacement of the ascending and descending thoracic aorta as well as of the vertex of the aortic arch - i.e., the most cranial location of the arch's curvature - using 4D-CTA (Weber et al., 2009).

They collected 11 patients with type B aortic dissection starting immediately distal to left subclavian artery (LSA) detachment. The datasets were transferred to a dedicated medial imaging workstation. To assess aortic in-plane displacements multiplanar reconstructions were taken in plane perpendicular to the centerline through the ascending and descending aorta. Separate evaluation was performed for true and false lumen. Semi-automated segmentation algorithm generates a region of interest - ROI - over the aortic contour for each time instance at three different aortic levels as previously depicted in figure 2.2. The software calculates the centroid of each ROI based on its geometry, the centroid is propagated and adapted for each time step. From the temporal changes of the centroid coordinates, temporal development and spatial direction of in-plane vessel displacement were determined relative to the first reconstruction interval. They considered only in-plane and not a thorough-plane displacement. The ascending aorta, section A in figure 2.2, describe an in-plane ovoid motion pattern with fast early systolic excursion to anterior position. In contrast to ascending the dissected descending segments, section C in figure 2.2, present a lesser magnitude of displacements and appear rather fixed to the vertebra. Horizontal displacement, see figure 2.3 left side, of the ascending aorta was found in the patient group with an average of approximately $5\,mm$. The contraction of the myocardium causes a shortening of the long cardiac axis that induces downward movement of the aortic root during systole and returns to initial position during diastole, section B in figure 2.2. Displacement in the vertical direction, see figure 2.3 right side, of $14\,mm$ has been recorded. Pathological condition associated with the stroke volume can affect vertical displacements either reducing or increasing it, is therefore important to state that non-conformity of graft can lead to graft instability and migration.
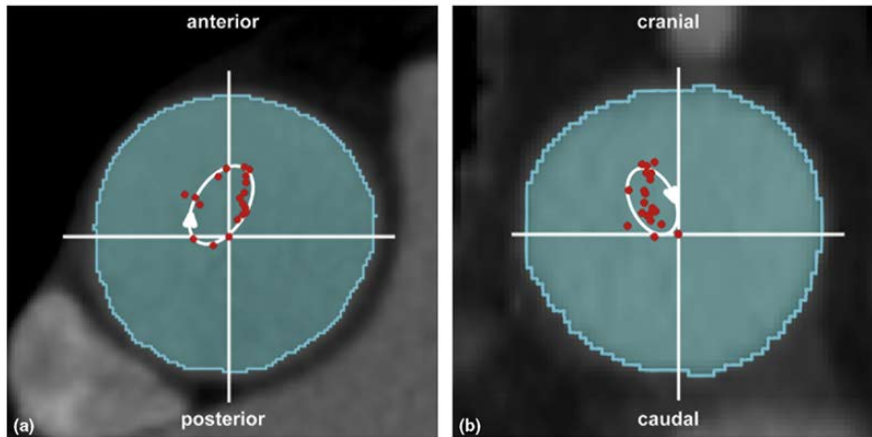
Figure 2.3: Visualization of the orientation of aortic motion at the mid-ascending aorta and the vertex of the aortic arch. While the ascending aorta underwent displacement predominantly directed anteriorly (a), the vertex of the aortic arch exhibited a slight cranial displacement (b). Figure is taken from the work of Weber et al. (2009).

Similar technique used in two work of Weber et al. (2009) has been exploited in a later work
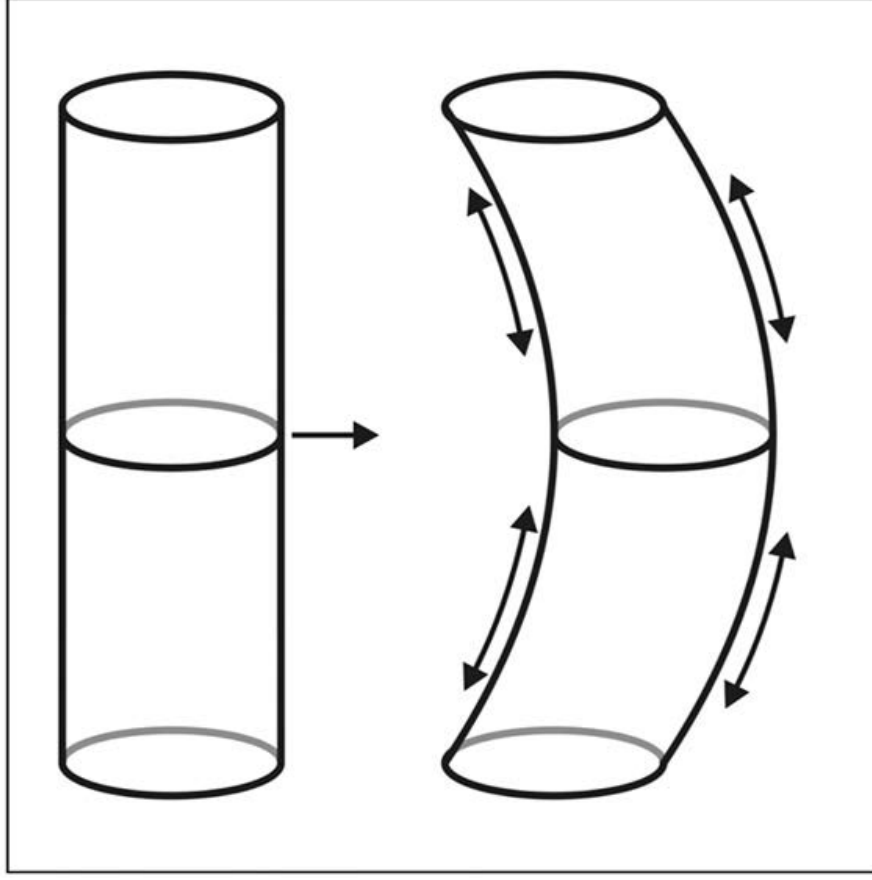
Figure 2.4: Schematic illustration of the biomechanical effect of the displacement perpendicular to the vessel centerline. Displacement strains the whole vessel wall and changes the vessel curvature. Figure is taken from the work of Rengier et al. (2012).

of Rengier et al. (2012), where the authors want to test their hypothesis that distension and displacement in various segments of the healthy thoracic aorta are significant and can be predicted based on clinical characteristics. They decided to study healthy volunteers based on the fact that TEVAR has been increasingly used in younger patients in case of traumatic aortic transection and that distension and displacements can produce not negligible cyclic changes in aortic morphology, see figure 2.4. In fact, the authors showed that aortic displacement works with the longitudinal forces on the vessel wall producing a strain both on the inner and outer aortic curvature, see figure 2.4. Furthermore, aortic displacement cyclically changes curvature and geometry of the aorta, figure 2.4, and consequently of the stent graft. Stent graft geometry has previously been shown to be an important determinant of drag forces acting on the stent graft and potentially leading to stent graft dislocation (Figueroa et al., 2009a), therefore quantification of aortic distension and displacement in a healthy population promises to identify groups of individuals that may undergo extensive geometric changes.

They first provided definitions of distension and displacement as follows: distension is the

diameter amplitude over the cardiac cycle and is regarded to be a function of vessel wall elasticity or compliance, displacement is the in-plane translational movement of the center of mass (CoM), the plane is defined perpendicular to the vessel centerline. Complete data sets were obtained for 61 volunteers that underwent MRI examination. Retrospectively ECG-gated dynamic data-sets covering one cardiac cycle were acquired at five locations in the thoracic aorta perpendicular to vessel centerline. The five locations, all of them chosen manually in a plane orthogonal to the centerline of the vessel, are respectively:

- between the aortic root and the brachiocephalic artery,

- between the left common carotid and left subclavian artery,

- 1 cm distal to the left subclavian artery,

- 10 cm distal to the left subclavian artery,

- distal descending thoracic aorta at the level of the diaphragm.

Using the same method described in two paper of 2009 (Weber et al., 2009) (Weber et al., 2009), they measured both distension and displacement, relative values were used in a multiple linear regression model including age group, gender, location, mean arterial blood pressure, heart rate and body mass index. As results they found that significant dynamic changes of the thoracic aorta are observable: diameter amplitudes reaches 6.9 mm (28% of aortic diameter) and aortic displacement reaches 11.2 mm (41% of aortic diameter). Age and gender had a significant impact on aortic dynamics, younger and female subjects showed significantly greater dynamics. This may result in relevant conformational changes of stent grafts with the risk of dislocation, especially in the younger population. The study of Rengier et al. (2012) shows that aortic distension and displacement can be predicted based on clinical characteristics relating to physiological parameters. This finding may help in identifying individuals at risk for high aortic dynamic changes, also being at risk for bad outcome of TEVAR.

In the previously reported studies measurements of distension and displacement were conducted on manually adjusted multi-planar image reconstruction and, thus, were possibly affected by errors introduced by end-user interaction. Recently, in a study of Weber et al. (2014), a computational procedure for automated vessel segmentation and landmark tracking was developed to overcome this limitation. The aim of this study was to investigate the magnitude and direction of displacement as well as the amount of cross-sectional distension of the thoracic aorta using this new approach in patients without evidence of thoracic aortic disease. They collected retrospectively 41 patients that underwent electrocardiogram-gated (ECG-gated) CT angiography; image data-set was made of 20 time points equally spaced covering the whole heart cycle. They exploited a parametric intensity model with elliptical cross-sections for temporal tracking, in this way motion

orthogonal to the centerline and deformation of the cross-section can be observed. Additionally they measured the longitudinal vessel motion along the centerline using intensity-based matching on spatially transformed image data. This combination of temporal and longitudinal tracking enabled to recover the full three-dimensional motion and deformation of the aorta over time during the heart-cycle; in fact, they measured displacement magnitude, displacement direction, and distension at five thoracic aortic levels of interest - i.e., aortic root distal to left coronary artery (COR), mid- ascending aorta between COR and brachiocephalic trunk (ASC), aortic arch distal to brachiocephalic trunk (BCT), aortic arch distal to left subclavian artery (LSA), descending aorta 10 cm distal to LSA (DES). The magnitude of displacement at the levels of interest has been measured in two different ways; determining first the maximum displacement vector (MDV), representing the maximum deviance of the aortic centerline during the heart-cycle compared with the first time point, and secondly defining the maximum displacement along each standard imaging plane (MDP), see figure 2.5. To quantify the main direction of displacement in an illustrative view they divided the imaging planes into 8 sectors of 45° each. MDP were allocated to the corresponding sector by calculating the displacement angle. Finally distension was expressed as absolute and relative values of major (DMAX) and minor (DMIN) axis diameters during the heart-cycle.
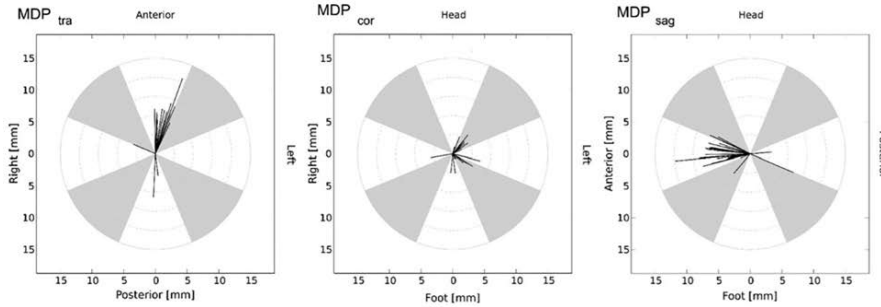
Figure 2.5: Directions and lengths of MDP at the level of COR are depicted for each patient and for each imaging plane.Imaging planes are divided into eight sectors each. Orientation of vectors within imaging planes define allocation of individual displacement to specific sectors. Figure is taken from the work of Weber et al. (2014).

Results highlighted that MDV was highest at COR and decreased gradually along the course of the thoracic aorta. At COR and ASC the spatial component of MDV was greatest along the y-axis. At BCT, displacement was evenly distributed. At LSA, displacement occurred predominantly along the z-axis. At DES no general preference of a specific spatial orientation was observable. Results for MDP were significant in terms of values at COR, where MDP was highest within transverse and sagittal imaging planes. This already implies that displacement was primarily orientated along the anterior-posterior direction. The same was the case for ASC, for the other levels of interest they did not find any significant differences between planes, the dominant sectorial direction of displacement was left and anterior for all positions, except for DES, we here depict

and example in figure 2.5 of MDP at COR level that represent well the pattern found by the investigators. To conclude this study aims at tracking dynamic changes of aortic geometry at clinical region of interest in a quantitative and reliable way.

A remarkable research activity in the field of thoracic aorta 4-CTA analysis is also carried on by a group of the University Medical Center Utrecht in the Netherlands and we will here cite some of their works on this topic.

In a work of Muhs et al. (2006) in 2006 they aim at utilizing high resolution ECG-gated 4D-CTA to characterize normal aortic motion, during the cardiac cycle, at relevant thoracic aortic anatomic levels for TEVAR. They collected ten patients affected by abdominal aortic aneurysm (aneurysm diameter larger than $5.5\,mm$) and they imaged the thoracic aorta from the heart to the celiac bifurcation. ECG triggered retrospective reconstructions were made at eight equidistant time points over the R-R cardiac cycle. They transferred the data-sets of the patients to a workstation equipped with a medical image analysis software. A user manually defines on the axial plane, perpendicular to the centerline of the vessel, relevant anatomic levels of the thoracic aorta for analysis, see figure 2.6

- level A: 1 cm proximal to the left subclavian artery,

- level B: 1 cm distal to the left subclavian artery,

- level C: 3 cm distal to the left subclavian artery,

- level D: 3 cm proximal to the celiac artery.

Afterwards the software automatically recognises and segments the 2D vessel's lumen, see figure 2.7, and measures area, minumum and maximum diameter changes of the regions of interest.

They defined the term pulsatility as radial displacement and area changes of the aorta lumen during a single cardiac cycle, and they calculated it as the largest difference respectively in diameter and area. Their results showed that maximum aortic diameter undergoes considerable variation during the heart cycle of approximately 10% at each anatomic level of interest. The change in aortic area showed, in their findings, a similar pattern as that of maximum aortic diameter change with significant pulsatility at each measured level. Results are summarized in table 2.1. To conclude they stated that endograft sizing based on poor preoperative measurements may result in post-operative complications such as intermittent type I endoleaks, graft migration, pros- thesis collapse, aneurysm rupture, and poor patient outcomes. There is a general need of understanding aortic pulsatility that may result in improved preoperative patient and device selection for TEVAR and subsequent improved graft durability and patient outcome. They presented here a semi-automatic framework to track dynamic changes of the descending thoracic aorta at relevant anatomical levels, however the study lacks of a three dimensional nature of measures, has a small number of patients,
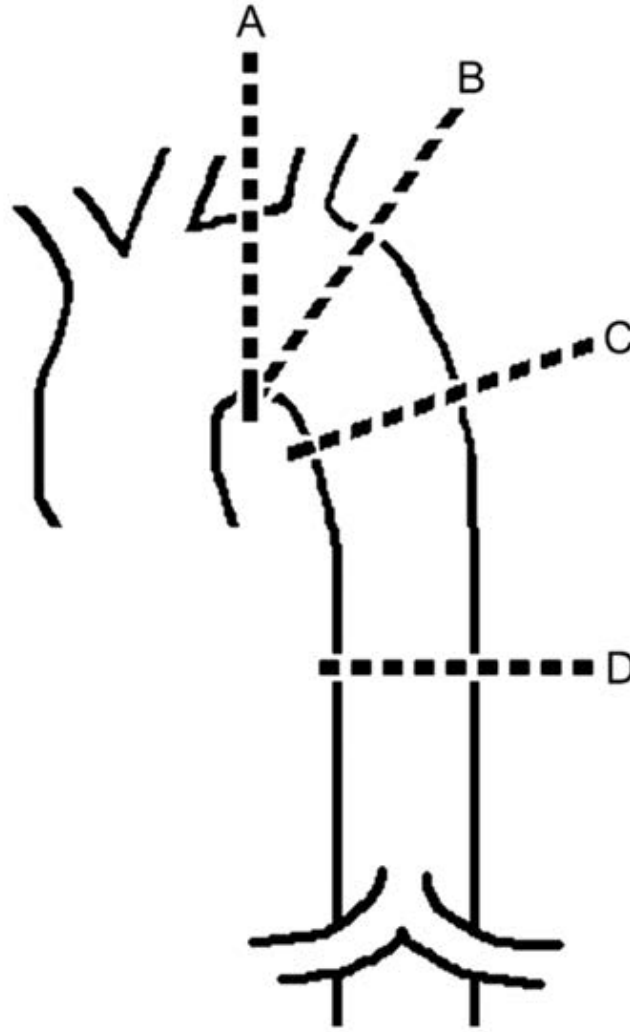
Figure 2.6: Diagram showing the four measured thoracic aortic levels. These levels included 1 cm proximal to the subcla- vian artery, 1 cm distal to the subclavian artery, 3 cm distal to the subclavian artery, and 3 cm proximal to the celiac artery. Figure is taken from the work of Muhs et al. (2006).

and manually adjustments are needed for the selection of the levels of interest and for segmentation improvements where poor quality of CT scans was present.

The same group of UMCU (University Medical Center Utrecht) in a study of van Prehn et al. (2009) evaluated the dynamic aortic changes in patients with thoracic aortic aneurysm exploiting 4D-CTA before and after endovascualar treatment for aneurysm repair. They aimed at understanding, exploiting ECG-gated CTA, the pulsatile aortic distention at relevant thoracic aortic anatomical levels in patients with a thoracic aoric aneurysm - TAA - before TEVAR and at investigating the influence of thoracic endograft placement on aortic distention. They collected six patients between 2005 and 2008 affected by TAA distal to the left subclavian artery and
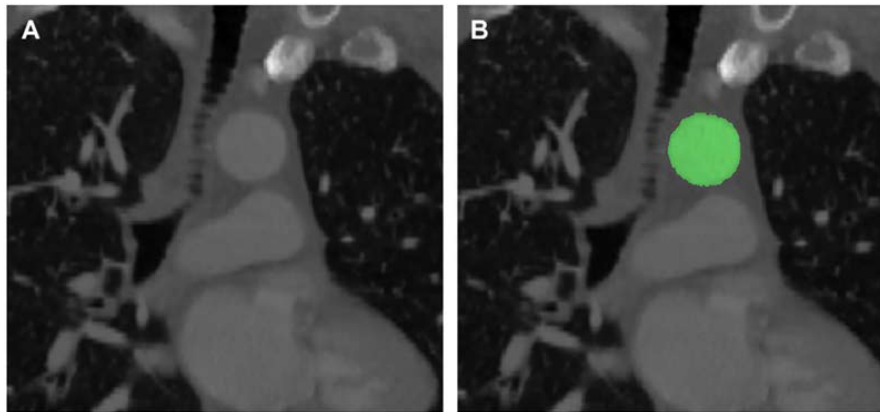
Figure 2.7: CTA with intravenous contrast demonstrates excellent image quality identifying the aortic lumen (A). Custom designed image segmentation software determines area and diameter changes based on this segmentation (B). Figure is taken from the work of Muhs et al. (2006).

Table 2.1: Area changes defined as pulsatility at the four levels of interest. The changes are measured as the difference between the maximum and the minimum area per cardiac cycle. LSA stands for left subclavian artery. Level A: 1 cm proximal to LSA , level B: 1 cm distal to LSA, level C: 3 cm distal to LSA, and levell D: 3 cm proximal to celiac trunk. Table is taken from the work of Muhs et al. (2006).

	A	B	C	D
Mean distention change (mm)	33.1 (4.8%)	33.2 (5.0%)	36.0 (5.5%)	37.9 (7.0%)
Range	2.7 - 6.9 %	3.9 - 6.9 %	3.0 - 10.8 %	1.4 - 3.1

that were evaluated for TEVAR. Each patient had both pre- and post-operative dynamic CTA scans collected, ECG-triggered retrospective reconstructions were made at eight equidistant time points over the whole cardiac cycle. They selected manually five region of interest, relevant for the evaluation and follow-up of typical TAAs and proximal sealing zones, perpendicular to the centerline of the thoracic aorta, see figure 2.8:

- level A: 1 cm proximal to the innominate trunk,

- level B: 1 cm proximal to the left subclavian artery,

- level C: 1 cm distal to the left subclavian artery,

- level D: 1 cm proximal to the proximal origin of the endograft,

- level E: 3 cm distal to the proximal origin of the endograft,

where the proximal origin of the endograft was defined as the first orthogonal slide on which the first stent strut became visible.
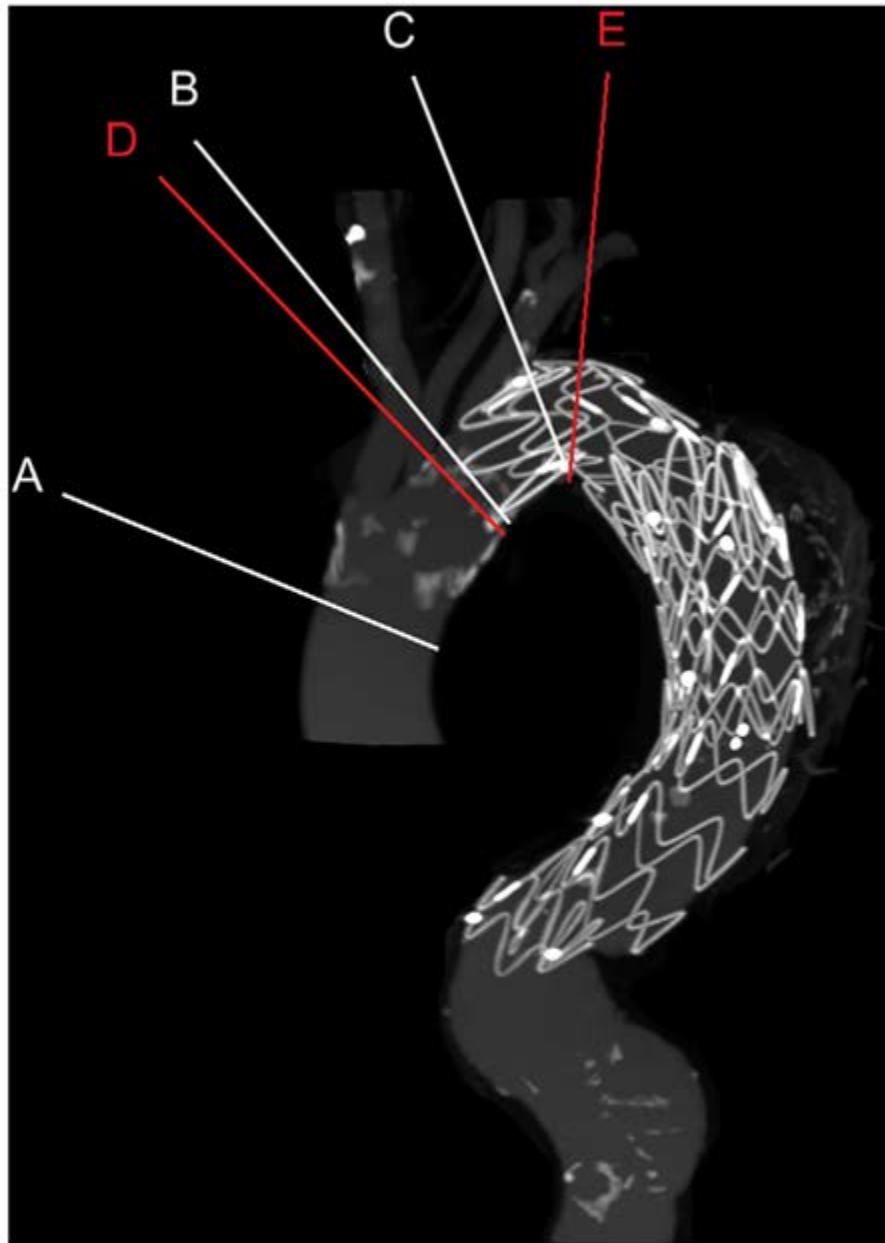
Figure 2.8: Anatomical levels. CTA maximum intensity projection reconstruction on which the levels studied are shown: 1 cm proximal to the innominate trunk (level A), 1 cm proximal (level B) and 1 cm distal (level C) to the left subclavian artery, and 1 cm proximal (level D) and 3 cm distal (level E) to the definitive proximal sealing zone. Levels in red depend on endograft position. Figure is taken from the work of van Prehn et al. (2009).

To measure levels D and E at the same level pre- and post-operatively, the centerline distance from the supra-aortic trunks to the proximal origin of the endograft was determined on the postoperative scan and applied to the pre-operative exam.

Once the levels are manually defined they performed at each level a multiplanar reconstruction

perpendicular to the centerline of the thoracic aorta and extracted eight images over the cardiac cycle per patient, obtaining a 2 dimensional in time data set. The data-set was transferred to a workstation and analyzed with the Dynamix software (Image Sciences Institute, University Medical Center, Utrecht, The Netherlands). The lumen of the aorta was semi-automatically segmented as described in Muhs et al. (2006), see figure 2.7, and manual adjustment of the segmentation was performed if needed. After segmentation of the aortic lumen in each cardiac phase, diameter change and area change over the cardiac cycle were measured. Diameter changes (difference between minimum and maximum diameters during the cardiac cycle) were measured on lumen axes defined on a line connecting one point belonging to the circumference of the lumen boundary to its opposite points through the center of mass of the lumen. They computed diameter measures for 180 axes, with an angular increment between each axes of 1 degree, finally the authors chosen the maximum and minimum between the measures acquired and computed the diameter changes. The aortic diameter and area demonstrated significant change during the cardiac cycle at each anatomical level, in each patient, in both pre- and post-operative settings, see figure 2.9.

They found that mean diameter change over the 180 axes ranged from 3% to 12% and that area change ranged from 2% to 20%. They also observed that thoracic aortic distention during the cardiac cycle is preserved after endograft placement. Preservation of distensibility after endograft placement may have major implications for stent-graft design and durability as the forces on the stents may be much larger after implantation than initially anticipated by stent manufacturers. Results are summarized in table 2.2. To the best of our knowledge, this is the first study with cine-CTA into the aortic dynamics in patients with TAA, both pre- and post-TEVAR. Even though this is a preliminary study there are some limitations that need to be addressed such as: small sample size, segmentation was semi-automatically made, and levels of interest were manually detected based on user experience.

Table 2.2: Area changes at the five levels of interest before and after endovascular procedure. The change is measured as the difference between the minimum and the maximum area per cardiac cycle. LSA stands for left subclavian artery. Level A: 1 cm proximal to brachiocephalic trunk, level B: 1 cm proximal to LSA, level C: 1 cm distal to LSA, level D: 1 cm proximal to proximal origin of stent-graft, and level E: 3 cm distal to proximal origin of stent-graft. Table is taken from the work of van Prehn et al. (2009).

	A	B	C	D	E
Before endovascular procedure					
Mean area change (mm^2)	51.4 (6.3%)	34.4 (6.2%)	33.2 (6.3%)	42.6 (6.8%)	35.9 (6.6%)
Range	3.3 - 14.9 %	2.2 - 12.0 %	4.4 - 8.5 %	3.4 - 17.5 %	2.6 - 12.4 %
After endovascular procedure					
Mean area change (mm^2)	64.5 (7.8%)	37.7 (6.2%)	29.6 (5.9%)	52.2 (7.5%)	27.7 (4.7%)
Range	3.0 - 13.7 %	4.4 - 10.0 %	3.0 - 12.3 %	2.5 - 20.2 %	2.6 - 6.8 %

In 2009 another paper has been published by the UMCU group (Van Prehn et al., 2009), here they pointed out another appealing topic for the community of the vascular surgeons interested
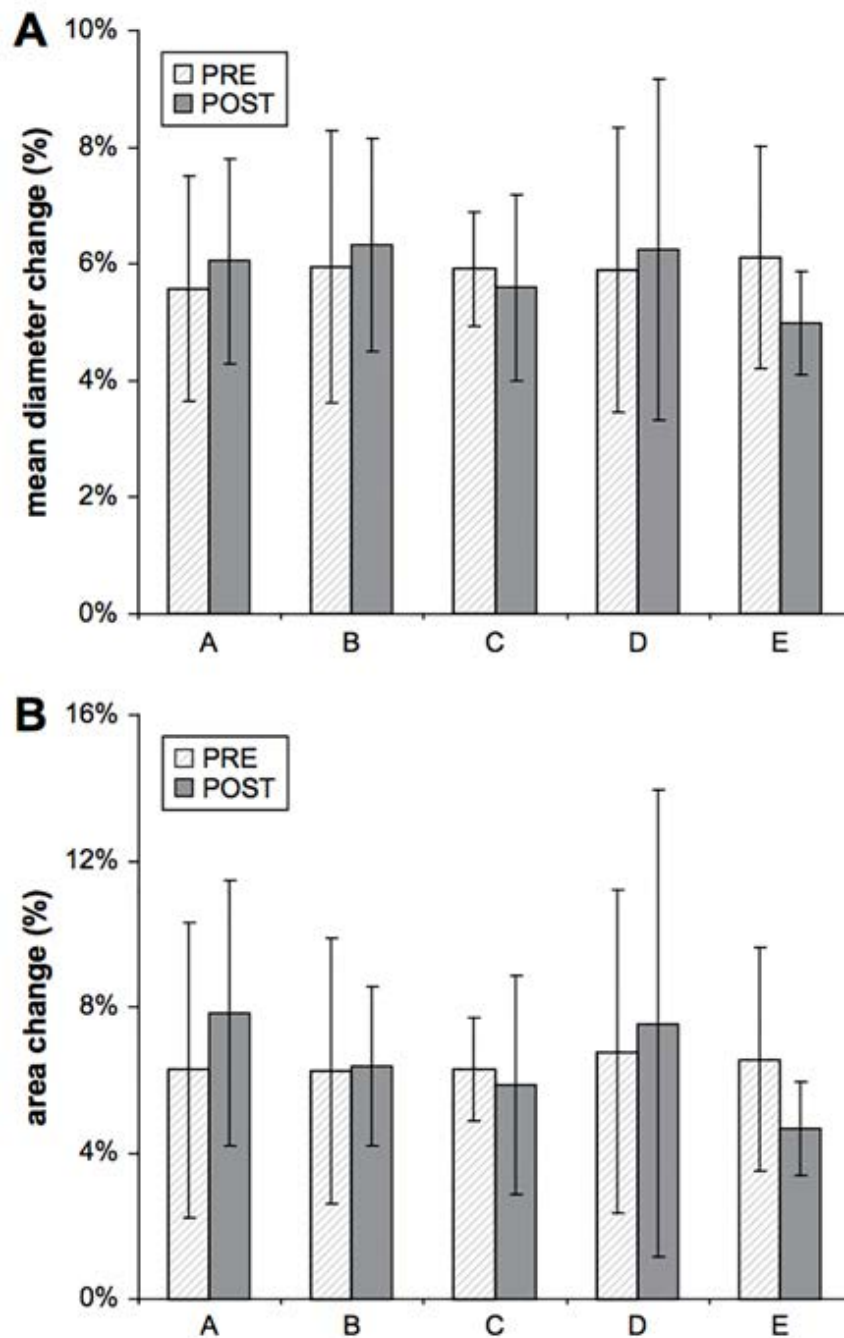
Figure 2.9: Mean percentage diameter (A) and area (B) changes of all patients. The mean percentage diameter and area changes are shown at each of the five measured levels, pre- and postoperatively. Figure is taken from the work of van Prehn et al. (2009).

in how vessels are dynamically changing due to the cyclic action produced by the heart. The dynamic aortic changes in younger persons without history of vascular pathology are important

as a baseline reference and are even more relevant with the extension of (thoracic) EVAR to traumatic ruptures of the aorta, more present in younger subjects, given this premise the authors aimed at understanding the dynamic changes in the undiseased aorta in order to gain insight into aneurysmatic and atherosclerotic aorta. The study protocol was the following: fifteen volunteers, mean age 24 years, were imaged with a clinical 1.5-T MR scanner, transverse ECG-gated high-resolution balanced fast field echo MRI scans with 16 reconstructed phases over the cardiac cycle were made perpendicular to the aorta. Five levels of interest along the vessel have been chosen:

- level A: 4 cm above the aortic bifurcation,

- level B: 1 cm below the lowest renal artery,

- level C: between the renal arteries,

- level D: 3 cm above the lowest renal artery,

- level E: the descending aorta 3 cm above the celiac trunk.

The scans were analyzed with dedicated in-house developed software Dynamix (Image Sciences Institute, Utrecht, The Netherlands) as desribed in previous works of the UMCU group (Muhs et al., 2006) (van Prehn et al., 2009). After segmentation of the aortic lumen in the images, the radius change - the difference between minimum and maximum radius over the cardiac cycle - was measured over 360 axes, with an angular increment of 1 degree. Radii were measured for each cardiac phase from the center of mass (CoM) of the aortic lumen to the inside of the aortic wall. They plotted the radius changes over each of the 360 axes as a function of angle, an example is depicted in figure 2.10. Zero degree corresponds to the anterior-posterior direction - i.e., AP-direction - and deviations of 90° and -90° correspond to right and left, respectively. They calculated also an asymmetry ratio dividing R_{max} by R_{min}.

They found that radius changes decreased from the proximal to the distal aorta, see figure 2.11. The change over the major axis ranged between 14% and 41%. The asymmetry rate varied per patient and per level and ranged between 1.02 and 1.53. In general, the orientation of the major axis was anterior-posteriorly, with minor variations per aortic level.

To summarize their conclusion, see table 2.3, since endovascular repair of traumatic aortic ruptures typically occurs in young patients, they studied the dynamic changes experienced by the descending aorta in healthy young volunteers. They found that, in the descending aorta, the mean radius change over the major axis was 35%. As a consequence, endovascular repair in younger patients will require more in terms of durability of the graft and sizing will be much complicated. Moreover they demonstrated that the aortic changes increased from the distal (abdominal) to the proximal (thoracic) aorta. The changes over the major axis ranged from 14% to 41%, this data are in contrast with the distension observed in the descending and abdominal aorta of patients with
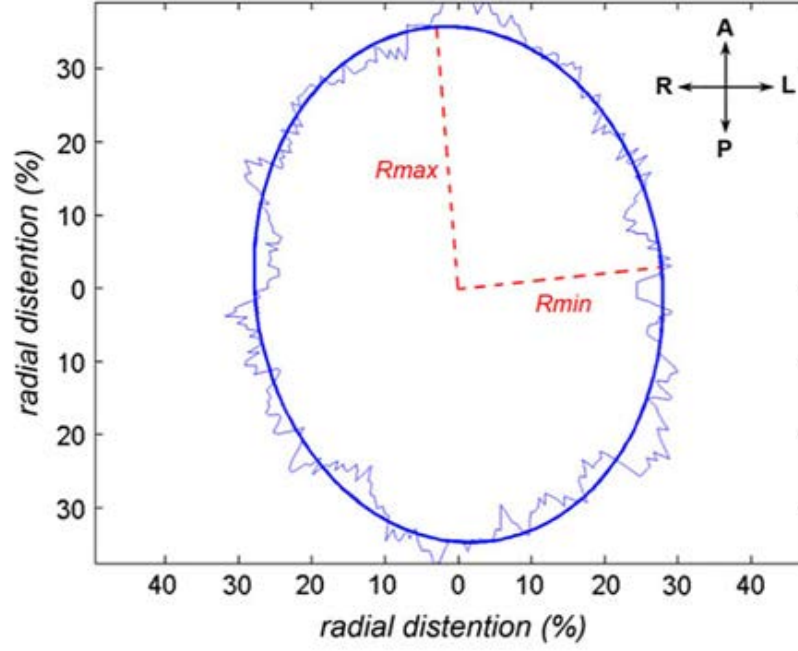
Figure 2.10: Radial distention plot with ellipse fitting. Radius change during the cardiac cycle is plotted as a function of angle. An ellipse is fitted over the plot. The radius change over the major (R_{max}) and minor axis (R_{min}) is calculated as well as the direction of the axis. A = anterior, P = posterior, R = right,L = left. Figure is taken form the work of Van Prehn et al. (2009).

abdominal aortic aneurysms (about 10%). An interesting proved findings is that, as first to our knowledge, they calculated an index of asymmetry, stating that aorta is not symmetric in shape and also does not change its shape symmetrically in time during the cardiac cycle. Asymmetric changes may help to explain why aneurysms develop at certain preferential places.

Another interesting fact is that at the supra-renal level the orientation of the major distension axis is in the right-anterior direction. The direction of distension might be attributed to the presence of surrounding structures that fix the vessel and force it to move the most along the free direction. When the aortic wall deforms non-uniformly, this will results in a non-uniform strain. Arterial wall motion, cyclic strain and wall shear stresses play important roles in changes of wall architecture (Moore et al., 1994) (Taylor et al., 1998) (Draney et al., 2004) (Pedersen et al., 1999). Non-uniform deformation and strain may contribute to the localization and development of vascular pathology. There is increasing evidence that aneurysm rupture involves a complex series of biological changes in the aortic wall (Choke et al., 2005).

This study has produced new interesting findings especially it has investigated the dynamic changes experienced by the abdominal aorta in healthy volunteers, but above all has introduced the concept of asymmetry referred to abdominal aorta, that may help in understanding why

Aortic Radial Distention
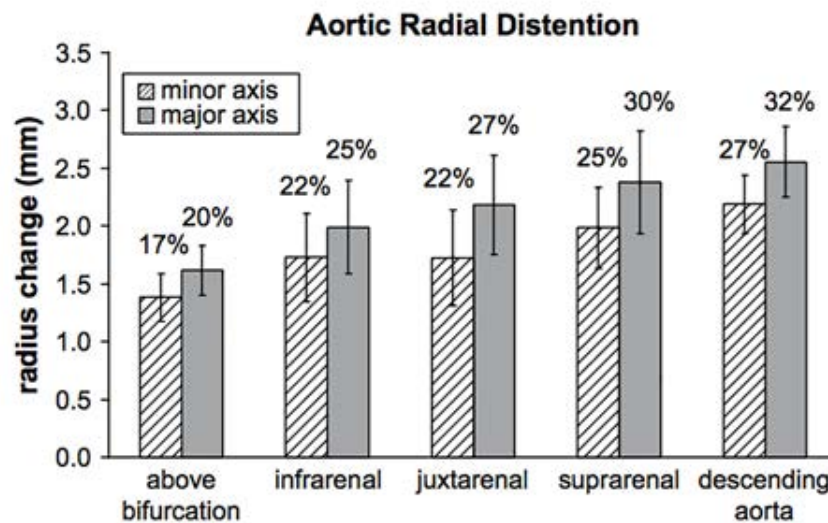
Figure 2.11: Mean and standard deviation of radius changes, expressed in mm, over the major and minor axis, calculated after fitting an ellipse through all radius changes in 360 directions (with 1 degree angular increment). Percentages above the bar represent mean percentage radius change. Figure is taken form the work of Van Prehn et al. (2009).
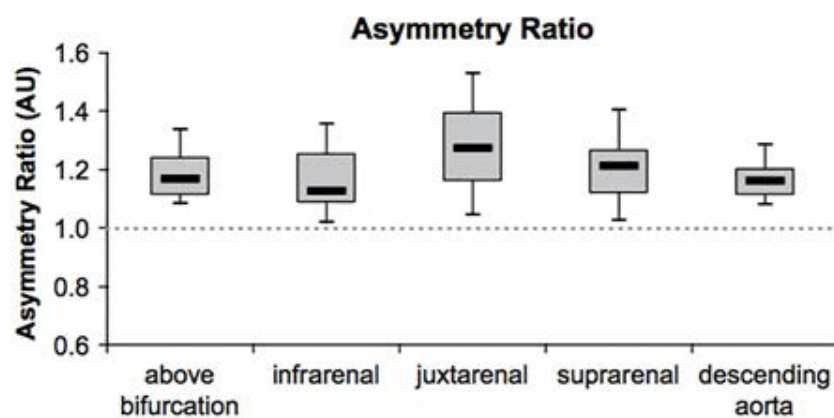
Asymmetry Ratio

Figure 2.12: Asymmetry ratio. AU stands for arbitrary units. The Ratio is calculated as distention over the major axis divided by distention over the minor axis $\frac{R_{max}}{R_{min}}$. An asymmetry ratio of 1.0 represents a symmetric distention and is depicted by the dashed line. Figure is taken form the work of Van Prehn et al. (2009).

stent-graft procedures have bad outcomes and why aneurysms or atherosclerosis develop. Some limitations remain, these are similar to the one addressed in the the previous studies conducted by the UMCU groups, such as small sample size, semi-automatic segmentation technique and manual choice of the levels of interest.

In a recent work of Suh et al. (2014), proposed quantification techniques to measure arch vessel

Table 2.3: Results. Aortic distensibility computed as mean ± SD and its relative range. The measures have been calculated for the clinical relevant levels of interest and are displayed in mm. Table is taken from the work of (Van Prehn et al., 2009).

	Above bifurcation	Infrarenal	Juxtarenal	Suprarenal	Descending aorta
Distention major axis (mm)					
Mean ± SD	1.6 ± 0.2	2.0 ± 0.4	2.2 ± 0.4	2.4 ± 0.5	2.6 ± 0.3
Range	1.1 - 1.9	1.2 - 2.9	1.6 - 3.3	1.4 - 3.1	2.0 - 3.2
Distention minor axis (mm)					
Mean ± SD	1.4 ± 0.2	1.7 ± 0.4	1.7 ± 0.4	2.0 ± 0.4	2.2 ± 0.3
Range	0.9 - 1.6	1.1 - 2.5	1.2 - 2.7	1.1 - 2.5	1.2 - 2.7
Asymmetry ratio (AU)					
Median	1.17	1.13	1.27	1.21	1.16
Range	1.09 - 1.34	1.02 - 1.36	1.04 - 1.53	1.03 - 1.40	1.08 - 1.28

geometry and deformation using CTA-based three-dimensional geometric models. Moreover they introduced cardiac-induced and respiratory-induced changes through the quantification of aortic arch translations and branching angles changes of the brachiocephalic artery (BA), the left common carotid artery (LCCA), and the left subclavian artery (LSA) in patients with thoracic aortic aneurysms and dissections. They enrolled 15 patients and acquired CTA images with retrospective electrocardiogram gating allowing the reconstruction of a 4D data-set at 10% intervals of the cardiac cycle. End-systolic images were reconstructed at 40% of the R-R interval and end-diastolic images at the 70%. They used four physiological states for the analysis i.e., inspiration + diastole, inspiration + systole, expiration + diastole, and expiration + systole. Using the SimVascular software they extracted the 3D models and the centerlines for the thoracic aorta, BA, LCCA, and LSA, see figure 2.13. First a reference centerline path was generated by hand-picking the centers of the vessel's lumen and interpolating these points with a cubic spline. Along the rough path, cross-sections orthogonal to the lumen are segmented with a two dimensional level set segmentation technique. The sets of cross-sectional segmentations were used to reconstruct the 3D geometry of the vessel and finally the true centerline is calculated exploiting the mathematically-computed centroids of each segmented sections; they performed a smoothing of the path with a 0.1 mm point interpolation and an optimized number of Fourier modes. They thus obtained the 3D coordinates of centroid-based path of the thoracic aorta, BA, LCCA, and LSA. Using Matlab they processed the path coordinates to compute arch branch positions and branching angles for each vessel at all models as well as their differences.

The branch positions of BA, LCCA, and LSA were tracked for each physiological state. They computed cardiac-induced aortic arch translation (Ci-AAT) and respiratory-induced aortic arch translation (Ri-AAT) as respectively:

$$Ci - AAT = \mathbf{x}_{sys} - \mathbf{x}_{dias} \tag{2.2}$$
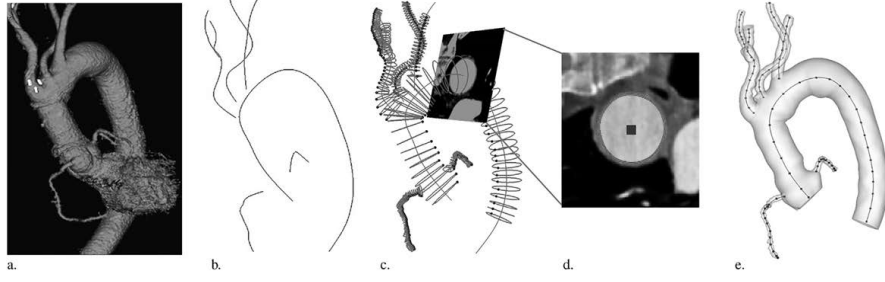
Figure 2.13: Lumen segmentation and centerline path extraction. (a) CTA images were loaded into the custom software SimVascular. (b) Vessel paths were constructed by connecting the hand-picked lumen centers along the thoracic aorta, BA (brachiocephalic artery), LCCA (left common carotid artery), LSA (left subclavian artery), and coronary arteries. (c) Along the vessel path, two-dimensional level set segmentations were performed to segment the lumen boundaries of the vessels. A 3D model was formed by lofting the contours to a two-dimensional shell surface. (d) Mathematical centroids were found from the segmentation contours. (e) Centerline paths were constructed by connecting the multiple centroids with cubic splines and reconstructed by optimized Fourier smoothing. Figure is taken from the work of Suh et al. (2014).

$$Ri - AAT = \mathbf{x}_{exp} - \mathbf{x}_{insp} \tag{2.3}$$

where $\mathbf{x}_{sys}$ and $\mathbf{x}_{dias}$ are the coordinates of the centerline path at systole and at diastole, instead $\mathbf{x}_{exp}$ and $\mathbf{x}_{insp}$ are the coordinates of the centerline path at expiration and at inspiration.

Moreover they defined the branching angle as the angle between the vector tangent to the centerline of the aortic arch and the vector tangent to the side branches: BA, LCCA, and LSA. The vector tangent to the aortic arch was computed by means of two points along the aortic arch centerline: the first at the level of the side branch ostium, the second 10 cm distal along the centerline. The vectors tangent to the side branches were computed from the branch ostium to three equally distant points along the side branches centerline: 10 cm, 20 cm, and 30 cm distal along the centerline, see figure 2.14. Higher branching angle indicates that the side branches are far away from the aortic arch, lower branching angle indicates that the side branches are closer to the aortic arch.

They computed cardiac-induced branching angle change (Ci-BAC) and respiratory-induced branching angle change (Ri-BAC) as respectively:

$$Ci - BAC = \alpha_{sys} - \alpha_{dias} \tag{2.4}$$

$$Ri - BAC = \alpha_{exp} - \alpha_{insp} \tag{2.5}$$

where α_{sys} and α_{dias} are the angles between aortic arch and side branches vectors at systole and at diastole, instead α_{exp} and α_{insp} are the angles between aortic arch and side branches vectors
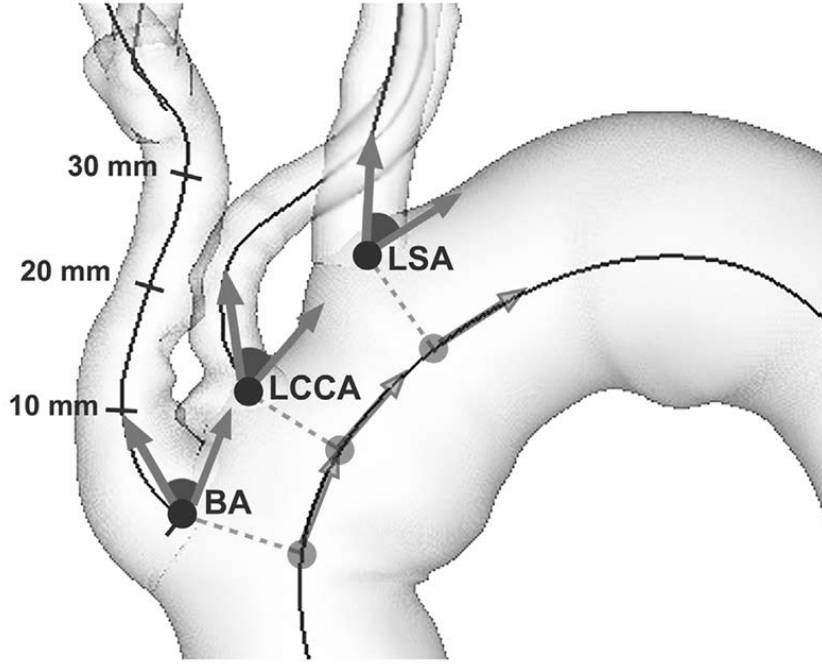
Figure 2.14: Calculation of branching angle of BA, LCCA, and LSA. Branching angle was defined as the angle between two vectors, one along the centerline path of the thoracic aorta and one along the path of each of BA, LCCA, and LSA. The thoracic aorta vector was defined by the point 10 mm distal to the branch ostium on the thoracic aorta centerline. The branch vessels vectors were defined by points 10 mm, 20 mm, and 30 mm distal to the ostia along the branch vessel centerlines. Figure is taken from the work of Suh et al. (2014).

at expiration and at inspiration. Results for Ci-AAT and Ri-AAT at BA, LCCA, and LSA, for branching angle of BA, LCCA, and LSA at the four physiological models and Ci-BAC and Ri-BAC of BA, LCCA, and LSA between the four physiological models are summarized respectively in tables 2.4, 2.5, and 2.6.

In this study the authors addressed the critical point of centerline calculation from which the fidelity of the measures depends. In fact being aware of this, they computed the centerline starting from the centroids of previously segmented aortic arch cross-sections in order to provide a more accurate and less user-dependent method compared with manual selection of sections and centerline along the vessel. They pointed out that cardiac pulsation and respiration resulted in significant translation of both aortic arch and side branches but with different direction and magnitude. BA, LCCA, and LSA showed different branching geometries and changes in branching angles were not significant. This findings may suggest that aortic arch endografts with branched components is not subjected to aggressive cyclic bending and angulation of the side branches.

So far we described bunches of method to characterize horizontally the cyclic changes experienced by the aorta but as the aorta expands horizontally it is slightly reasonable that it experiences

Table 2.4: Cardiac-Induced and Respiratory-Induced 3D Aortic Arch Translation (mm) at BA, LCCA, and LSA Branch Points. Values are mean ± SD. BA = brachio-cephalic artery, LCCA = left common carotid artery, LSA = left subclavian artery. Table is taken from the work of Suh et al. (2014).

		BA (mm)	LCCA (mm)	LSA (mm)
3D translation				
Diastole-systole	Inspiration	2.4 ± 1.7	2.2 ± 1.7	2.0 ± 1.5
	Expiration	2.5 ± 1.7	2.9 ± 1.8	2.8 ± 1.5
Expiration-inspiration	Diastole	6.7 ± 4.4	6.3 ± 4.2	6.1 ± 3.9
	Systole	6.6 ± 3.9	5.6 ± 3.5	6.4 ± 3.1

also vertical changes during the cardiac cycle. In fact in a study of Morrison et al. (2009) they developed a method to study how age influences circumferential and longitudinal strain of the human thoracic aorta. They pointed out that deformation of large vessels has been described by a variety of terms.

Distensibility ($\frac{cm^2}{mmHg}$) has been defined as the fractional change in vessel cross-sectional area divided by the distending pressure, which refers to the capacity of the vessel to stretch:

$$distensibility = \frac{(area_{systole} - area_{diastole})}{pressure} \tag{2.6}$$

The elestic modulus ($\frac{N}{cm^2}$) has been defined as:

$$E = K \frac{(P_{systole} - P_{diastole})}{(D_{systole} - D_{diastole})/D_{diastole}} \tag{2.7}$$

where K is a constant equals to 133.3 , P is the pressure, and D is the diameter of the vessel.

Moreover pulsatility has been defined as the radial displacement of the lumen during a single cardiac cycle:

$$pulsatility = radius_{systole} - radius_{diastole} \tag{2.8}$$

These methods and definitions, for the authors of the paper (Morrison et al., 2009) have been insufficient for quantifying in vivo cyclic strain and also have lead to confusion in most of the cases due to a missing unequivocal and standardized usage. They therefore developed a technique that can be applied to analyze the cyclic strain with cardiac-gated image data. Strain is typically defined as the ratio of the change in length to the original length. In vivo strain cannot be measured, however changes of deformation over the cardiac cycle relative to a reference configuration can be measured using cardiac-gated image data. They used as reference length the diastolic length and they computed the circumferential cyclic strain using the actual circumference of the lumen boundary, not the effective diameter or cross-sectional area changes as previous studies did. They

Table 2.5: Branching Angle (degrees) of BA, LCCA, and LSA at Four Physiologic Modes with Branch Vessel Vectors Defined by Points 10, 20, and 30 mm Distal to the Branch Ostia. Values are mean ± SD. BA = brachiocephalic artery, LCCA = left common carotid artery, LSA = left subclavian artery. Table is taken from the work of Suh et al. (2014).

		BA (mm)	LCCA (mm)	LSA (m)
Branch vector 10 mm distal				
Inspiration	Diastole	58.9 ± 18.7	52.8 ± 15.4	65.6 ± 19.5
	Systole	58.6 ± 20.6	51.8 ± 15.2	65.5 ± 17.4
Expiration	Diastole	60.4 ± 21.2	55.1 ± 17.5	66.0 ± 20.1
	Systole	60.0 ± 18.8	54.7 ± 14.3	65.8 ± 19.6
Branch vector 20 mm distal				
Inspiration	Diastole	56.9 ± 20.5	48.2 ± 16.3	63.1 ± 19.5
	Systole	55.0 ± 22.5	46.6 ± 15.6	63.1 ± 22.5
Expiration	Diastole	59.6 ± 26.9	50.3 ± 18.8	63.8 ± 23.0
	Systole	57.5 ± 23.0	50.3 ± 14.9	63.1 ± 21.2
Branch vector 30 mm distal				
Inspiration	Diastole	59.9 ± 25.7	44.7 ± 18.3	61.9 ± 23.4
	Systole	58.0 ± 26.7	43.7 ± 17.0	61.5 ± 20.9
Expiration	Diastole	63.2 ± 31.6	47.3 ± 21.0	62.8 ± 23.8
	Systole	60.9 ± 27.9	47.4 ± 18.5	62.2 ± 22.6

developed a method to effectively "attach" the reference frame to the ostia of the intercostal arteries and the major branch vessels. This helps to track the motion of the vessel wall by analyzing the same segment of the vessel at peak-systole and end-diastole, thereby eliminating spurious results due to through-plane motion of the vessel. This is not possible using an Eulerian reference frame, particularly in the region of the ascending thoracic aorta, where observed motion is large and therefore they exploited the Lagrangian reference frame to perform their work. They collected 14 gated 4D-CTA of the thoracic aorta composed of 10 equally spaced time instants. To calculate the centerline they used the same method exploited also later on by Suh et al. (2014). For each patient, two center paths were created to represent the vessel at peak- systole and end-diastole. Both paths were subsequently used for the deformation and strain calculations. They used anatomic markers along the thoracic aorta to examine the lumen boundary just distal to the ostia of intersecting vessels. As an example we describe their method applied at the distal location of the left coronary artery. First they followed the centerline from peak-systole until the segmentation plane(perpendicular to the lumen) was just distal to the left coronary artery (see figure 2.15, A) and outlined the lumen boundary using automatic segmentation. They then exploited the centerline and image data from end-diastole and highlighted the lumen boundary, again, just distal to the left coronary artery (see figure 2.15, B). They showed also the potential

Table 2.6: Differences in Branching Angle (degrees) of BA, LCCA, and LSA between Four Physiologic Modes with Branch Vessel Vectors Defined by Points 10, 20, and 30 mm Distal to the Branch Ostia. Values are mean ± SD. BA = brachiocephalic artery, LCCA = left common carotid artery, LSA = left subclavian artery. Table is taken from the work of Suh et al. (2014).

		BA (mm)	LCCA (mm)	LSA (m)
Branch vector 10 mm distal				
Diastole-systole	Inspiration	0.3 ± 4.2	1.0 ± 4.3	0.1 ± 4.8
	Expiration	0.5 ± 6.7	0.3 ± 7.8	0.2 ± 7.0
Expiration-inspiration	Diastole	1.6 ± 7.9	2.3 ± 4.7	0.5 ± 6.3
	Systole	1.4 ± 5.0	3.0 ± 5.6	0.3 ± 7.1
Branch vector 20 mm distal				
Diastole-systole	Inspiration	1.9 ± 3.6	1.6 ± 3.0	0.0 ± 4.1
	Expiration	2.1 ± 7.7	0.0 ± 7.9	0.7 ± 5.7
Expiration-inspiration	Diastole	2.7 ± 9.0	2.1 ± 4.6	0.7 ± 5.9
	Systole	2.5 ± 5.1	3.7 ± 6.0	0.0 ± 6.8
Branch vector 30 mm distal				
Diastole-systole	Inspiration	1.9 ± 3.3	1.0 ± 2.6	0.4 ± 3.9
	Expiration	2.4 ± 7.2	0.1 ± 7.1	0.6 ± 5.5
Expiration-inspiration	Diastole	3.3 ± 8.4	2.6 ± 5.4	0.9 ± 5.8
	Systole	2.9 ± 5.4	3.7 ± 6.6	0.7 ± 7.3

errors introduced when an Eulerian frame is detecting the lumen boundary in peak-systole, as described, and in end-diastole fixed the location of the segmentation plane as shown in figure 2.15, C.

The diameter and circumferential cyclic strain was calculated at seven locations along the aorta, see figure 2.16: 1) distal to the left coronary artery; 2) proximal to the brachiocephalic trunk; 3) distal to the brachiocephalic trunk; 4) distal to the left common carotid artery; 5) distal to the left subclavian artery; 6) distal to the first intercostal artery; 7) distal to seventh intercostal artery.

The length of the centerline was measured from the left coronary artery to the first intercostal artery, and the descending thoracic aorta (DTA) length was measured from the first to seventh intercostal artery.

They computed seven cross-sections orthogonal to the centerline of the aorta at peak-systole and end-diastole. The circumference of the vessel at the cross-sections was calculated by summing the distance between each of the points constituent the sections. The circumference was used in the calculation of the cyclic strain, no diameters or cross-sectional areas, as previously done by other researchers. They used the Green-Lagrange strain tensor to compute the circumferential cyclic strain,the following expression was used to calculate the circumferential cyclic strain:
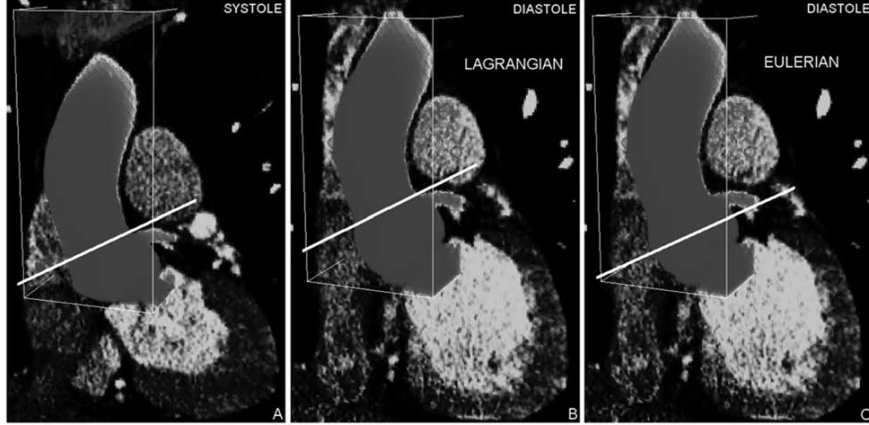
Figure 2.15: A partial three-dimensional volume-rendering of the ascending aorta is shown at (A) peak-systole, (B) end-diastole in the Lagrangian frame, and (C) end-diastole in the Eulerian frame. The white line is the segmentation plane aligned at the distal location of the left coronary artery in A and B. In C, the segmentation plane is fixed at the location from peak-systole, which does not capture the desired lumen boundary. Note that the volume of the left ventricle indicates the stage of the cardiac cycle. The figure is taken from the work of Morrison et al. (2009).

$$E_{\theta\theta} = \frac{1}{2}(\frac{C_S^2}{C_D^1} - 1) \tag{2.9}$$

with C_S and C_D respectively the systolic and the diastolic circumference.

To calculate the longitudinal cyclic strain they simply took the difference between the systolic and diastolic DTA lengths divided by the diastolic DTA length. They showed that the diameters of the thoracic aorta increased, on average, by 14% with age from the younger (mean age, 41 years) to the older (mean age, 68 years) group. Moreover they showed also that the circumferential cyclic strain of the thoracic aorta decreased, on average, by 55% with age from the younger to the older group, see table 2.7. Finally they measured that the diameters of the thoracic aorta decreased with aortic location for both patient populations but that circumferential cyclic strain did not, see figure 2.17.

Concluding they reported longitudinal cyclic strain of about 2% for the younger patients (one-quarter of the circumferential cyclic strain in the same group). They also showed that the longitudinal and circumferential cyclic strain at the DTA decreases by 50% with age. They moreover observed that the aorta enlarges between 10% to 15% with age and it also elongate of a similar amount. Finally they also understood that the circumferential strain does not vary down the length of the aorta and this implies a larger volumetric compliance in the proximal aorta with respect to the distal aorta. Discussing their results arises the fact that the observed deformation of the aorta is nonuniform and that heretofore no stent-graft compensates for nonuniform deformation or circumferential variations in cyclic strain of the thoracic aorta.
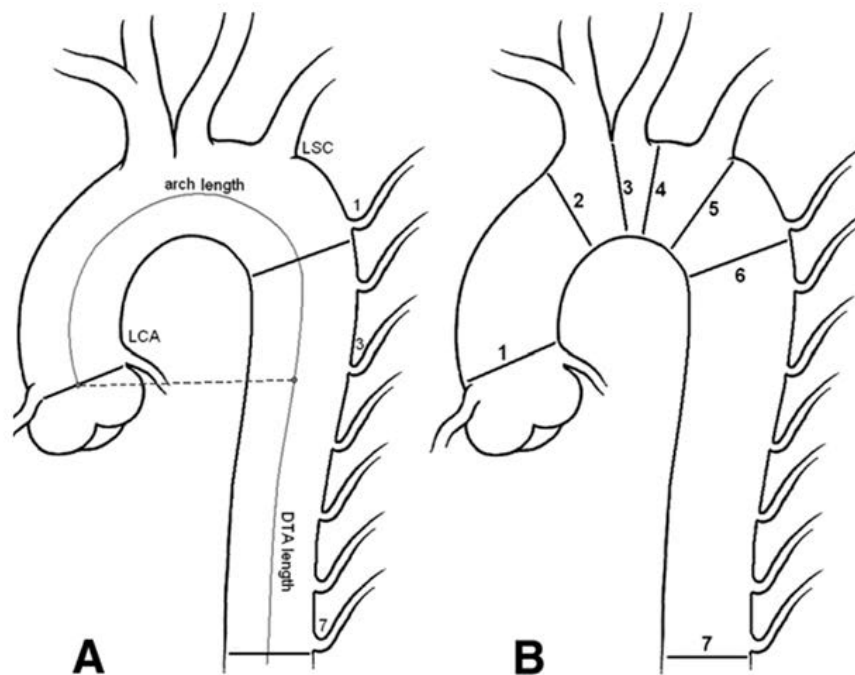
Figure 2.16: Displayed is a schematic of the thoracic aorta, where the branch vessels are drawn in-plane, which is not typical for patients. A, The labels for the left coronary artery (LCA), the left subclavian artery (LSC), the first, third, and seventh intercostal artery (ICA) are shown. The arch is defined from the LCA to the first ICA, while the descending thoracic aorta (DTA) is defined from the first to the seventh ICA. The dashed line represents the three-dimensional measurement of the relative deformation between the ascending and descending aorta. B, The numbers correspond to the locations along the arch and DTA where we quantified circumferential cyclic strain and systolic diameters. The figure is taken from the work of Morrison et al. (2009).

2.3 Open issues

We described in detail the state of the art concerning the morphological characterization of vascular networks exploiting static and dynamic medical images. What appears from this extensive review is that:

- quantitative reliable methods to automatically retrieve levels of interest along the aorta are missing;

- standard definitions of aortic cardiac changes, distensibility are missing;

- longitudinal cyclic strain characterization of the thoracic aorta is to be investigated;

Hereafter we discuss more in detail the findings just mentioned above. All the papers reported rely on the manual selection of aortic levels of interest and on their two-dimensional segmentation. This fact introduces high variability in dependency of the operator and on the medical image quality. In fact picking manually those regions introduce not negligible differences in measures

Table 2.7: The diameters and circumferential cyclic strains for the ascending aorta, the arch, and the descending aorta are reported for the younger and older groups. Values for P were computed between the younger and older group for each location using the paired t test. Each number, 1 to 7, corresponds to the aortic location shown in the figure 2.16. The table is taken from the work of Morrison et al. (2009).

Variable, mean ± SD	1	2	3	4	5	6	7
Diameter, mm							
Young	31.9 ± 4.7	31.1 ± 3.9	27.1 ± 1.7	25.2 ± 1.3	23.5 ± 1.1	22.8 ± 1.0	21.1 ± 1.4
Older	32.3 ± 4.3	34.7 ± 2.0	32.4 ± 3.6	29.1 ± 2.6	26.1 ± 2.5	26.6 ± 3.0	24.5 ± 2.8
P	= .56	= .11	<.05	<.01	<.05	<.05	<.05
Cyclic strain, %							
Young	10.3 ± 3.8	11.3 ± 6.9	8.8 ± 3.8	8.9 ± 3.5	7.9 ± 2.4	7.3 ± 2.6	8.1 ± 3.3
Older	2.6 ± 1.2	3.4 ± 1.5	1.6 ± 1.4	2.7 ± 1.4	2.0 ± 2.0	2.7 ± 1.3	4.2 ± 1.9
P	<.01	<.01	<.01	<.01	<.001	<.01	<.01

and in comparing same levels of interest between pre- post-TEVAR models. Moreover there is a lack of investigation concerning the ascending aorta. This region has instead to be investigated carefully since by visual inspection at different cardiac cycle steps it is possible to observe large axial deformation and rigid-body motion. In addiction more studies need to be addressed on data-set composed by aneurysmatic and dissected patients, as well as on data-set composed by patients who undergo traumatic injuries or composed by healthy patients of whom no significant, extensive, and reliable aortic dynamic changes data are, to the best of our knowledge, nowadays present. Currently available information are limited and conflicting. Results showed by Muhs et al. (2006) and by van Prehn et al. (2007) are slightly different from those reported by Morrison et al. (2009). For example, in the work of Mush - no age for patients is reported - they yielded a 10% changes in diameter in the descending thoracic aorta, which correlated with the findings of Morrison for the younger group of patients but that is 50% larger than the values measured by Morrison for the elder group of patients. Moreover in the work of van Prehn their diameter changes in the ascending aorta in 15 patients (mean age 72 years old) resulted in larger values than those computed by Morrison et al. (2009).

Many studies focused their attention on the quantification of the diameter along the major axis and this does not take into consideration that the aorta may have a non circular shape but more likely an elliptical one. This also can lead to the fact that the aorta does not behave in a uniform way but that it shows nonuniform horizontal deformation or variation during the cardiac cycle.

A remarkable aspect arises from the previous literature review. None of the paper cited exception made for the work of Morrison et al. (2009) investigated the longitudinal cyclic aortic changes. This aspect need to be investigated more in detail as stent-graft deployment may change dynamic of the aorta not only horizontally but also longitudinally being the aorta a complex
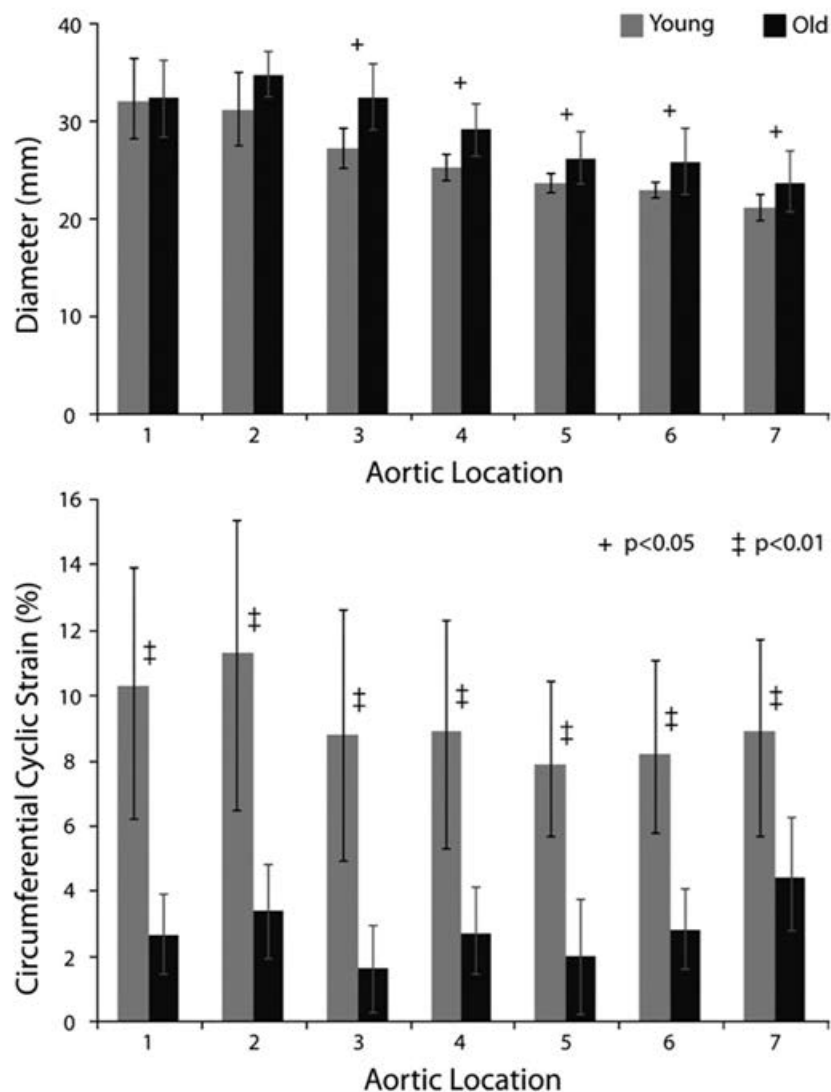
Figure 2.17: Top, Data for diameters along the thoracic aorta at seven locations are given with the standard deviation. The light bars correspond to the younger patients and dark to the older patients. The diameters in the older group are statistically larger that the younger group at all locations except for the left coronary artery and the brachiocephalic trunk (BRC). The decrease in diameters along the aorta indicates the tapering of the aorta in both populations. Bottom, The circumferential cyclic strain along the thoracic aorta at seven locations is presented with the standard deviation. The cyclic strain is significantly smaller in the older patient population and is not statistically different along the length of the aorta in either group. The figure is taken from the work of Morrison et al. (2009).

dynamic environment.

Finally emerges from a paper of Kaladji et al. (2013) an interesting finding. To calculate aortic lengths and diameters and overcome the hazard of shortening inherent to axial imaging, a centerline extraction is useful in order to estimate true vessel length. This method is widely

used and is generally adopted as the "gold standard". Nevertheless, it is observable that thoracic endovascular aortic repair (TEVAR) distal landing zones do not always lie where the centerline-based plan might predict. The usual error is that the length of the stent-graft is shorter than the length planned. This phenomenon has been previously described in abdominal EVAR (White et al., 1999). Potential explanations include shortening of the endograft during deployment and the geometric consequences of the curvature of the thoracic aorta. Previous investigators have shown that there is a difference between aortic length estimated using a centerline reconstruction from that obtained by measuring along the aortic wall, see work of Wörz et al. (2010). In the study of Kaladji et al. (2013) they collected retrospectively 74 patients, who underwent TEVAR. All CTA were analysed with EndoSize software using automatically extracted centerlines. For each case, a proximal and distal landmark was placed on the centerline corresponding to the distal and proximal ends of the endograft. They performed three measurements between these landmarks (see figure 2.18): the centerline length (green in figure 2.18), the straightline (red in figure 2.18) length and the outer curvature length (blue in figure 2.18). The software computed automatically the measured of distance. The outer curvature length is calculated using a virtual endograft (circular tube), which is constrained on the centerline. The outer curvature length is then automatically computed by the maximal path along the tube. For each patient the diameter of this virtual endograft was calculated using the diameter of the implanted endograft.

There was a statistically significant difference in the lengths measured using centerlines (135.4 $\pm$ 24 mm) compared with that of the endografts (160 $\pm$ 29 mm) ($p < .0001$). The mean difference between the centerline length and the endograft length was 24.6 ± 11 mm (range, 1 - 50 mm). The "industry standard" for the estimation of aortic length uses corrected centerline extraction. This method has limitations and the apparent aortic length varies depending on how it is measured - centerline of flow, inner or outer wall measurements. There are potentially important differences between the apparent length estimated using centerlines and those measured from the outer wall. In the study of Kaladji et al. (2013) this difference has been measured to be as much as 50 mm. The majority of sizing of complex endografts is performed in the manufacturers' planning centres. In the near future, with the release of "off-the-shelf" fenestrated and branched endografts, surgeons will have to perform their own complex sizing, particularly in the management of emergencies. Therefore, these measurement subtleties must be recognized and sizing tools that take them into account are required.
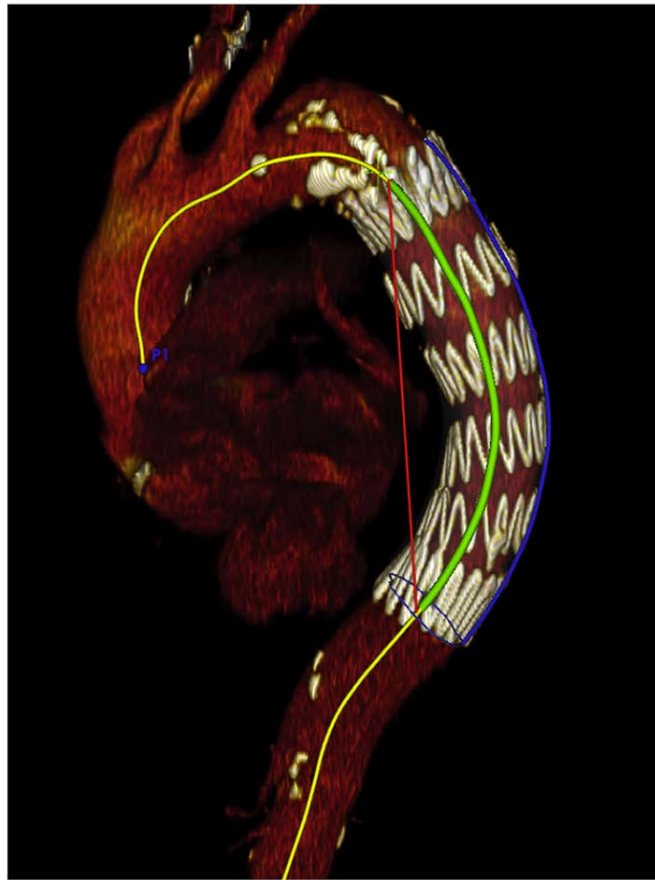
Figure 2.18: The EndoSize software calculates three lengths: the straight line (red), the centerline (green) and the outer line (blue). P1 is the start of the centerline. Figure is taken from the work of Kaladji et al. (2013).

Chapter 3

Three-dimensional aortic model: from images to patient specific 3D reconstruction

3.1 Image pre-processing: enhancement techniques

Image enhancement techniques are used to improve the quality of digitally stored images so that image features can be perceived easier by the human visual system or can be detected by an automatic image analysis system. Image enhancement can highlight image details that in the original image are not easily or not at all recognizable. This is the case for example of images affected by artifacts that mask important image features, or when image is affected by noise, or finally when the contrast is not sufficient to recognize the structure of interest (Bankman, 2008). Enhancement techniques act a transformation or a mapping of the original image and give back a new image with the produced modifications. It is remarkable that the result of image enhancement can be the same for different starting images; this lead to the consideration that image enhancing could be not reversible. It is also relevant that often image enhancement of certain features in the images can produce not desirable effects. Important features may be lost or the resulting image could be of poor interest with respect to the original one. Furthermore it has to be remarked that only features already present in the original image can be enhanced. If the image does not contain the features we are highlighting then only not desirable effects will appear on the processed image such as noise or blur.

Computed tomography Imaging, available today in clinical settings, are capable to carry information about the anatomy with high resolution (sub-millimetric). In the continuous space an

image can be defined as a function $I(\mathbf{x})$ from $\mathbb{R}^3 \rightarrow \mathbb{R}$; i.e., to any point $\mathbf{x}$ in the domain $\mathbb{R}^3$ (the spatial coordinates) I associates a scalar value called the intensity or grey level of the image at that point. A digital image is, therefore, an array of numbers that represents the distribution of the continuous signal both in space and intensity.
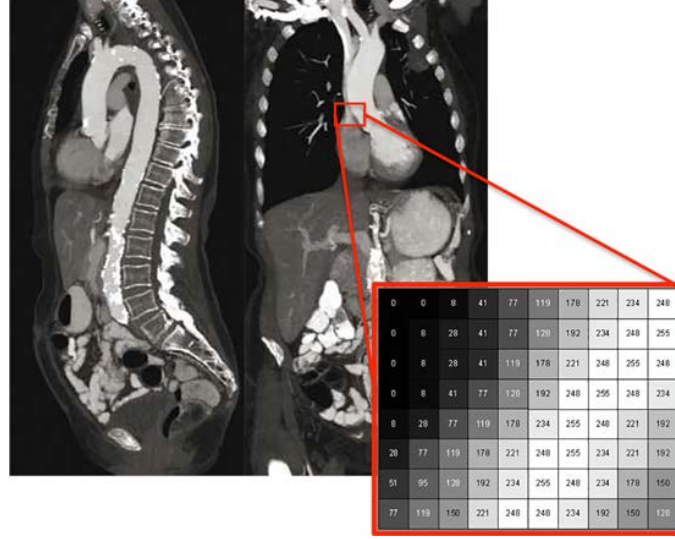
Figure 3.1: Computed tomography angiography (CTA) of the chest and abdomen. The image is composed by a large serial 3D array of data values, defined as $I(\mathbf{x})$, where $\mathbf{x} \in \mathbb{R}^3$ are the spatial (plane) coordinates, and the amplitude of I at any coordinates $\mathbf{x}$ is called the intensity or grey level of the image at that point.

In the discrete space, a digital image is a function $I(m,n)$ where I is the intensity of the pixel and m and n define the position of the pixels in the image grid composed by M rows and N columns. The intensity levels or grey levels of the image are quantized into P discrete levels form 0 to $P-1$, to each couple (m,n) corresponds its discrete P grey level. A commonly used quantity in image enhancement is the histogram of the image. The histogram of a digital image is a operator that counts the number of pixels in the image that have the same intensity level. It is defined as follows:

$$h(i) = \sum_{m=0}^{M-1} \sum_{n=0}^{N-1} \delta(I(\mathbf{m},\mathbf{n}) - i) \qquad i = 0, 1, \ldots, P-1 \qquad (3.1)$$

where

$$\delta(w) = \begin{cases} 1 & \text{if } w = 0, \\ 0 & \text{otherwise,} \end{cases}$$

Methods for image enhancing are primarily based on two categories, one that operates on pixels and the other that operates locally. For our purpose we will use only the local operators. Local operators act on the original image pixel by pixel providing a new value for each pixel based

on the value of the pixel itself and the value of its neighbours. Local operators may be linear or non-linear, these type of local filters are obtained through the convolution of the image with a matrix called *kernel*

3.1.1 Mean filtering

Mean filtering is a local operator technique to suppress noise. In fact mean filtering is achieved by the convolution of the image with a kernel of dimension $(2K + 1, 2L + 1)$ where each coefficient has the value equal to the reciprocal of the number of the coefficients in the kernel. A convolution is done by multiplying a pixel and its neighbouring pixels by a matrix, called kernel. Differently sized kernels containing different patterns of numbers produce different results under convolution. The size of a kernel is arbitrary but 3×3 is often used For example when $K = L = 2$ we obtain:

$$w(k,l) = \begin{pmatrix} 1/9 & 1/9 & 1/9 \\ 1/9 & 1/9 & 1/9 \\ 1/9 & 1/9 & 1/9 \end{pmatrix}$$

that is the 3×3 kernel or mask to be convolved with the image, see figure 3.2 panel (c). This type of filter is in a way a smoothing filter and is effective to reduce noise but on the other side it can affect the sharpness of the edges, see figure 3.2 panel (d).
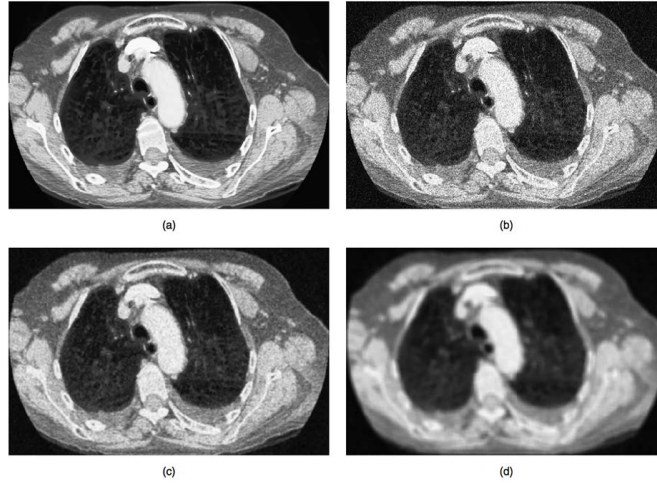
Figure 3.2: (a) Original CT image. (b) Original image in (a) corrupted by added Gaussian white noise with maximum amplitude of ± 25 gray levels. (c) Image in (b) convolved with the 3×3 mean filter. The mean filter clearly removes some of the additive noise; however, significant blurring also occurs. This image would not have significant clinical value. (d) Image in (b) convolved with the 9×9 mean filter. This filter has removed almost all the effects of the additive noise (Courtesy of Ms. Bonnie Cameron, MRT and Dr. Paul Schulte, Regina General Hospital) Bankman (2008).

3.1.2 Median filtering

Median filtering is a non-linear filter used to suppress noise as the mean filter operator does (Bankman, 2008). It operates differently from the mean filtering operator, as it is not the convolution of the kernel with the image. It rather return an output image that has in each pixel the median of the intensity values of the pixels covered with the kernel and this value is positioned in the output image at the coordinate representing the center of the kernel. Median filters do not have the same characteristics of smoothing that mean filters have. Features smaller than half of the size of the kernel are completely removed and large discontinuities (edges or changes in image intensity) are not affected by the usage of the median filter in term of grey scale values but could be shifted by some pixels. Median filter is really useful to remove salt-and-pepper kind of noise.
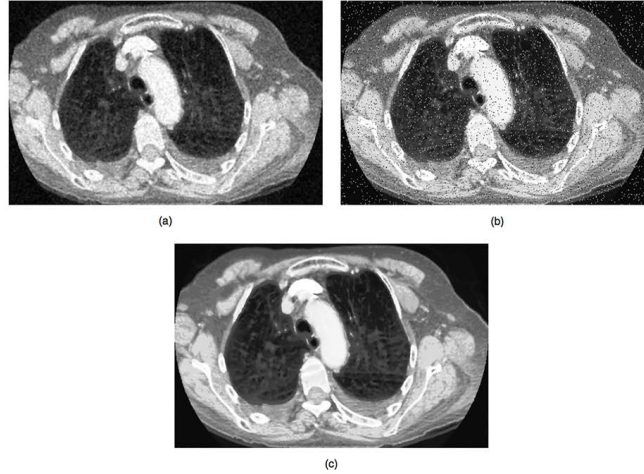
Figure 3.3: (a) Image in figure 3.2 (b) enhanced with a 3×3 median filter. The median filter is not as effective in noise removal as the mean filter of the same size; however, edges are not as severely degraded by the median filter. (b) Image in figure 3.2 (a) with added "salt-and-pepper" noise. (c) Image in (b) enhanced by a 3×3 median filter. The median filter is able to significantly enhance this image, allowing almost all noise to be eliminated (Courtesy of Ms. Bonnie Cameron, MRT and Dr. Paul Schulte, Regina General Hospital) (Bankman, 2008).

3.2 Level sets segmentation

In the field of image processing many algorithms have been developed to segment anatomical structures of interest. Segmentation is ideally the full separation of a structure of interest from the background and it is essential for visualization and for further analysis of anatomical region of interest. Segmentation methods can be divided in two categories: region-based methods (Cohen et al., 1993) (Chan et al., 2001) which are based on the intensity values of the image, and edge-based methods (Kass et al., 1988) (Sethian, 1999b) which are based on the identification of image edges. We here decide to exploit an edge-based approach and in particular, the level set method

proposed in Antiga (2002a), and we customize the initialization of the level sets evolution equation in order to adapt it specifically to the segmentation of the thoracic aorta and its side-branches.

Before moving to the description of the method, since it is an edge-based approach, let introduce how edge of an image are detected.

Edge detection

Edge detection is the name for a set of mathematical methods which aim at identifying points in a digital image at which the image brightness changes sharply or, more formally, has discontinuities. The points at which image brightness changes sharply are typically organized into a set of curved line segments termed edges. Edge detection is a fundamental tool in image processing, machine vision and computer vision, particularly in the areas of feature detection and feature extraction.

There are many methods for edge detection, but most of them can be grouped into two categories, search-based and zero-crossing based. The search-based methods detect edges by first computing a measure of edge strength, usually a first-order derivative expression such as the gradient magnitude, and then searching for local directional maxima of the gradient magnitude using a computed estimate of the local orientation of the edge, usually the gradient direction. The zero-crossing based methods search for zero crossings in a second-order derivative expression computed from the image in order to find edges, usually the zero-crossings of the Laplacian or the zero-crossings of a non-linear differential expression. As a pre-processing step to edge detection, a smoothing stage, typically Gaussian smoothing, is almost always applied to reduce noise present in the image. Let describe more in detail the search-based method that will be exploited later and in particular the gradient magnitude.

The gradient for a function $I(\mathbf{x})$ at coordinates $\mathbf{x}$ is given by the column vector:

$$\nabla I = \begin{pmatrix} G_x \\ G_y \\ G_z \end{pmatrix} \begin{pmatrix} \partial I/\partial x \\ \partial I/\partial y \\ \partial I/\partial z \end{pmatrix}$$

the magnitude of this vector is given by

$$\|\nabla I\| = mag(\nabla I) = (G_x^2 + G_y^2 + G_z^2)^{1/2} = ((\partial I/\partial x)^2 + (\partial I/\partial y)^2 + (\partial I/\partial z)^2)^{1/2}$$

Different gradient operators can be applied to estimate image gradients from the input image or a smoothed version of it. The simplest approach is to use central differences, that correspond to the application of filter masks to the image data. First-order difference operators for estimating image gradient have been proposed by Sobel, Prewitt, Roberts, and Frei-Chen, just to cite the most famous (Ziou et al., 1998).

Examples of 3×3 mask for horizontal gradient estimation - see figure 3.4 b - ($w_h(k,l)$, where k and l are numbers of kernel rows and columns) are:

$$w_{h1}(k,l) = \begin{vmatrix} 1 & 1 & 1 \\ 0 & 0 & 0 \\ -1 & -1 & -1 \end{vmatrix} \tag{3.2}$$

$$w_{h2}(k,l) = \begin{vmatrix} -1 & -1 & -1 \\ 0 & 0 & 0 \\ 1 & 1 & 1 \end{vmatrix} \tag{3.3}$$

Examples of 3×3 mask for vertical gradient estimation - see figure 3.4 c -($w_v(k,l)$, where k and l are numbers of kernel rows and columns) are:

$$w_{v1}(k,l) = \begin{vmatrix} 1 & 0 & -1 \\ 1 & 0 & -1 \\ 1 & 0 & -1 \end{vmatrix} \tag{3.4}$$

$$w_{v2}(k,l) = \begin{vmatrix} -1 & 0 & 1 \\ -1 & 0 & 1 \\ -1 & 0 & 1 \end{vmatrix} \tag{3.5}$$
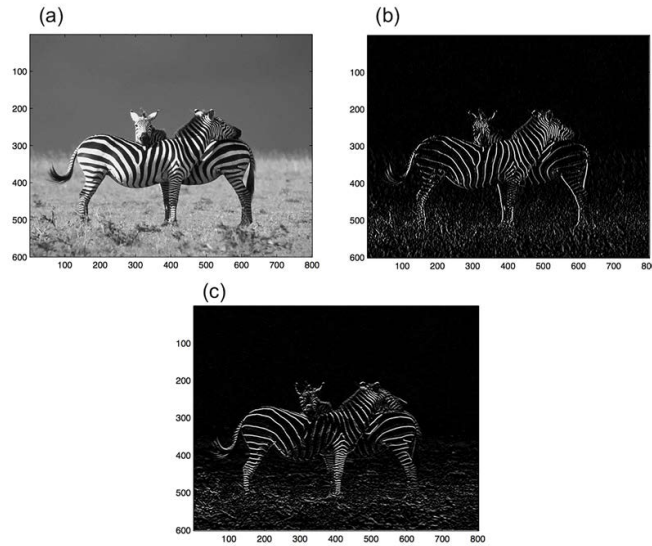
Figure 3.4: (a) The original image. (b) Original image convolved with a 3×3 mask for horizontal edges and lines enhancement 3.3. (c) Original image convolved with a 3×3 mask for vertical edges and lines enhancement 3.5.
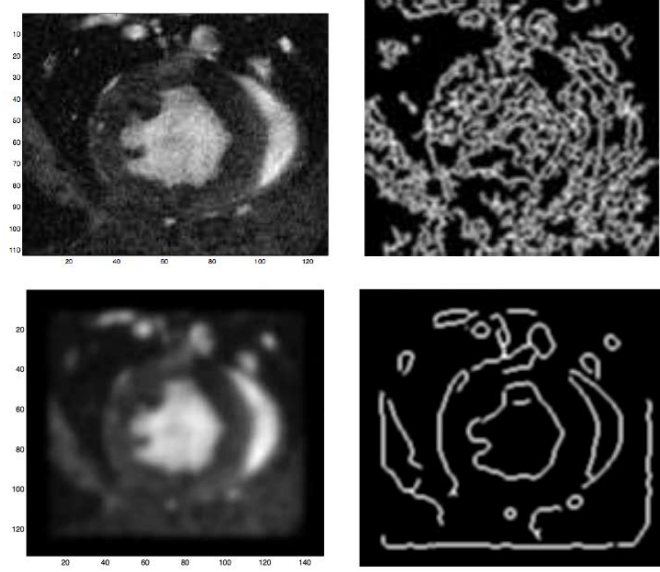
Figure 3.5: The original image on the left side. On top the original image is not filtered while in the bottom side the original image is filtered to reduce noise. The original image is convolved with a mask for edges and lines enhancement (right side). In the convolved image on top right side is visible that edge detection fails to detect the edged we are interested in, instead in bottom image right side it is clearly visible how contour of the structures in the original image (bottom left side) are highlighted correctly.

Now that the key ingredient to compute the edges of an image are introduced, let describe more in detail the segmentation technique itself. The idea behind this technique is that the surface of interest can be represented as the isosurface of level k of a scalar function (Sethian, 1999b). In particular, a surface evolving in time

$$S : \mathbb{R}^2 \times \mathbb{R} \to \mathbb{R}^3,$$

can be represented as an isosurface of level k of a time dependent scalar function

$$\Phi(\mathbf{x}, t) : \mathbb{R}^3 \times \mathbb{R} \to \mathbb{R}.$$

so that

$$S(t) := \left\{ \mathbf{x} \in \mathbb{R}^3 \mid \Phi(\mathbf{x}, t) = k \right\}. \tag{3.6}$$

is the k *level set* of $\Phi(\mathbf{x}, t)$. In particular we choose $k = 0$.

Following Antiga (2002b), the following evolution equation should be solved:

$$\begin{cases} \dfrac{\partial \Phi}{\partial t}(\mathbf{x}, t) = -w_1 G(\mathbf{x}) \|\nabla \Phi\| + 2w_2 H(\mathbf{x}) \|\nabla \Phi\| + w_3 \nabla P(\mathbf{x}) \cdot \nabla \Phi, & (\mathbf{x}, t) \in \mathbb{R}^3 \times [0, T], \\ \Phi(\mathbf{x}, 0) = \Phi_0(\mathbf{x}), & \mathbf{x} \in \mathbb{R}^3, \end{cases} \tag{3.7}$$

coupled with suitable boundary conditions and, as initial condition, the *signed distance function*

$$
\Phi_0(\mathbf{x}) = \begin{cases} -D_0(\mathbf{x}) & \text{if } \mathbf{x} \text{ is inside } S(0), \\ +D_0(\mathbf{x}) & \text{if } \mathbf{x} \text{ is outside } S(0), \\ 0 & \text{if } \mathbf{x} \in S(0), \end{cases}
$$

where $D_0(\mathbf{x}) = \min_{\mathbf{y} \in S(0)}\{\|\mathbf{x} - \mathbf{y}\|\}$, see figure 3.6.
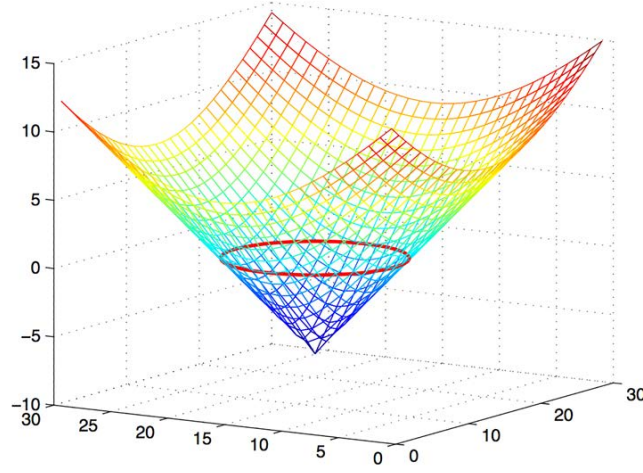
Figure 3.6: An example of signed distance, a two-dimensional curve embedded within a three-dimensional surface. To illustrate this point, figure shows the segmentation boundary (red circle) as part of a surface where the contour level is d, i.e., the d-th level set.

In particular:

- w_1, w_2, w_3 are user-defined weights;

- the function $G(\mathbf{x})$ is defined as:

$$
G(\mathbf{x}) = \frac{1}{1 + \|\nabla I(\mathbf{x})\|}.
$$

and is called *inflation speed*. The term $-w_1 G(\mathbf{x}) \|\nabla \Phi\|$ is an inflation term. The surface expands along $\|\nabla \Phi(\mathbf{x})\|$, which is the direction normal to the zero level of Φ, with velocity proportional to $G(\mathbf{x})$. The inflation speed is lower when image gradient is higher, so that it is approximately equal to one (maximum value) inside the vessel and negligible near the edges.

- the function $H(\mathbf{x})$ is defined as:

$$H(\mathbf{x}) = \nabla \cdot \left(\frac{\nabla \Phi}{\|\nabla \Phi\|} \right),$$

and is equal to the curvature of the zero level set of $\Phi(\mathbf{x})$. The term $2w_2 H(\mathbf{x}) \|\nabla \Phi\|$ is a penalization term to guarantee the smoothness of the surface, penalizing high curvatures.

- the function $P(\mathbf{x})$ is defined as:

$$P(\mathbf{x}) = -\|\nabla I(\mathbf{x})\|$$

and is called *attraction potential*. The term $w_3 \nabla P(\mathbf{x}) \cdot \nabla \Phi$ defines a convective term that drives the surface towards the edges.

The solution of this problem in `vmtk` is performed by the script `vmtklevelsetsegmentation`.

3.2.1 Custom segmentation initialization: colliding fronts

The choice of an initial level set function $\Phi(0) = \Phi_0$ is a key step for this segmentation strategy. We need to initialize Φ_0 and then let it evolves through the level set evolving equation already described.

The adopted initialization is the colliding front initialization (Antiga, 2002a) (Antiga, 2002b), that is specific for the purpose of vessel segmentation. The operator selects two seed points (P_1 and P_2) on the image, inside the vessel. The selection of the seeds accounts for the most critical part in which user-defined input and experience is required. The extraction of the portion of vessel between these seeds is then computed through propagation of two independent wave fronts, starting respectively from each seeds, with speed proportional to local image intensity. The Eikonal equation is used to tackle this purpose (Sethian, 1999a)

$$\|\nabla T_i(\mathbf{x})\| = \frac{1}{1 + I(\mathbf{x})}, \quad T_i(\mathbf{P}_i) = 0$$

We refer as $T_i(x)$ the travel time of a wave propagating from $P_i, i = 1, 2$ and traveling with velocity equal to $I(x)$ (the intensity of the image, i.e. the wave has velocity higher where the image is brighter, as for vessels). Once the travel times T_1 and T_2 have been computed, the initial level set function is defined as

$$\Phi_0(\mathbf{x}) := \nabla T_1 \cdot \nabla T_2. \tag{3.8}$$

its value is negative when the two waves travel in opposite direction and positive otherwise, see figure 3.7. $\Phi_0 \geqslant 0$ on the lumen boundary since $I(x)$, that drives the speed of propagation of the waves, undergoes a strong decrease in speed precisely at the lumen boundary. This property

of Φ_0 at the lumen boundary permit to initialize the surface of the vessel in close proximity to the boundary of the lumen, especially for high enhanced vessel with respect to background. When the signal-to-background ratio is not high, the slowdown of the wave front at the lumen boundary might be not sufficient to initialize properly the vessel. In this case, the set-up of a threshold to guide the wave propagation within a range of intensity would be desirable.

Figure 3.7: Colliding fronts initialization. Negative where the two waves travel in opposite direction (the first approximation of the vessel), positive otherwise (in particular, side branches which are thus excluded).
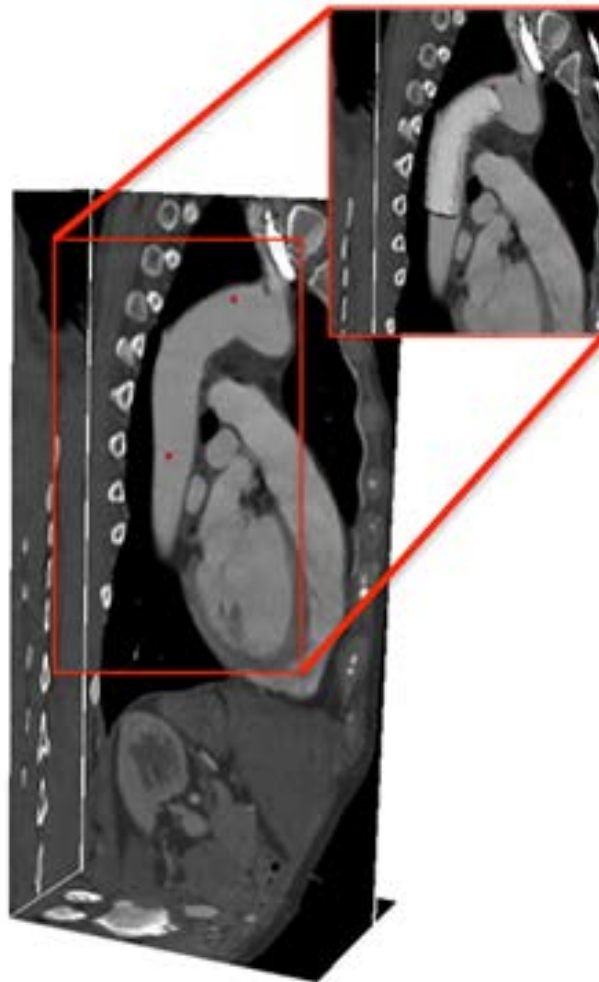
Figure 3.8: Colliding fronts initialization. On figure the two seeds from which the colliding fronts will propagate are depicted (red dots). The red box is highlighted and the colliding front initialization between the two seeds is showed.
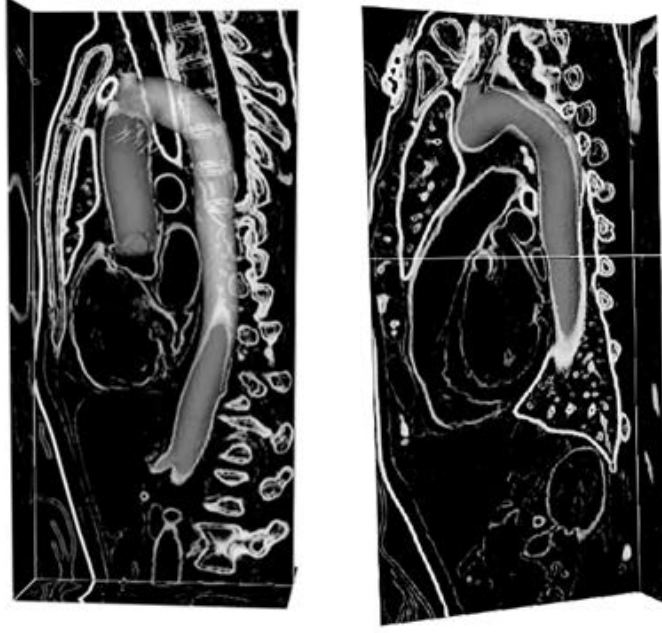
Figure 3.9: Segmentation procedure. The iso-surface of level zero is depicted on the image convolved with an edge detecting filter. It is possible to recognize immediately the anatomical structures of interest, in this case the thoracic aorta thanks to edge detection.

Dealing with large 4-dimensional dataset of the thoracic aorta arises three major problems intrinsic to the anatomy of the vessel under investigation and to the segmentation procedure.

First of all it is worth remarking that side branches, if present, are automatically excluded form the initialization, since the two fronts enter in side branches travelling in the same direction and therefore equation 3.8 becomes positive. This fact is a disadvantage when dealing with the thoracic aorta anatomy that, as described in chapter 1, is characterized by four major side branches, i.e. - the brachiocephalic trunk, the left common carotid artery, the left subclavian artery, and the celiac artery. In this case the user would perform an initialization for each side branch leading to an increase in the workload and time related to segmentation procedure. Moreover,the problems related to the segmentation technique are one related to the cost in term of time required to segment individually eight time steps pre- and post-operative and the other related to the user intra- and inter-variability more likely to be introduced in this particular type of 4-dimensionally characterized data. We therefore develop a method to avoid those drawbacks in an intuitive manner, tailored on the thoracic aortic shape. We decide to customise the initialisation step changing a vmtk class in order to run directly with seven seed points: the script performs a bunch of initialisations looping from the first seed point to the last and vice versa. Using seven seed points (red dots in Fig. 3.10) it is possible to gather the level set of the entire aorta in one shot, leaving the possibility to detail it better in subsequent steps, if necessary. We define and compute

the following function

$$F_k(\mathbf{x}) = \sum_{i=k}^{k+1} \sum_{j=k}^{k+1} \nabla T_i \cdot \nabla T_j, \qquad i \neq j$$

where $k = 1, \ldots, 6$ and i and j represents the user defined seeds from where the bunch of initialisations are performed. Once $F_k(\mathbf{x})$ is computed we take

$$\min_{\mathbf{x} \in \mathbb{R}^3} \{F_1(\mathbf{x}), \ldots, F_6(\mathbf{x})\}$$

to be sure to obtain a function that is negative inside the vessel and positive outside, equation 3.7 is evolved with parameters $w_1 = 0.4$, $w_2 = 0.4$ and $w_3 = 1.0$ in order to obtain the level set representing the first time instant of our 4-dimensional dataset (Fig. 3.10, right side).
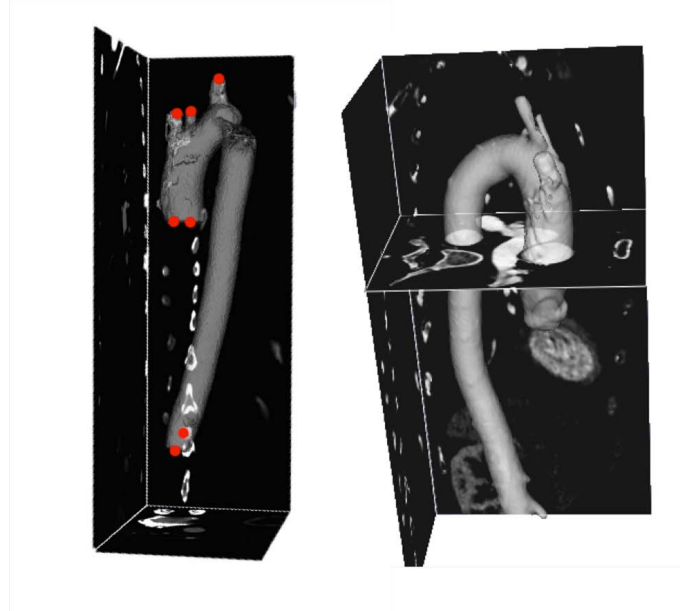
Figure 3.10: Segmentation procedure. The user puts seven seed points on the image (red dots) to initialise the aorta segmentation in one shot. Figure on the left side depicts, on the image grid, the apposition of the seven seed points and zero level of initial φ_0. Figure on the right side depicts on the image grid the final zero-level of $\varphi(x)$ obtained with parameters $w_1 = 0.4$, $w_2 = 0.4$, and $w_3 = 1.0$.

3.2.2   Initial level sets: shift

The level set produced as output after the performed custom initialisation is the representation of one time instant among the eight that constitute the dataset we have to study.

Starting from two main considerations:

- the aortic arch initialisation produced is a signed distance function, which means that it is negative inside the vessel, positive outside and zero on the boundary,
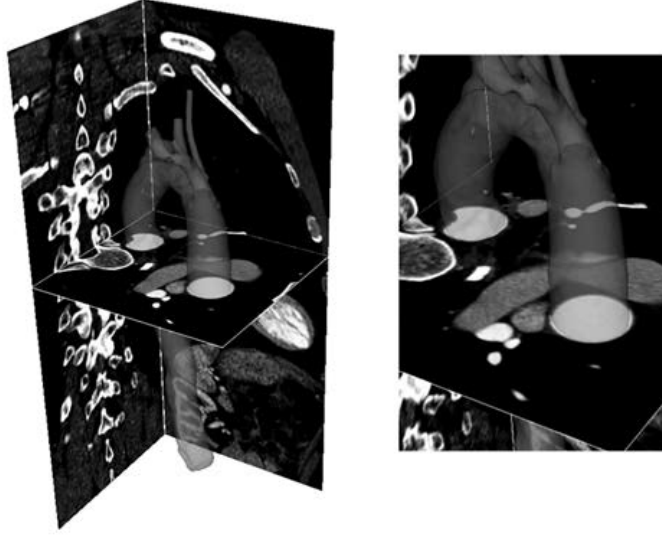
Figure 3.11: The evolved $\Phi_0(\mathbf{x})$ is shifted of 1 mm inside the vessel on the image grid. Here is depicted an example of shifting procedure.

- two subsequent time instants do not experience high changes of position,

it is possible to exploit both and develop a technique to shrink the level set of a time instant and reuse it to initialise the subsequent time instant being sure that it will entirely fall inside its boundaries.

The resulting level set is therefore shifted of 1 mm inside the vessel, see figure 3.11, and used as initial level set for the subsequent time instant, for which the evolution equation is run with the same parameters w1, w2 and w3. This process is automatically repeated for each time step allowing the reduction of the workload and the user interaction. In Fig. 3.12 a representation of the segmentation steps is depicted. This technique presents robustness and repeatability on one hand, and efficiency on the other. In particular, we aimed at satisfying the following criteria:

- minimize the operator demanding tasks, while maintaining the flexibility of the tool in certain context (e.g. - the choice of the number of seeds for the initialization);

- reduce the number of free parameters to be specified by the user, fix them based on past experience and propagate them through the time steps, so that the operator is facilitated in taking decisions.
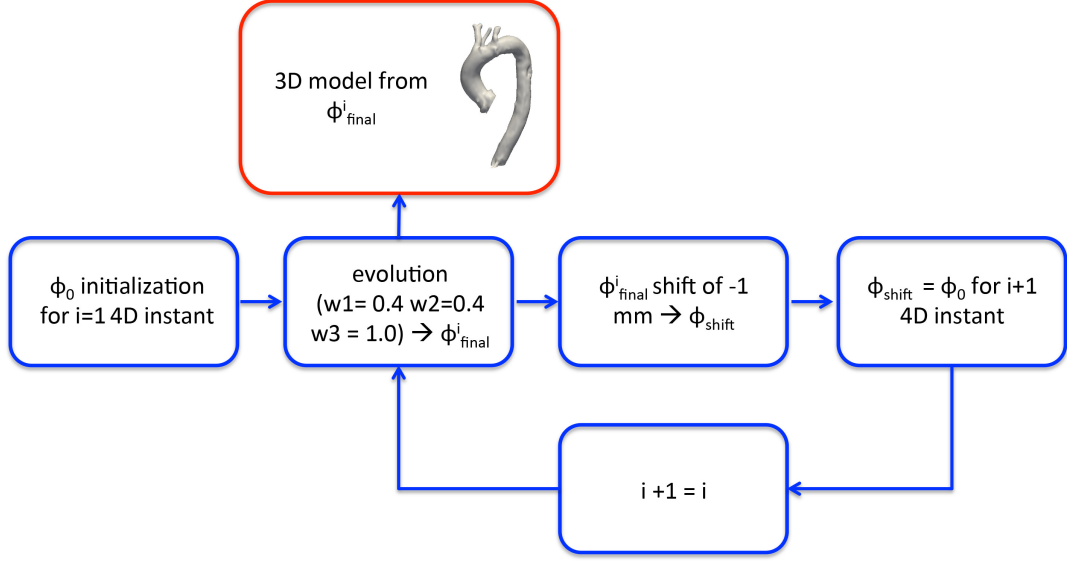
Figure 3.12: 4D segmentation workflow: from the initialisation of $\Phi_0(\mathbf{x})$ to the generation of the 3D geometric model. We initialise $\Phi_0(\mathbf{x})$ only for the first time instant of the 4-dimensional dataset. Once the initialisation is performed we let it evolves with parameters $w_1 = 0.4$, $w_2 = 0.4$ and $w_3 = 1.0$. The evolved $\Phi_0(\mathbf{x})$ is shifted of 1 mm inside the vessel on the image grid and is used as initial level set for the subsequent time instant.

3.3   3D model surface fairing and optimization: smoothing and remeshing

Once segmentation has been performed, the zero level set surface can be extracted using the Marching Cubes algorithm (Lorensen and Cline, 1987). This algorithm creates a polygonal surface located at a specific scalar value from a 3D array of data (image). Its formulation dates back to 1987, however this algorithm is still commonly used in a variety of fields, and represents a gold standard for the creation of a surface model from the 3D data. The Marching Cubes algorithm returns a polygonal surface i.e. an initial triangular mesh τ_0.

Models obtained with reconstruction techniques such as level sets, balloon or Marching Cubes (iso-level reconstruction algorithm) are not directly suitable for geometric analysis. Most of the time, imaging artifacts can create region of irregularities on the reconstructed model. In fact deformable models, since are based on image gradient, tend to be disturbed by image gradient closer,

both in intensity and spatially, to the region of interest in which level sets have to be initialized. The activation of the curvature term in level sets evolution equation 3.7 limits this effect, and it can eventually prevent it, but the price to pay is global loss of model detail. The solution to these problems requires either the imposition of modeling constraints in the reconstruction phase, or the use of techniques which allow to edit the reconstructed models - i.e. fairing techniques. We therefore introduce techniques based on the usage of smoothing filters and remeshing operations.

We decide to apply a global smoothing filter based on the algorithm described by Taubin et al. (1996). Most of the existing smoothing methods are affected by the problem of shrinkage and this is evident the most when applied iteratively and a large number of times, we chose the method described in Taubin et al. (1996) because it is not affected by shrinkage related problems.

Moreover we perform the remeshing operation on the reconstructed model. These methods produce a new mesh τ that has to maintains the topological characteristics of the original mesh τ_0 but that has high quality triangles and well organized vertices. The algorithm used in this work progressively modifies the initial mesh τ_0 in order to conform imposed quality and sizing criteria. Mesh improvement is carried on with a set of three elementary topological operations, i.e. edge collapse, edge split, and edge swap (performed on surface triangles) and with a geometric operation, point relocation (performed on point position).

All the algorithms here briefly described and used are implemented in *vmtk* and well detailed in the work of Antiga (2002a).

Chapter 4

Automatic tool for geometric characterization of thoracic aorta

4.1 Introduction

There is a considerable amount of literature supporting the evidence that the aorta undergoes dynamic changes during the cardiac cycle, especially at the level of the thoracic aorta and in particular from the sino-tubular junction (STJ) to the left subclavian artery (LSA) (Van Keulen et al., 2009) (van Herwaarden et al., 2006) (van Prehn et al., 2007) (Muhs et al., 2006). Therefore, the characterization of vessel geometry from medical images is a fundamental step for a better understanding of aortic dynamic changes in particular for those patients who underwent endovascular surgery, in particular Thoracic EndoVascular Aortic Repair (TEVAR), that can affect aortic dynamic and surgery follow-up.

Geometrical analysis of the thoracic aorta is in general a challenging task both for the anatomical variability of in vivo morphology and for the copious quantitative measures of interest potentially available. Nevertheless geometrical analysis can shade light on the behavior of the aorta during the entire heart cycle and can be useful for the clinicians in order to better understand how stent-graft geometry and deployment can affect pathological aortas and their dynamics.

In order to carry on the pipeline object of this work, we develop an automatic framework that requires a robust geometrical characterization, so that operations can be performed robustly and with minimal or no user interaction. In our framework the geometric analysis relies on calculation of the centerline of the vessel. The following chapter is dedicated in detail to the description of the automatic framework in particular to the method used for the computation of the geometric features of the thoracic aorta.

4.2   Vessel topology characterization

4.2.1   Centerline calculation and treatment

Once the 3D reconstructed model is obtained, for the purpose of our analysis, we need a synthetic descriptor of the vessel lumen geometry, which is not the surface itself.

When dealing with blood vessels and for the purpose of further analysis it is of paramount importance to search for a robust, unique, and simple way of synthesize the peculiar characteristics of the complex vascular network.

The ideal descriptor is the centerline of the vessel, defined as the line drawn between an inflow section and multiple outflow sections of a vessel that locally maximizes the distance from the vessel's wall.

From the definition of centerline it is worth noting that its calculation can be carry out solving a problem of energy minimization. We therefore look for a path $C(s)$, where s is the arch length or curvilinear abscissa, between two points p_0 and p_1 that minimize the following energy functional:

$$E_{centerline}(C(s)) = \int_0^L F(C(s))ds \tag{4.1}$$

where $F(x)$ is a cost function which has to be properly defined. This method resembles to the formulation of the snake evolution, a parametric method for image segmentation, which deals with the idea of finding the path between two points that minimizes some criterion in this case the energy functional.

For the choice of $F(C(s))$ we follow the work of Antiga et al. (2003), this method is based on the concepts of medial axis, Voronoi diagram, and wave propagation.

Given the importance of the centerline for this work, we here recall briefly the theory behind the definition of the functional in 4.1. Let define $\Omega \in R^3$, the volume of interest with boundary $\partial\Omega$. For any point $\mathbf{x}$ in Ω we exploit the concept of distance transform, interpreted as the distance of a point $\mathbf{x}$ from its nearest boundary point,

$$DT(\mathbf{x}) = \min_{\mathbf{y}\in\partial\Omega}\{dist(\mathbf{x},\mathbf{y})\} \tag{4.2}$$

where $dist$ is the Euclidean distance.

The definition of the distance transform $DT(\mathbf{x})$ is convenient to introduce the concept of *medial axis MA(Ω)*. In fact the medial axis of a volume Ω is defined as the locus of point equidistant from the boundary $\partial\Omega$ of Ω and, as the sphere is the object whose points are all equidistant from its center, it is straight forward to say that the medial axis is the locus of centers of maximal inscribed spheres (i.e., not strictly contained into any other inscribed spheres) into Ω. MA(Ω) is a non-manifold surface (a surface is said to be 2-manifold if every point has a neighborhood that

can be mapped onto a disk, it is non-manifold otherwise) located medially inside the volume of interest and it can be retrieved once the boundary $\partial\Omega$ of the volume is known. This task is not trivial and it requires the usage of approximation procedures.

It is necessary that the approximation of the medial axis would be as much accurate as possible and fast to be computed. As input data we have a piece-wise surface (i.e., the vessel surface obtained after the segmentation technique) whose vertexes sample the real surface with a high density. A method to compute robustly the medial axis is based on considering only the surface mesh vertexes as a cloud of not-connected points. We introduce, therefore, the definition of Voronoi diagram $Vor(P)$ of a point set P, as:

$$Vor(P) = \bigcup_{\mathbf{p}\in P} \partial V(\mathbf{p}) \tag{4.3}$$

where $V(\mathbf{p})$ is the Voronoi region associated with point $\mathbf{p}$, defined as the region of R^3 whose points are closer to $\mathbf{p}$ than any other points included in P.

$$V(\mathbf{p}) = \{\mathbf{x} \in R^3 \mid dist(\mathbf{p}, \mathbf{x}) \leqslant dist(\mathbf{p}, P)\} \tag{4.4}$$

The union of the boundary of the Voronoi regions as defined in 4.3 constitutes a tassellation of the entire R^3, this union performed for all the points in P is the so called Voronoi diagram, see definition 4.3 and figure 4.1.

Points on $Vor(P)$ have more than one nearest point in P and the $Vor(P)$ diagram lies on the edges of the distance transform - i.e., DT - defined in 4.2, of the point set P, this highlight the connection between Voronoi diagram and the medial axis, being the Voronoi diagram a sort of finite approximation of the medial axis.

To compute the Voronoi diagram, the method described in this work as previously developed by Antiga et al. (2003), propose the usage of its dual - i.e., the Delaunay tessellation of P $Del(P)$ - which in fact is a tetrahedrization of the point set P with the property that no point in P is strictly contains in the sphere circumscribed to each tetrahedron. The relationship that exists between Delaunay tessellation and the Voronoi diagram is that the Voronoi vertices are the circumcenters of Delaunay tetrahedrons, and the sphere circumscribed to the Delaunay tetrahedrons are maximal spheres with respect to the point set P, these spheres are called Voronoi spheres. Moreover, if two Delaunay tetrahedrons share a face their circumcenters can be connected to form an edge of the Voronoi diagram and a Voronoi polygon can be obtained connecting circumcenters of Delaunay tessellation if they all share an edge. There exists more than one method to build the tessellation of Delaunay, three are the major method used: flipping, incremental and random incremental algorithm.

It is worth noting that the Delaunay tessellation does produce always a set of convex tetrahe-
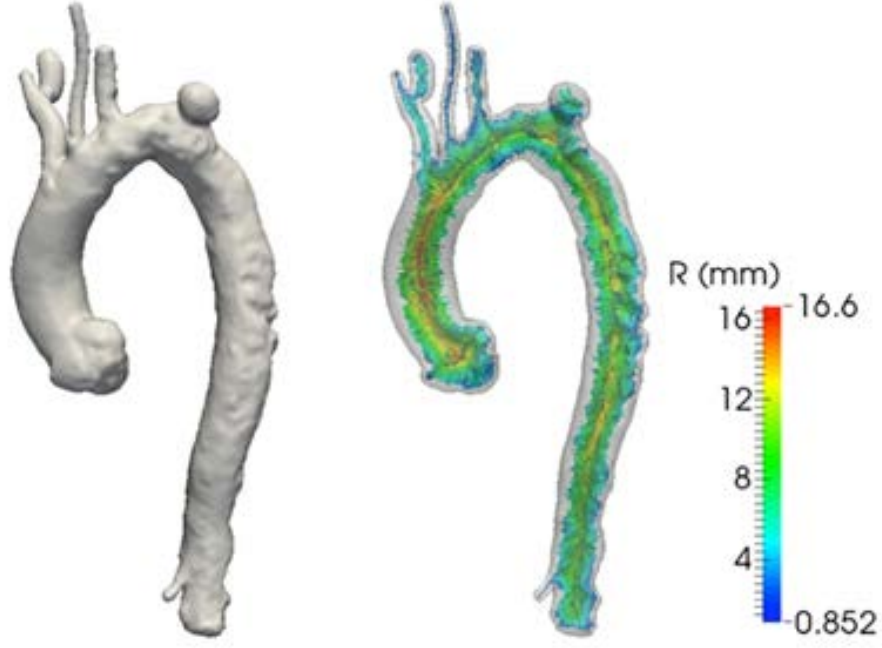
Figure 4.1: Left: thoracic aorta model surface. Right: embedded Voronoi diagram (colored surface) and internal Delaunay tetrahedra boundary (transparent surface). Colors map R, which is the radius of Voronoi spheres.

dral, therefore computing the Delaunay tessellation of a non-convex object, as vessels can be, will not assure to tetrahedralize only the inner part of the object.

The Voronoi diagram is, therefore, not defined only inside the volume under investigation but in the entire 3D space; this leads to the necessity of distinguish between internal and external Voronoi diagram.

This task is tackled removing from the Delaunay tessellation all the tetrahedral falling outside the vessel with their circumcenter and constructing then only those Voronoi polygons whose vertex loop are complete. Form a practical point of view to remove the outer tetrahedral it is useful to compute the normal at the vessel's surface vertex and then to orient it outward. The tetrahedron T_i will be removed if its circumcenter is laying outside Ω:

$$(\mathbf{p_j} - c_j) \cdot \mathbf{n_j} \geqslant 0 \quad \forall p_j \in T_i, \quad j = 1, 2, 3, 4$$

where c_j are the circumcenter of T_i and $\mathbf{n_j}$ are the outward surface normals defined on the vertexes p_j of the tetrahedron.

Now we deal with the internal Voronoi diagram that is a non-manifold surface composed by convex polygons whose vertexes are the circumcenters of the Delaunay tetrahedra and the centers

of the maximal inscribed spheres. The maximal inscribed sphere radius , called $R(\mathbf{x})$ is associated with each vertex and provide information concerning the distance from the boundary. At this point the centerline is defined as the minimum path between two or more points that maximize the distance from the boundary of the surface investigated and is therefore obtained solving equation 4.1 where the cost function $F(\mathbf{x})$ is defined as:

$$F(\mathbf{x}) = \frac{1}{R(\mathbf{x})} \quad \forall \mathbf{x} \in Vor(P) \tag{4.5}$$

where the domain for the search of the centerline has been restricted to $Vor(P)$ instead of the entire R^3. This choice of F assures that the centerline will be medial, since it lies on top of the Voronoi diagram, moreover it minimizes the line integral, since this cost function is the inverse of the maximal inscribed sphere radius.

The minimization problem is equivalent to solve the Euler-Lagrange equation

$$\frac{dC}{dt} = -\nabla F(\mathbf{x}) \tag{4.6}$$

the gradient of the scalar function F will attract the line to the center of the vessel. In this work we decide to use a weighted geodesic approach as implemented in *vmtk*. The minimization of the energy along a path can be seen also as the minimal path between two extreme points on the Voronoi diagram in accord with the scalar function $F(\mathbf{x})$. The weighted geodesic approach, once the scalar field is defined on the domain, considers to search for the shortest path between points p_0 and p_1, the integral of the scalar field along the path should be minimal. A way to solve the problem is to search the weight geodesic distance from p_0 to all the other points in the domain and than to backtrace the path from p_1 to p_0 along the gradient of the weighted geodesic distance field. The weight geodesic distance is defined as:

$$T(\mathbf{x}) = \min_{C \in \Gamma(p_0, x)} \int_0^S F(C(s)) ds \tag{4.7}$$

the term $\Gamma(p_0, \mathbf{x}))$ denotes the set of possible path from p_0 to $\mathbf{x}$ that can be constructed on the Voronoi diagram. To simplify this equation we can do some considerations, $T(\mathbf{x})$ is the weighted geodesic set of distance from p_0, the level sets of $T(\mathbf{x})$ are the regions of equal weighted geodesic distance to p_0, and the weighted geodesic paths are orthogonal to the level sets $T(\mathbf{x})$. Comes together that to make $T(\mathbf{x})$ varies of dT along the distance we need to compute $\frac{dT}{F}$, so that $T(\mathbf{x})$ must satisfy the following equation over the domain of the Voronoi diagram

$$|\nabla T(\mathbf{x})| = F(\mathbf{x}) \tag{4.8}$$

this equation is non linear and hyperbolic, it is known as the Eikonal equation, and it is

much more convenient than the variational formulation above. Once the field of weighted geodesic distances is found, the path of interest is calculated following from p_1 the gradient of $\nabla T(\mathbf{x})$ in every point, solving this equation

$$\frac{dC(s)}{ds} = -\nabla T(\mathbf{x}) \tag{4.9}$$

thus obtaining $C(s)$ that minimizes the energy function related to the centreline, s is the arch length parametrization with $C(L) = p_1$ and $C(0) = p_0$. This procedure ensures that centerline lies on the ridges of the distance transform (DT) and that its path from p_0 to p_1 is minimal, see figure 4.2.
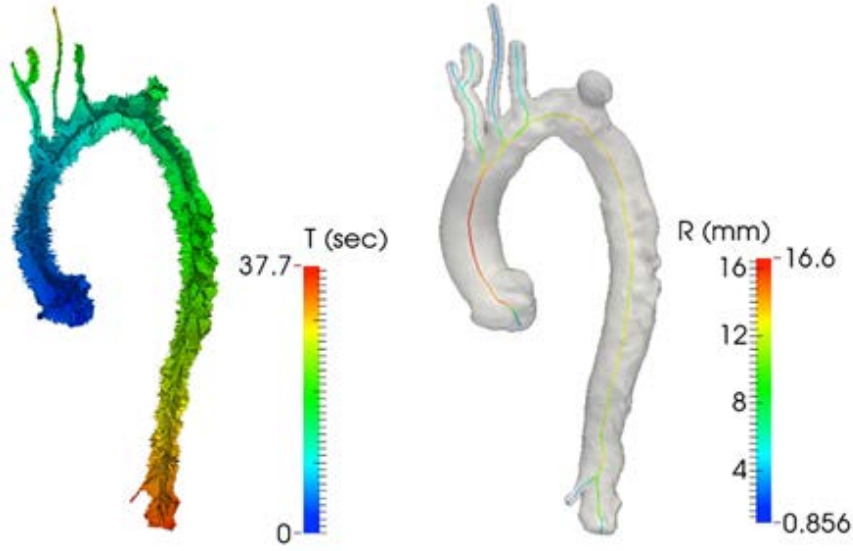
Figure 4.2: Left: solution of the Eikonal equation over the embedded Voronoi diagram for the thoracic aorta model presented in figure 4.1, with seed point at the aorta inlet. Right: centerlines obtained after backtracing from model outlets (namely brachiocephalic arteries, left common carotid artery, left subclavian artery, aorta outlet, and celiac artery.). Colors on centerlines are the values of maximal inscribed sphere radius.

4.2.2 Centerline post-processing

Voronoi diagrams and medial axis in general are very sensitive to boundary noise, in our case to the vessel surface. It can happen that if the surface shows local irregularities or bulges the medial axis moves considerably attracted by the surface irregularities. It follows that even a small change in single point position can affect Voronoi diagram and therefore medial axis computation. Moreover, it is essential, in order to perform a robust and repeatable geometric analysis, to deal with smooth centerline deprived of noise and sudden changes in direction, since being centerline

only C0 continuous, we will use the method of finite differences to perform centerline differentiation.

Given the drawbacks of the centerline calculation we would, before any further analysis, re-sample and smooth the centerline. In order to perform the re-sampling step we apply a spline filter, in particular we use an interpolating cubic B-spline with a sample size of a hundred points. We exploit the *VTK* abstract class *vtkSpline* which gives the advantage to deal with a piece-wise polynomial function builds on equally spaced points. To obtain a smoothed representation of the centerline we moreover apply a Laplacian smoothing filter. The Laplacian smoothing filter (Field, 1988) is an algorithm used to smooth a polygonal mesh or in our case a piece-wise line. For each point belonging to the centerline a new position is chosen based on local information (the position of neighbours) and the point is moved to the new position. The operation is carried on iteratively through all the points. More formally:

$$\Delta x_i = \tau w_{ij} \sum_{j \in N_1(i)} (x_j - x_i) \tag{4.10}$$

where x_i is the i-th point belonging to the centerline, $N_1(i)$ are its first order neighbours and $w_{ij} = \frac{1}{m}$ where m is the number of neighbours, in the case of centerlines $m = 2$, and τ is a relaxation factor ranging between 0 and 1, choosing 0 we decide not to *relax* the position of the current point but simply to keep the same position, choosing 1 we decide to commit the new position of the current point to the calculation of the barycentre of its neighbour points. We decided to use a value of relaxation equal to 0.4.

4.2.3 Bifurcation reference system definition

In the previous section, we deal with the challenging task of centerline computation. Even though high importance has been given to this key step, no information about related geometric characterization has been extracted yet. It is of high importance to the subsequent geometrical analysis to be able to identify bifurcation regions and to be able to branch the aorta in three regions of interest: the ascending aorta, the thoracic aorta and the descending aorta. In order to perform this debranching operation we need to be able to identify in a robust and repeatable manner the bifurcation regions related to the supra-aortic branches and to the celiac artery. The method has to deal with a large population of subjects which have different anatomical features; it is therefore of paramount importance to be objective in the identification of the regions of interest through different patient-specific cases.

In this section we illustrate how it is possible to identify bifurcation and related branches exploiting the definition of centereline and tube as implemented in a previous work of Antiga et al. (2004). They present a fully automated method for decomposing the surface of bifurcating vessels. Their goal is to provide a technique based on objective criteria capable of generating

consistent parameterizations over a wide range of bifurcating geometries, so as to allow unbiased quantitative comparisons of geometric quantities in the context of population studies.

Since, as stated in previous section, centerlines host the centers of maximum inscribed spheres, it is possible to build a tube-like structures based on the intersection of the spheres themselves, see figure 4.3.
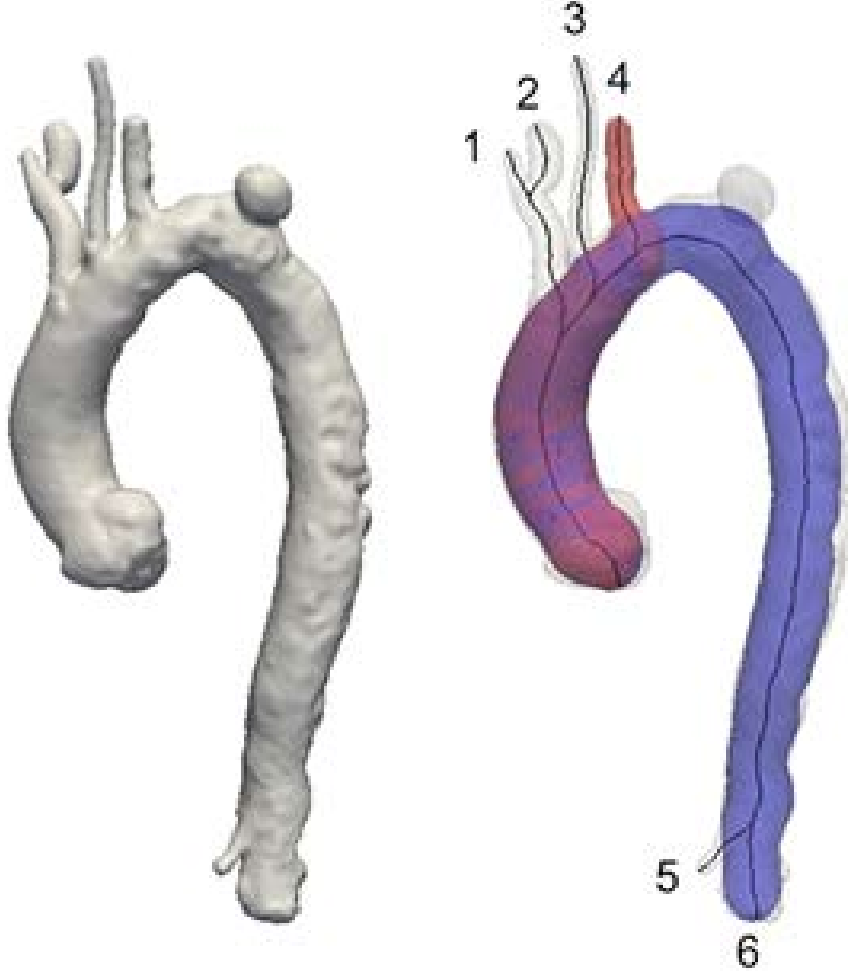
Figure 4.3: Left: realistic surface model of the thoracic aorta. Right: Representation of the six centerlines respectively belonging to the brachiocephalic arteries (1 and 2), left common carotid artery (3), left subclavian artery (4), celiac artery (5), and descending aorta (6). In blue and red are depicted the zero level sets of the tubes generated by the centerlines 4 and 6.

Let describe formally what a tube is, it is a function $T : R^3 \to R$:

$$T_{c,s}(\mathbf{x}) = min_{s \in [0,L]}\{|\mathbf{x} - c(s)|^2 - r^2(s)\} \tag{4.11}$$

where $c(s)$ is a centerline, parameterized by arclength $s \in [0, L]$, $\mathbf{x}$ is the point coordinates,

and $r^2(s)$ is the radius of the sphere with center on the centerline. The zero level of $T_{c,s}(\mathbf{x})$ is the tube surface, see figure 4.3 for tubes of centerline referring respectively to left subclavian artery and descending aorta. Computing centerline from the surface of a branching vessel results in the computation of a multiplicity of curves running from one inlet to multiple outlets of the bifurcations, figure 4.3. The centerlines calculated will not divide sharply after bifurcation but they rather depart smoothly from each other. In fact the centerline calculation does not provide any geometrical information about the bifurcation region or reference system and therefore a method to identify the bifurcation reference system is needed. This is not an easy task and it has to accomplish some basic and necessary requirements: robustness, repeatability, flexibility, and user-independence. The most important feature of the methodology is assuring that small changes in anatomical shape does not produce non-consistent results.

The definition of the bifurcation reference system recall from Antiga et al. (2004) deals with the identification of two reference points along each centerline. The first reference point is defined where a centerline intersects the tube defined on the other centerline downstream the bifurcation region.

More formally, given the two centerlines calculated between the same inlet and the two different bifurcation outlets $c_1(s)$ and $c_2(s)$, the point c_1^A at which the line $c_1(s)$ crosses the tube surface of $ts_2(s)$, see figure 4.4, is determined by

$$s_1^A = min\{s_1 \in [0, L_1] : \exists s_2 \in [0, L_2] |c_1(s_1) - ts_2(s_s)|^2 = 0\} \tag{4.12}$$

where s is the arclength of the two centerlines. The second reference point c_1^B, with $s_1^B < s_1^A$, see figure 4.4, is defined as the center of the upstream sphere touching the first reference point c_1^A

$$s_1^B = max\{s_1 \in [0, s_1^A] : |ts_1(s_1) - c_1^A|^2 = 0\} \tag{4.13}$$

These four points delimit a segment on each centerline and this segments identify the bifurcation region carrying information about shape and size of the region itself. Fixed the four points it is possible to define the origin of the bifurcation reference system, see figure 4.4 red dot, as the barycenter of the surfaces of the maximal inscribed spheres centered in the reference points

$$\mathbf{x}_O = \frac{\sum_{i,j}(r_i^j)^2 c_i^j}{\sum_{i,j}(r_i^j)^2} \qquad i = 1, 2 \qquad j = A, B \tag{4.14}$$

where r_i^j are the radii of the maximal inscribed spheres associated with the centerline locations c_i^j. This definition of the origin for the bifurcation reference system accounts for the potential differences in branch size, in fact defining the bifurcation origin as in 4.14, that is weighting the position of the reference points c_i^j with the radius of their relative maximal inscribed spheres,

penalizes the position of the reference points on the smaller branches, thus stabilizing the position of the origin with respect to the changes in the relative size of the branches.
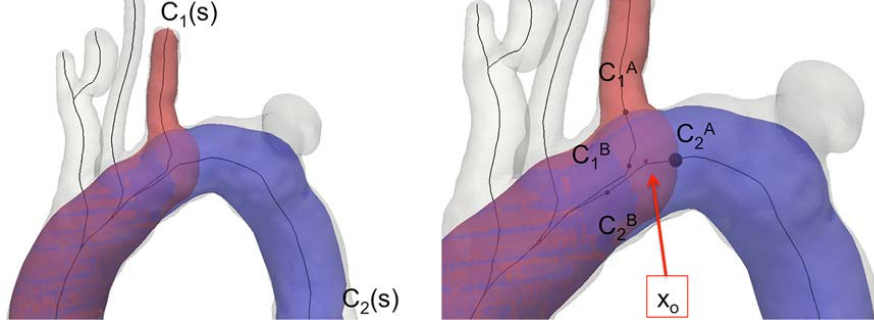
Figure 4.4: Left: in blue and red are depicted the zero level sets of the tubes generated by the centerlines 4 and 6. Right: reference points (in black) and center of the bifurcation (in red).

It is worth noting that this origin does not correspond to the location where centerlines depart from each other, instead it is more robustly determined from the centers and the radii of the spheres inscribed at the reference points previous calculated.

The bifurcation plane is then defined by the normal $\mathbf{n}_{bif}$ to the polygon defined by the four reference points evaluated in $\mathbf{x}_O$. Since the four points would be non-planer the normal $\mathbf{n}_{bif}$ will be the bilinear interpolation in the bifurcation origin of the normals at each vertex of the polygon as the normal of the corner triangles of the polygon itself. The bifurcation reference frame is completed by calculating a downstream direction $\mathbf{u}_{bif}$ as the normalized average of vectors $(c_1^A - c_1^B)$ and $(c_2^A - c_2^B)$. By defining the origin of the bifurcation reference system as with 4.14 it is possible to detect a shift of the origin toward the center of the main vessel in term of size and the bifurcation normal will be less influenced by the reference point related to small branches.

4.2.4   Branch extraction procedure

The identification of the bifurcation regions allows the decomposition of the centerline into tracts belonging to different branches upstream and downstream the bifurcation region in addiction to the bifurcation region itself. Once centerline has been split into its relative branches, the reference points are exploited to decompose the surface of the vessel. Centerlines are split into tracts belonging to different bifurcation branches and surface decomposition is performed by dividing the space around the tube surfaces of each centerline tract, see figure 4.5.

Each centerline $c_i(s)$ is grouped into tracts defined by the reference points $s \in [0, s_i^B]$ and $s \in [s_i^A, L_i]$; a gap is left between the reference points at the bifurcation region. Each centerline tract i is then associated with the related branch and a group function $\gamma_i(s)$ is then defined for each tract i composing the group. To carry out the decomposition of a vessel's surface into its related
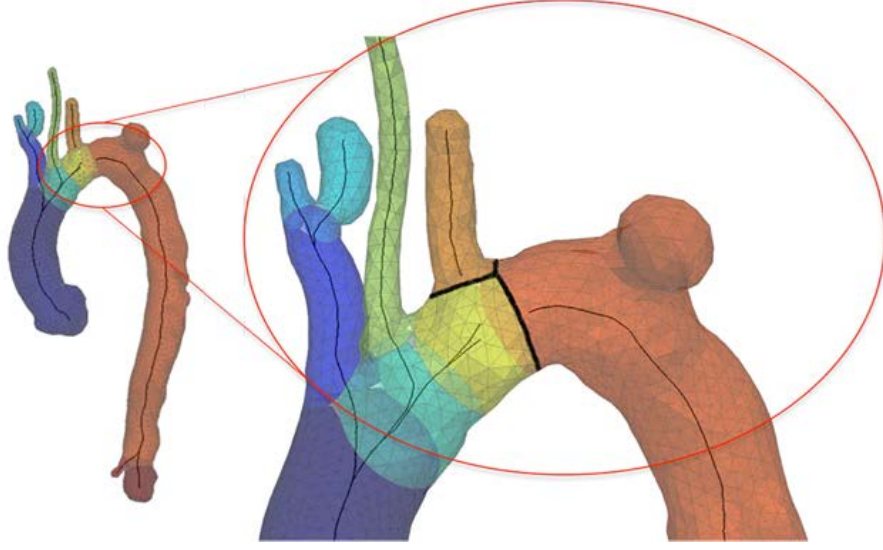
Figure 4.5: Left: surface mesh with highlighted with different colors the region belonging to different branches. Detail (in red circles) depicts the bifurcation region where centerlines are split into trecat belonging to different branches and the bifurcation region is defined (solid black line) accounting for the vessels size, in fact the line of the splitting region is closer to the smaller branches.

branches we can exploit the distance metrics defined in 4.11, in fact it is possible to decompose R^3 into groups, in which the $i-th$ group is composed by the union of points closer to $\gamma_i(s)$ than to any other $\gamma_j(s)$, more formally

$$\Gamma_i = \{\mathbf{x} \in R^3 : |\mathbf{x} - \gamma_i(s_i)|^2 \leqslant |\mathbf{x} - \gamma_j(s_j)|^2, \qquad \forall j \neq i\} \tag{4.15}$$

Dealing with this definition means that Γ_i is a region of the space R^3 where branches are influenced only by the centerline branch related to the $i-th$ group. The partition of the vessel is therefore carried out using 4.15, and the boundaries of each region are identified as the region where

$$\partial\Gamma_i = \bigcup_{j \neq i}\{\mathbf{x} \in \Gamma_i : |\mathbf{x} - \gamma_i(s_i)|^2 = |\mathbf{x} - \gamma_j(s_j)|^2\} \tag{4.16}$$

Since no definition of bifurcation region on the vessel's surface is present, the boundaries meet at the bifurcation region. As the definition of tube function 4.11, we can definitely say that the splitting boundary accounts for relative size of the vessels departing from the bifurcation region. It is possible to verify that splitting lines are positioned around the insertion of the branches and account for their size, in fact the boundary of the branches is closer to the smaller one in size. Once the vascular tree is split into its related branches we can proceed with further geometrical analysis on different vascular anatomy since fixed reference regions - i.e., bifurcations - can robustly

be identified and used in order to perform same measures at same/comparable aortic regions on different population group.

4.2.5   Bifurcation reference system transformation

Registration of shapes is an important problem arising in many research areas, such as computer graphics, vision, pattern recognition, and structural biology. In general, given two structures represented as surfaces, one wishes to identify for every point of one surface the corresponding point of the other. Dealing with 4-dimensional data-sets of pre- and post-TEVAR (Thoracic EndoVascular Aortic Repair), it is quite immediate that a comparison between 3D reconstructed models can be of paramount importance to assess good outcomes and to understand the changes induced by the metallic stent-graft on both shape of the vessel and changes experienced by the thoracic aorta during the cardiac cycle.

In order to possibly compare the 3D models of pre- and post-TEVAR we pointed out that a rigid-body transformation - i.e., mutual distances of points within a model are conserved during transformation - between the models under investigation would be a necessity.

A rigid body transformation can be decomposed in a rotation matrix R_{AB} and a translation vector T_{AB} .

The transformation is written as

$$\mathbf{x_A^{transf}} = R_{AB}(\mathbf{x_A}) + \mathbf{T_{AB}} \tag{4.17}$$

We decide to implement a simple but robust rigid body transformation and transform not a set of point but two reference systems integral with the surfaces under investigation. Bifurcation reference system (BRS) described in previous section 4.2.3 tends to be more stable than individual reference points along the centerline and also more stable than any other point on the surfaces to be registered. We therefore decide to exploit the BRS of pre- and post-TEVAR configuration and to perform an alignment of the pre-TEVAR BSR into the post-TEVAR BSR, see figure 4.7.

Since the thoracic aorta hosts lots of bifurcation regions and the same amount of BRS, almost five, we need to define which of these regions is the most suitable for our purpose. We know from previous section 4.2.4 that the splitting boundary accounts for relative size of the vessels departing from the bifurcation region. It is therefore reasonable exploiting a BRS that has the better chance of being stable ; this BRS is identified as the most distal along the brachiocephalic artery, where the vessel entering the bifurcation region and the vessels leaving the bifurcation region has approximately the same size, see figure 4.7.

At this point we compute the distance between the origin of the BSRs as

$$\mathbf{T_{PrePost}} = X[i]_{pre} - X[i]_{post} \tag{4.18}$$

where $X[i]_{pre}$ and $X[i]_{post}$ are the coordinates of the origin respectively of the BRS pre-TEVAR and of the BRS post-TEVAR.

The rotation matrix, named $R_{PrePost}$, is constructed from the rotation angles, we exploit the Euler angles that are three angles used to describe the orientation of a rigid body in 3-dimensional Euclidean space. To describe such an orientation three parameters are required and are typically denoted as α, β, and γ. These angles represent a sequence of three elemental rotations, i.e., rotations about the axes of a coordinate system. Any orientation can be achieved by composing three elemental rotations. The elemental rotations can either occur about the axes of the fixed coordinate system (extrinsic rotations) or about the axes of a rotating coordinate system, which is initially aligned with the fixed one, and modifies its orientation after each elemental rotation (intrinsic rotations).

In the following, the axes of the BRS pre-TEVAR are denoted as $\{Normal^{pre}, Cross^{pre}, UpNormal^{pre}\}$ and the axes of the rotated frame are denoted as $\{Normal^{transf}, Cross^{transf}, UpNormal^{transf}\}$, these will be transformed to coincide with the axes of the BRS post-TEVAR $\{Normal^{post}, Cross^{post}, UpNormal^{post}\}$.

The geometrical definition (referred sometimes as static) of the the angles exploited in this work is based on the axes of the above-mentioned (pre and post) reference frames and an additional axis called the line of nodes. The line of nodes (N) is defined as the intersection of the $\{Normal^{pre}, Cross^{pre}\}$ and the $\{Normal^{post}, Cross^{post}\}$ coordinate planes. In other words, it is a line passing through the common origin of both frames, and perpendicular to the $\{UpNormal^{pre}, UpNormal^{post}\}$ plane, on which both $UpNormal^{pre}$ and $UpNormal^{post}$ lie. The three angles are defined as follows:

- α is the angle between the $Normal^{pre}$ axis and the N axis;

- β is the angle between the $UpNormal^{pre}$ axis and the $UpNormal^{post}$ axis;

- γ is the angle between the N axis and the $Normal^{post}$ axis.

This definition implies that:

- α represents a rotation around the $UpNormal^{pre}$ axis;

- β represents a rotation around the N axis;

- γ represents a rotation around the $UpNormal^{post}$ axis.

To better comprehend the process please refer to figure 4.6.

In this work angles are automatically computed between pre- and post-TEVAR configuration yielding the rotation matrix
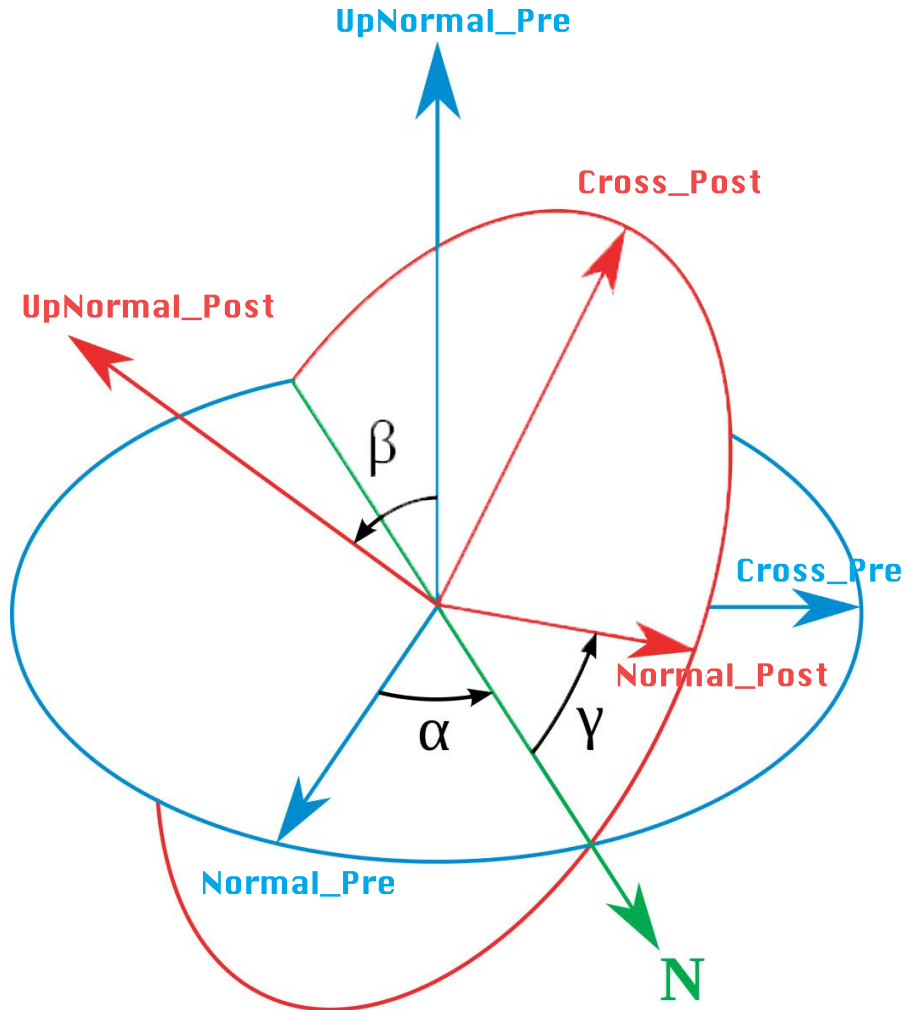
Figure 4.6: Euler angles representing rotations about $UpNormal^{pre}$, N, and $UpNormal^{post}$ axes. The $Normal^{pre}, Cross^{pre}, UpNormal^{pre}$ (original) system is shown in blue, the $Normal^{transf}, Cross^{transf}, UpNormal^{transf}$ (rotated) system is shown in red. The line of nodes (N) is shown in green.

$$R_{PrePost} = R_{UpNormal^{pre}}(\alpha) \, R_N(\beta) \, R_{UpNormal^{post}}(\gamma) \qquad (4.19)$$

described in detail as:

$$R_{UpNormal^{pre}}(\alpha) = \begin{pmatrix} \cos(\alpha) & -\sin(\alpha) & 0 \\ \sin(\alpha) & \cos(\alpha) & 0 \\ 0 & 0 & 1 \end{pmatrix}$$

$$R_N(\beta) = \begin{pmatrix} 1 & 0 & 0 \\ 0 & \cos(\beta) & -\sin(\beta) \\ 0 & \sin(\beta) & \cos(\beta) \end{pmatrix}$$

$$R_{UpNormal^{post}}(\gamma) = \begin{pmatrix} \cos(\gamma) & -\sin(\gamma) & 0 \\ \sin(\gamma) & \cos(\gamma) & 0 \\ 0 & 0 & 1 \end{pmatrix}$$

Rotation matrix and translation vector gives the transformation as follows:

$$\mathbf{x}_{\mathbf{Pre}}^{\mathbf{transf}} = R_{PrePost}(\mathbf{x}_{\mathbf{Pre}}) + \mathbf{T}_{\mathbf{PrePost}} \qquad (4.20)$$

This rigid body transformation is applied to all $\mathbf{x_{Pre}}$ of the pre-TEVAR configurations resulting in the rigid alignment of the two aortic models of interest, see figure 4.7.

4.2.6 Surface longitudinal subdivision: outer contour lines

Several works in literature dealt with the parametrization of surfaces starting from their picewise linear approximation - i.e., surface mesh. In this section we describe how to exploit angular parametrization of vessel's surface to perform a surface data analysis through the definition of *outer contour lines*, see figure 4.8. Performing such an analysis required the usage of a method described in Antiga et al. (2004). First of all, once we split the branches of a vascular network we can say we are dealing with cylinders, since topologically speaking those regions resemble a cylinder. Given a surface $\partial\Gamma_i$, already defined in the previous section, of a branch i with extremities given by two topological circle ψ_{i0} and $\psi i1$, we search for a bijective mapping

$$\Phi : \partial\Gamma_{i_{\mathbf{x}}} \to \mathcal{U}_{\mathbf{u}} \qquad (4.21)$$

$\mathcal{U} \subset R^2$ is the parametric space in the coordinates $\mathbf{u} = (u, v)$, where $u \in [0, L_i]$ is the longitudinal parametric coordinate and $v \in [-\pi, \pi]$ is the periodic circumferential parametric coordinate such that $\Phi(\mathbf{x}) = (0, v)$ on ψ_{i0} and $\Phi(\mathbf{x}) = (L_i, v)$ on ψ_{i1}.
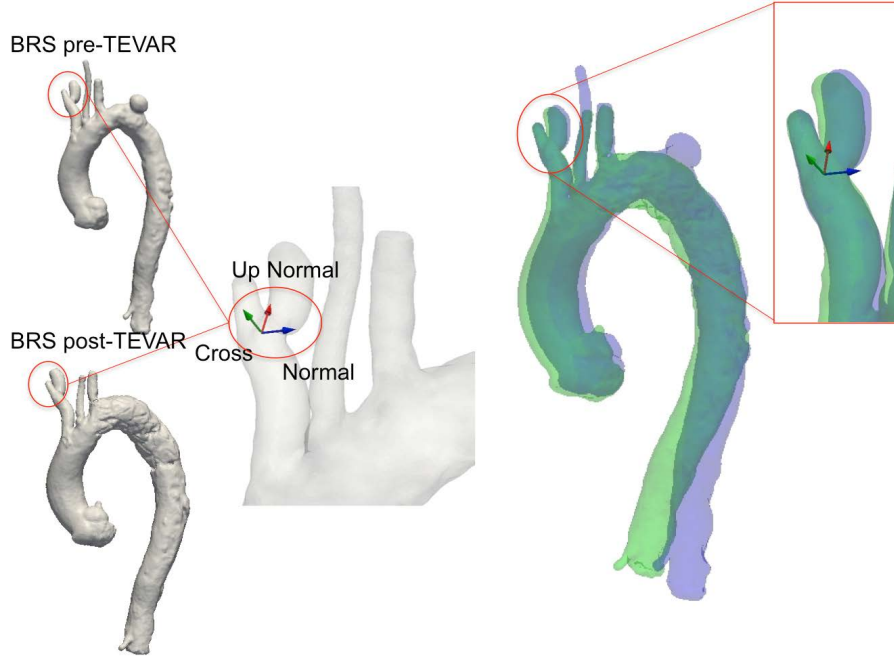
Figure 4.7: Bifurcation reference system definition on both pre- and post-TEVAR models. Registration (left side) of the pre- and post-TEVAR surfaces depicted respectively in blue and green colors.

Longitudinal mapping: The approach described in Antiga et al. (2004) to build a longitudinal mapping is that of computing a harmonic function with extremes on the branch boundaries, as proposed in Halier et al. (2000), and then to stretch it in order to gather localization with respect to centerline abscissa and reference system. The computation of the harmonic function $f = f(\mathbf{x}), \mathbf{x} \in \partial \Gamma_i$, is performed by solving the partial differential equation:

$$\Delta_B f = 0 \tag{4.22}$$

with boundary condition $f(\mathbf{x}) = 0$ on ψ_{i0} and $f(\mathbf{x}) = 1$ on ψ_{i1}, and where Δ_B is the Laplace-Beltrami operator. The Laplace-Beltrami operator can be generalized to operate on functions defined on surfaces in Euclidean space and, more generally, on Riemannian and pseudo-Riemannian manifolds; is defined as the divergence of the gradient, and is a linear operator taking functions into functions. Solving 4.22 corresponds to minimizing the Dirichlet functional

$$E(f) = \frac{1}{2} \int_{\partial \Gamma_i} |\nabla f|^2 ds \tag{4.23}$$

Equation 4.22 is solved using a finite elements approach on the surface mesh, as described in detail in Angenent et al. (1999).

Circumferential mapping: Different from the approach proposed in Halier et al. (2000), in the

work of Antiga et al. (2004), they define v as the angular position of surface points around the centerline. The position of a point with respect to a curve in space is determined by a set of normals $n(s)$ along the curve. This normals definition has been studied and developed in many works and with the usage of different approaches. In general we can say that given a curve $c(s) \in R^3$, a reference frame can be identified by a tangent unit vector

$$t(s) = \frac{c'(s)}{|c'(s)|} \tag{4.24}$$

and by two other unit vectors, normal $n(s)$ and bi-normal $b(s)$, both lying on a plane normal to $t(s)$ and responding to the following assumption $n(s) = t(s) \times b(s)$. A popular solution to this problem is given by the Frenet frame (Bishop, 1975) which defined the unit vector $n(s)$ at each point directed toward the center of the osculating circle of the curve. This approach suffers of abrupt changes in direction of $n(s)$ and is therefore not so useful for gather a smooth twisting behavior. Twist minimization can be achieved, instead, with the usage of the parallel transport approach (Hanson and Ma, 1995). The PT (parallel transport) approach simply define the frame at $s+ds$ from the frame at s by rotating $t(s)$ into $t(s+ds)$ in the osculating circle plane. The frame is thus rotated of a minimal quantities and no twist is introduced. In practice a frame defined at c_{i+1} is obtained rotating the frame defined in c_i around the vector $n_i = t_i \times t_{i+1}$ of an angle $\alpha = \arccos(t_i \dot{t}_{i+1})$ and then translating the frame at position c_{i+1}. Whilst for the Frenet frame the definition and the orientation of the frame at s is intrinsic to the curve, for PT approach is required to define the initial frame to be transported. To our purpose the initial frame is located near the bifurcation origin, $c(s_0)$, and is given by $t(s_0)$, the tangent unit vector to the centerline points toward the downstream direction, $n(s_0) = n_b$, the reference system bifurcation normal, and $b(s_0) = t(s_0) \times n(s_0)$. Once the centerline normals are defined, v is build at each point $\mathbf{x} \in \Gamma_i$, the surface under investigation, by finding its nearest point $c(\bar{s})$ on the centerline, by finding the projection $\bar{\mathbf{x}}$ of $\mathbf{x}$ on the plane normal to $t(\bar{s})$ and computing

$$v(\mathbf{x}) = \arccos((\bar{\mathbf{x}} - c(\bar{s}))\dot{n}(\bar{s})) \tag{4.25}$$

.

We decide to exploit the *circumferential mapping* and act as follows for ascending and descending thoracic aortic branches. *Circumferential mapping* associates at each point of a surface its angular position value around the centerline, i.e., $[-\pi, \pi]$.

We therefore compute ten equidistant values in space between $[-\pi, \pi]$ and automatically select the points of the surface which lay exactly at the same angular position. These groups of points have been identified and for each group the points have been ordered exploiting the longitudinal mapping previously described and computed. In this way we obtain ten equidistant outer contours
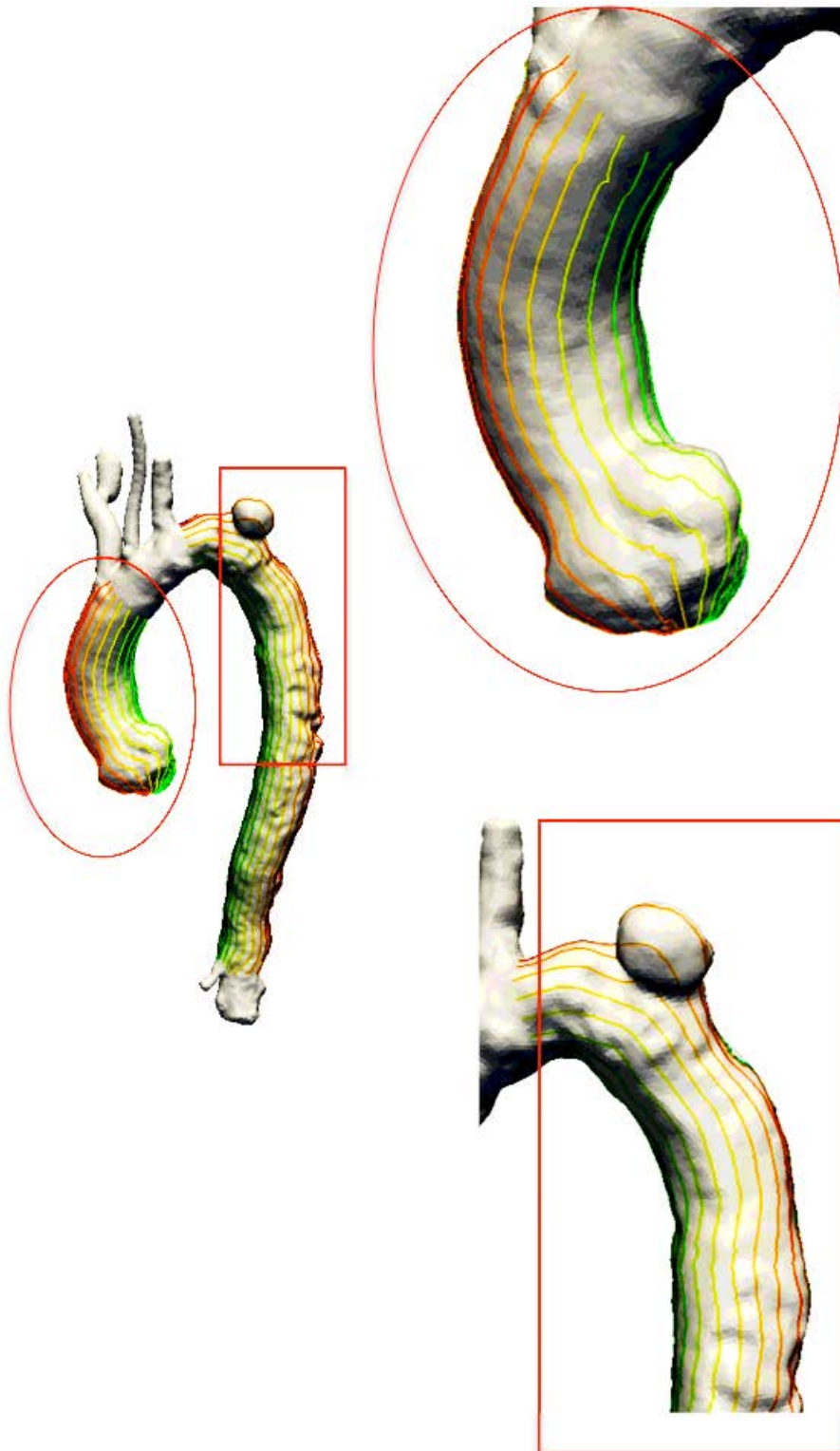
Figure 4.8: Example of outer contour lines are depicted in figure for the ascending and descending aorta.

laying on the surface of the vessel.

Given $I = [-\pi, -\frac{4}{5}\pi, -\frac{3}{5}\pi, -\frac{2}{5}\pi, -\frac{1}{5}\pi, 0, \frac{1}{5}\pi, \frac{2}{5}\pi, \frac{3}{5}\pi, \frac{4}{5}\pi, \pi]$ for each outer contour we define the outer length OL as:

$$OL(\theta) = \int_{P_0(\theta)}^{P_1(\theta)} s \, ds \qquad \theta \in I \tag{4.26}$$

where s is the curvilinear abscissa defined on the centerline and P_0 is the initial point where the longitudinal parametric map has value zero and P_1 is the final point where the longitudinal parametric map has value one.

Moreover we introduce a relative quantity to track the changes in space experienced by the aorta, named Outer Length Changes (OLC), expressed in percentage and defined as follows:

$$OLC = \frac{Amplitude(OL(\theta))}{A_{v_{space}}(OL(\theta))} \tag{4.27}$$

where:

$$Amplitude(OL(\theta)) = (\max_{\theta \in I}(OL(\theta)) - \min_{\theta \in I}(OL(\theta))) \tag{4.28}$$

$$A_{v_{space}}(OL(\theta)) = \frac{1}{10} \sum_{\theta \in I} OL(\theta) \tag{4.29}$$

4.2.7 Surface sectioning

In our analysis of the thoracic aorta we deal with six centerlines (see Fig. 4.14, centre). Once the centerlines are computed our tool allows to cut the vessel's surface with section perpendicular to the centerline itself and to compute the area of every section.

We exploit this feature to automatically select the sino-tubular junction (section A in figure 4.9): first the aortic root is cut from the valvular plane upward with 30 sections equally spaced of 1 mm. The area of each section and its difference with the subsequent section is calculated, returning the sino-tubular junction as the section where this difference reaches a local minima.

Centerline also allows the definition of vessel bifurcations. In fact each centerline point is associated to the radius of the maximum inscribed sphere defined in that point: this means that we can construct a tube around each centerline build from the envelope of maximum inscribed spheres. In general, each two centerlines in a vascular tree will mutually intersect the surface of the other centerline's tube. This region is defined as a bifurcation region (Piccinelli et al., 2009).

The tool identifies the brachiocefalic section (section B in figure 4.10), one centimetre before the innominate artery bifurcation, as the point where the centerlines referring to the ascending aorta and the innominate artery divide.
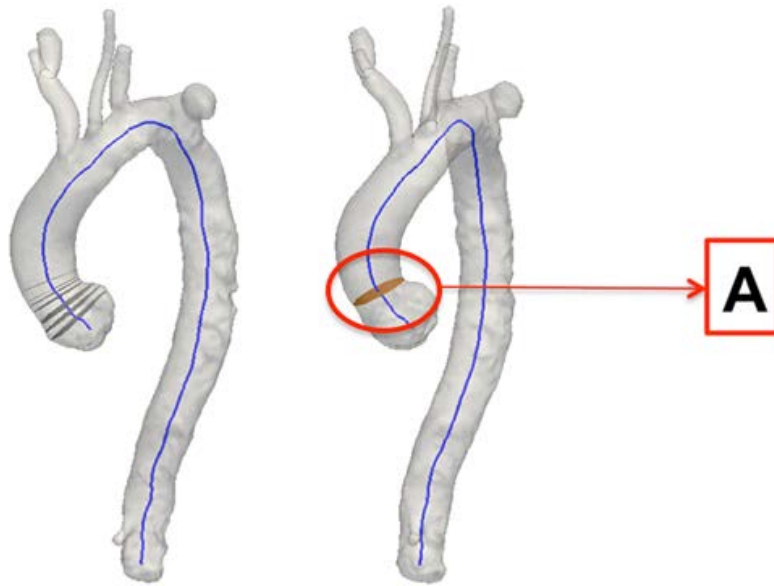
Figure 4.9: Automatic surface sectioning. Section A represents the level of the sino-tubular junction (STJ). On the left side are depicted 30 sections thet cut the proximal aorta from the valvular plane upward (1mm spaced). On the right side local minima of the difference in area between the sections return the STJ section. Section A indicates the begin of the ascending aorta that is comprised between STJ and the innominate artery.
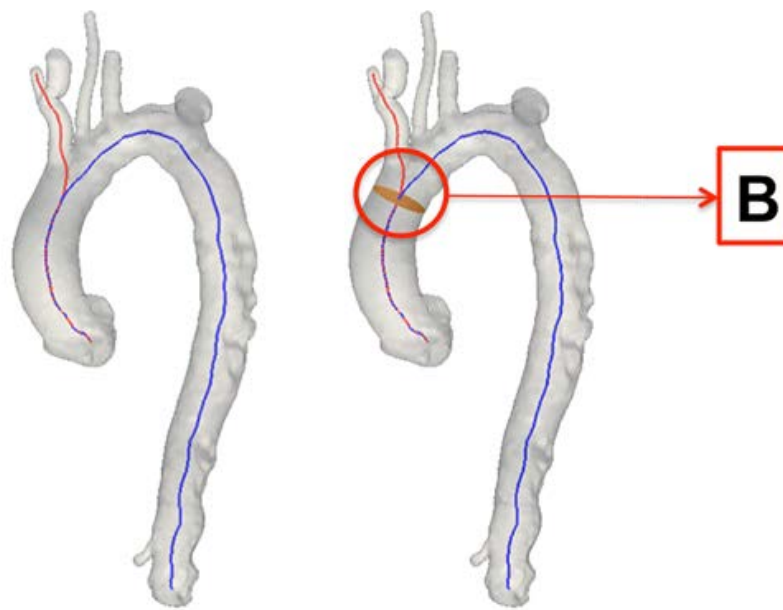
Figure 4.10: Automatic surface sectioning. Section B represents the level of the innominate artery bifurcation, as the point where the centerlines referring to the ascending aorta and the innominate artery divide. Section B indicate at the same time the end of the ascending aorta and the begin of the aortic arch, delimited by section B and C see for reference 4.11.

In a similar manner it identifies the section just after the left subclavian artery (section C in figure 4.11), once this section is automatically identified sections D and E are easily defined at a fixed distance of respectively 10 and 20 cm from section C along the centerline (see figure 4.11).
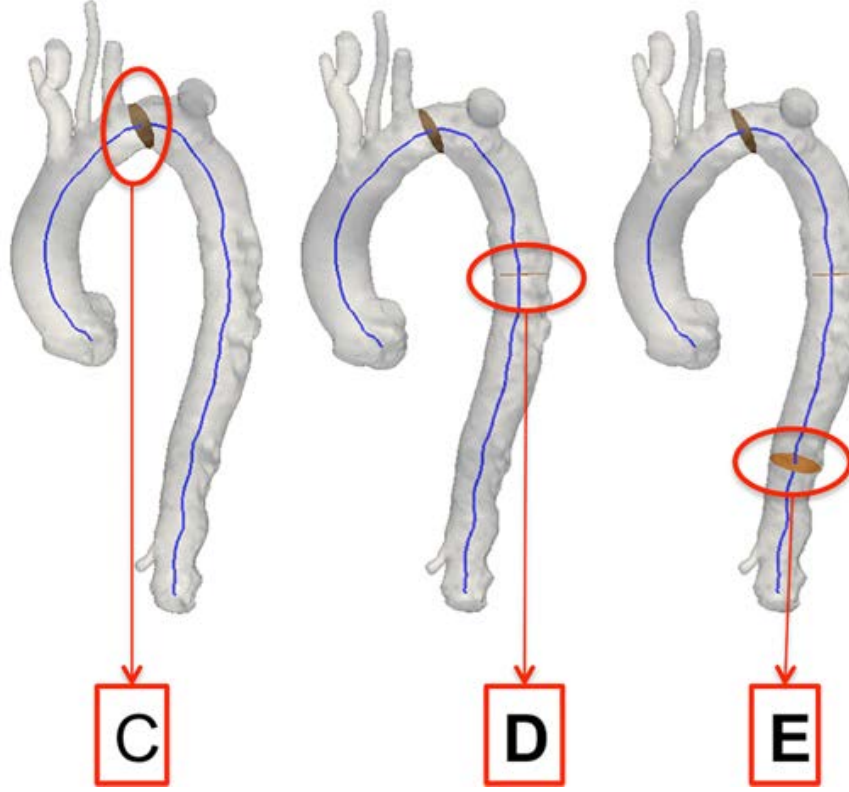
Figure 4.11: Automatic surface sectioning. Section C represents the region just after the left subclavian artery (LSA) and it defines the begin of the descending thoracic aorta. Sections D and E are inspection sections along the descending aorta placed at respectively 10 and 20 cm far away from the LSA.

Finally, the celiac bifurcation (section F in figure 4.12) is identified as the point where the centerlines referring to the descending aorta and the celiac artery divide. Sections and length are depicted globally in figure 4.13.

4.3   Performed measures

4.3.1   Area and diameter

Once all the regions of interest have been identified (sections A, B, C, D, E, and F in figure A.5) the tool can easily calculate: area, minimum and maximum diameter. The area is computed triangulating the section of interest and then summing the area of each triangle over the entire section. Minimum and maximum diameter of every section is calculated as follows:
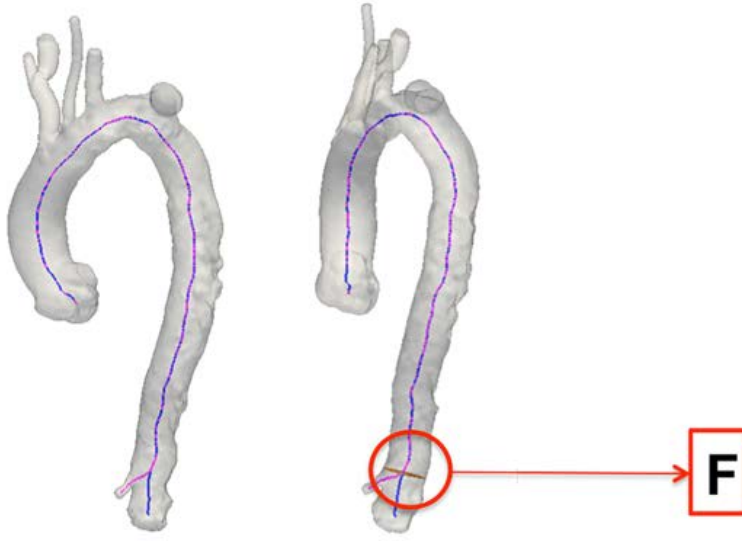
Figure 4.12: Automatic surface sectioning. Section F represents the level of the celiac bifurcation region. In fact at this point departs from the descending aorta the celiac artery the is exploited as anatomical landmark to indicate the end of the thoracic aorta and the begin of the abdominal aorta.

$$d_{min}(S) = \min_{\mathbf{x} \in \partial S} (\max_{\mathbf{y} \in \partial S} (dist(\mathbf{x}, \mathbf{y}))) \tag{4.30}$$

$$d_{max}(S) = \max_{\mathbf{x} \in \partial S} (\max_{\mathbf{y} \in \partial S} (dist(\mathbf{x}, \mathbf{y}))) \tag{4.31}$$

where $\mathbf{x} = (x, y, z)$, $\mathbf{y} = (x, y, z)$ are coordinates of the points of the contour ∂S of the section S, and $dist(\,\cdot\,)$ is the Euclidean distance.

4.3.2 Length

We define, furthermore, the length between two sections as the length of the centerline, see figure 4.13.

We perform this computation exploiting the concept of curvilinear abscissa defining the length between two generic sections S_1 and S_2 as:

$$l(S_1, S_2) = \int_{S_1}^{S_2} s \, ds \tag{4.32}$$

where s is the curvilinear abscissa defined on the centerline and s_1 and s_2 are the points of the centerline on the generic sections S_1 and S_2. Lengths of the four regions of interest are computed and classified as L (total length), $L1$ (ascending aorta length), $L2$ (aortic arch length)
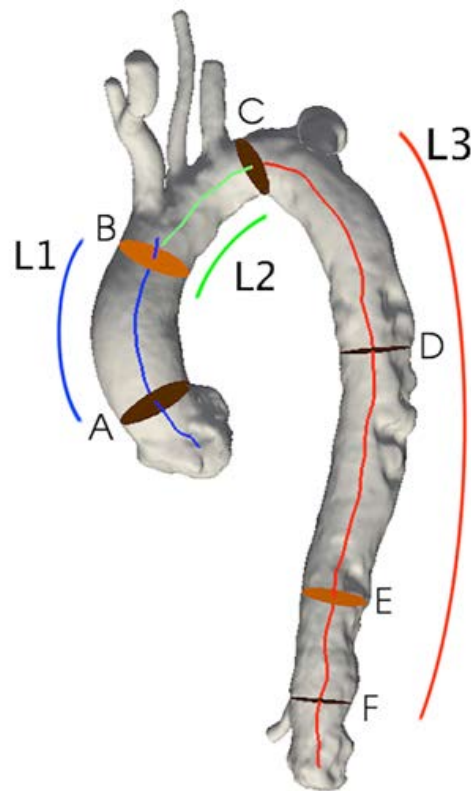
Figure 4.13: Automatic surface sectioning. All the automatically computed sections A, B, C, D, E, and F depicted with the length of interest identified between sections A and B (length L1) the ascending aorta, between sections B and C (length L2) the aortic arch, and between sections C and F (length L3) the descending aorta. Total length L is computed between sections A and F, the entire thoracic aorta.

and $L3$ (descending aorta length) where the length of every segment is the length of the centerline between section A and F, A and B, B and C, C and F respectively (see Fig. 4.14).

4.3.3 Dynamic geometric changes

Being the data-set with which we are dealing, a 4-dimensional data-set, after the conduction of a pure static geometrical analysis we decide to define few quantities based on area, diameter, and length that may give an idea of the dynamic changes experienced by the aorta during a cardiac cycle.

We introduce, therefore, three relative quantities to track the changes in time experienced by the aorta, such as relative Area Changes (AC), relative Diameter Changes (DC) and relative Length Changes (LC) expressed in percentage and defined as follows:

$$AC = \frac{Amplitude(Area)}{A_{v_{time}}(Area)} \tag{4.33}$$

$$DC = \frac{\frac{1}{2}(Amplitude(d_{min}) + Amplitude(d_{max}))}{\frac{1}{2}(A_{v_{time}}(d_{min}) + A_{v_{time}}(d_{max}))} \tag{4.34}$$

$$LC = \frac{Amplitude(l)}{A_{v_{time}}(l)} \tag{4.35}$$

where:

$$Amplitude(\mathbf{X}) = (\max_{i \in time}(\mathbf{X}[i]) - \min_{i \in time}(\mathbf{X}[i])) \tag{4.36}$$

$$A_{v_{time}}(\mathbf{X}) = \frac{1}{8}\sum_{i=1}^{8}\mathbf{X}[i] \tag{4.37}$$

with $\mathbf{X}$ the vector containing the values of the computed quantities (e.g., area, diameter maximum and minimum and length) for the eight time instants. We remark that AC and DC refer to distensibility of the aorta, while LC refers to elongation. Finally we introduced a quantity called Mean Shape, i.e., a dimensionless index ranging between 0 and 1; the more the index is closed to 1 the more the section resembles a circular shape. The Mean Shape (MS) is defined as follows:

$$MS = \frac{A_{v_{time}}(d_{min}(S))}{A_{v_{time}}(d_{max}(S))} \tag{4.38}$$
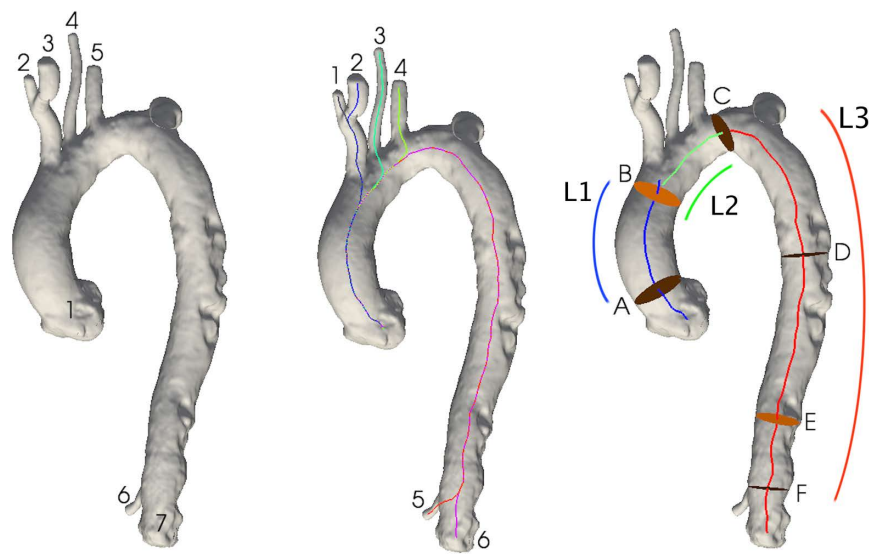
Figure 4.14: Automatic geometric analysis. Left side depicts the 3D model with numbered the seven seed points required to initialise the centerline. The figure central to the panel depicts the 3D model and the six centerlines. The right side of the panel shows the 3D model of the aorta with the six sections A-F indicated: A, level of the STJ; B, 1 cm proximal to brachiocephalic trunk; C, left subclavian artery (LSA), D, 10 cm distal to LSA; E, 20 cm distal to LSA, and F, level of celiac bifurcation. The right panel shows also the centreline subdivision into three regions: L1, ascending aorta (blue line, between sections A and B); L2, aortic arch (green line, between sections B and C); and L3, descending aorta (red line, between sections C and F).

Chapter 5

Results

Retrospective ECG gating or ECG synchronization virtually eliminates cardiac pulsation artefacts and has therefore extended the clinical applicability of CTA to finally also include the aortic root. ECG gating allows cardiac phase-resolved ('time-resolved') cine imaging and visualization, adding a 'fourth dimension' (4D) to this technique - i.e., it is possible to obtain images at different time points during the cardiac cycle. A minimum temporal resolution of eight phases per cardiac cycle can give an adequate perspective of the aortic dynamics. The dateset analysed in this thesis are 4D-CTA of the thoracic aorta composed by eight time steps. The University Medical Center Utrecht provided us the dateset of in total eleven patients of whom eight are aneurysmatic patients, two are dissected patients, and one is an healthy control patient.

5.1 Application of the framework to a 4D dataset: aneurysmatic patients

5.1.1 The dataset

The patients, enrolled by the University Medical Centre Utrecht, The Netherlands, were six male and two female, mean age was 71.0 ± 8.2 years. A median of 2.0 (IQR 1.0 - 2.0) stent-grafts was used. The median interval from the TEVAR procedure to the post-TEVAR dynamic CTA imaging was 0.1 (0.1 - 5.8) months. Patient and procedural characteristics are listed in table 5.1.

5.1.2 4D image segmentation

The results of 4D segmentation have been evaluated by visual inspection. The procedure performed well for all the eight patients composing the dataset.

Table 5.1: Patient and procedural characteristics are demonstrated, including diagnosis, size and brand of the implanted stent-graft(s). The size of the implanted stent-grafts was reported as: DP-DD-GL, where DP is the proximal diameter, DD the distal diameter and GL the stent-graft length. All the measures are expressed in mm. Oversizing rates of the stent-graft compared to aortic diameter are listed for each patient. PAU = penetrating aortic ulcer; TAA = thoracic aortic aneurysm.

Patient	Sex	Age	Diagnosis	stent-graft type	Size graft 1	Size graft 2	Size Graft 3
1	m	79	TAA	Relay, Bolton	42-42-100	38-38-100	
2	m	65	TAA	Relay, Bolton	38-38-100		
3	m	61	TAA	Valiant, Medtronic	38-38-125	40-40-150	44-44-150
4	m	80	TAA	Valiant, Medtronic	36-36-100	38-38-100	
5	m	70	TAA	Valiant, Medtronic	36-36-100		
6	m	75	TAA	Valiant, Medtronic	42-42-150		
7	f	77	TAA	Valiant, Medtronic	38-38-200	38-38-200	
8	f	59	PAU/TAA	Relay, Bolton	34-34-100		

5.1.3   Aortic Diameter and Aortic Area Changes

Area and diameter changes - named respectively ad AC and DC - are shown in table 5.2. We may notice that thoracic aorta distensibility is preserved or increased after TEVAR if referring to the mean values of the patients affected by thoracic aortic aneurysm - i.e., TAA. This observation is no more valid if we inspect more in detail each patient of the dataset, in fact changes in distensibility are more evident in patient 3, 7, and 8.

Aortic diameter and aortic area changes were highest at the level of the sino-tubular junction - STJ - (section A) and were comparable between sexes and between patients that received one or more stent-graft, see table 5.3.

In particular few considerations can be done on AC and AD after the stratification, see table 5.3.

Values of AC for male patients registered an increase at sections E (from 10.3% to 10.5%) and F (from 12.4% to 17.1%), instead for female AC registered an increase in sections A (from 12.4% to 13.4%), C (from 8.8% to 10.5%), E (from 16.1% to 17.3%), and F (from 7.5% to 18.1%). Values of AC for patients with one stent-graft registered an increase at sections C (from 6.1% to 8.9%), E (from 7.0% to 14.4%), and F (from 10.0% to 18.1%), instead for patients with more stent-grafts AC registered an increase in sections A (from 11.8% to 13.4%), D (from 5.4% to 6.7%), and F (from 12.4% to 16.4%).

Values of DC for male patients registered an increase at sections A (from 8.7% to 11.7%), B (from 3.9% to 4.3%), D (from 4.4% to 8.0%), E (from 8.3% to 8.6%), and F (from 8.4% to 12.6%), instead for female DC registered an increase in sections A (from 9.8% to 10.2%) and F (from 4.1% to 11.1%). Values of DC for patients with one stent-graft registered an increase at all the sections (A: from 11.0% to 11.8%, B: from 5.0% to 5.6%, C: from 5.7% to 6.3%, D: from 6.3% to 6.9%, E: from 6.8% to 10.6%, F: from 6.9% to 13.4%), instead for patients with more stent-grafts DC

Table 5.2: Values of AC, DC, LC expressed in percentage for the eight aneurysmatic patients pre-TEVAR (pre) and post-TEVAR (post). A: level of the STJ; B: 1 cm proximal to brachiocephalic trunk; C: left subclavian artery (LSA), D: 10 cm distal to LSA; E: 20 cm distal to LSA, and F: level of celiac bifurcation. L: region between A nd F; L1: region between A and B; L2: region between B and C; L3: region between C and F. We remark that Overall quantities are expression of the mean values per quantity computed.

Patient		AC						DC						LC			
		A	B	C	D	E	F	A	B	C	D	E	F	L	L1	L2	L3
1	pre	6.2	2.0	4.0	5.3	9.0	12.6	5.3	2.2	3.9	3.5	6.5	8.0	3.1	5.7	4.9	3.9
	post	4.9	4.0	4.0	4.5	11.1	14.5	5.6	2.7	2.8	2.7	7.9	9.9	2.9	6.5	6.4	3.9
2	pre	24.8	5.3	5.2	15.6	6.1	15.3	15.2	4.0	3.0	7.9	6.1	11.2	3.2	5.6	6.8	4.8
	post	13.6	7.8	8.5	5.0	14.8	16.8	8.2	3.4	6.8	6.6	10.4	10.4	2.0	7.8	9.0	3.8
3	pre	12.6	9.0	11.9	9.7	12.4	17.3	6.3	4.7	7.1	4.9	8.2	9.8	3.8	4.0	6.6	5.6
	post	17.2	5.2	10.6	5.3	6.9	28.0	11.0	3.0	5.3	15.2	4.6	15.0	3.1	7.9	8.5	3.0
4	pre	12.9	12.0	23.5	5.5	24.1	17.1	7.2	7.8	12.9	3.3	15.9	10.8	3.1	14.1	9.2	3.2
	post																
5	pre	10.4	3.5	4.8	3.0	4.6	8.6	8.5	2.1	4.3	5.0	5.8	6.9	0.8	4.8	4.9	2.3
	post	15.6	7.0	2.7	3.0	9.9	18.9	12.2	6.7	2.8	4.6	5.6	11.4	1.1	4.6	4.8	1.4
6	pre	11.9	4.0	3.6	5.3	5.6	3.5	9.8	2.3	2.2	2.1	7.5	3.6	1.5	4.3	6.0	1.4
	post	14.1	5.2	10.3	10.3	9.5	7.4	19.4	5.5	6.9	10.7	14.6	16.4	2.0	5.9	6.7	3.7
7	pre	15.6	5.2	6.6	1.3	20.6	2.4	9.0	2.5	3.4	0.9	13.2	2.3	1.3	6.5	4.7	1.2
	post	18.3	7.1	7.0	10.3	11.4	6.7	13.1	4.6	5.2	4.4	6.3	6.8	6.4	6.9	5.2	8.0
8	pre	9.2	10.3	10.9	17.9	11.6	12.5	10.6	11.4	13.5	10.1	7.9	5.9	2.1	5.6	9.5	2.5
	post	8.5	7.4	14.0	8.4	23.3	29.5	7.3	6.7	9.0	5.9	11.8	15.5	4.7	15.6	8.8	5.4
Overall pre		12.9	6.4	8.8	7.9	11.7	11.2	9.0	4.6	6.3	4.7	8.9	7.3	2.4	6.4	6.6	3.1
Overall post		13.2	6.2	8.2	6.7	12.4	17.4	11.0	4.7	5.5	7.2	8.7	12.2	3.2	7.9	7.1	4.2

registered an increase in sections A (from 7.0% to 9.9%), D (from 3.1% to 7.4%), and F (from 7.7% to 10.6%). Results of AC and DC are consistent for patients who received more than one stent-graft.

5.1.4 Aortic Elongation Changes

The aortic length changes of L, L1, L2 and L3 for all patients before and after TEVAR are shown in table 5.2. The elongation changes at different segments and the region interested by the stent-graft coverage are depicted in figures 5.1, 5.2, 5.3, and 5.4. The thoracic aorta showed high aortic changes in elongation. Elongation was not preserved after TEVAR in the segments covered with the stent-graft, it instead increased in the segments proximal to the stent-graft.

In detail for patient 1, see table 5.4 and figure 5.1, elongation changes in the aortic arch increased from 4.9% to 6.4% in L2; this observation, besides the fact that the proximal landing zone of the stent-graft is in segments L2, can lead to the conclusion that aortic length have to compensate the stiffness induced by the stent-graft apposition forcing regions before the stent-

Table 5.3: Values of AC, DC, LC expressed in percentage for the eight aneurysmatic patients pre-TEVAR (pre) and post-TEVAR (post). A: level of the STJ; B: 1 cm proximal to brachiocephalic trunk; C: left subclavian artery (LSA), D: 10 cm distal to LSA; E: 20 cm distal to LSA, and F: level of celiac bifurcation. L: region between A nd F; L1: region between A and B; L2: region between B and C; L3: region between C and F. We remark that Overall quantities are expression of the mean values per quantity computed. We report the values stratified for sex (male/female) and number of stent-graft implanted.

Parameter	AC						DC						LC			
	A	B	C	D	E	F	A	B	C	D	E	F	L	L1	L2	L3
male																
Overall pre	13.1	6.0	8.8	7.4	10.3	12.4	8.7	3.9	5.6	4.4	8.3	8.4	2.6	6.5	6.4	3.5
Overall post	13.1	5.8	7.2	5.7	10.5	17.1	11.3	4.3	4.9	8.0	8.6	12.6	2.2	6.6	7.1	3.2
female																
Overall pre	12.4	7.7	8.8	9.6	16.1	7.5	9.8	7.0	8.5	5.5	10.5	4.1	1.7	6.0	7.1	1.8
Overall post	13.4	7.3	10.5	9.3	17.3	18.1	10.2	5.6	7.1	5.1	9.0	11.1	5.5	11.2	7.0	6.7
1 stent-graft																
Overall pre	14.1	5.8	6.1	10.4	7.0	10.0	11.0	5.0	5.7	6.3	6.8	6.9	1.9	5.1	6.8	2.7
Overall post	12.9	6.8	8.9	6.7	14.4	18.1	11.8	5.6	6.3	6.9	10.6	13.4	2.4	8.5	7.3	3.6
2 or more stent-graft																
Overall pre	11.8	7.0	11.5	5.4	16.5	12.4	7.0	4.3	6.8	3.1	10.9	7.7	2.8	7.6	6.4	3.5
Overall post	13.4	5.4	7.2	6.7	9.8	16.4	9.9	3.4	4.4	7.4	6.3	10.6	4.1	7.1	6.7	5.0

graft to elongate more. On the contrary the region (L3) where the stent-graft is deployed shows no changes in elongation that remains constant at 3.9% in L3.

For patient 2, see table 5.4 and figure 5.1, elongation changes in the aortic arch increased from 6.8% to 9.0% in L2; the proximal landing zone of the stent-graft is again in segments L2, same conclusions for patient 1 are valid also for patient 2. On the contrary the region (L3) where the stent-graft is deployed shows a contraction in length from 4.8% to 3.8%.

Patient 3 shows a behaviour similar to patients 1 and 2, see table 5.4 and figure 5.2. Elongation changes in the aortic arch, segment L2, just before the stent-graft increases from 6.6% to 8.5%, instead the stent region L3 shows a contraction in length from 5.6% to 3.0%.

Patient 4 is excluded from our discussion since, as visible in figure 5.2, its complex geometry do not allow to be quantitatively accurate.

Patient 5, see table 5.4 and figure 5.3, shows no elongation changes in the aortic arch; segment L2, just before the stent-graft, register a constant LC at 4.9% pre-TEVAR and at 4.8% post-TEVAR. Instead, the stent region, L3, shows a decrease in LC from 2.3% to 1.4%.

Patient 6, see table 5.4 and figure 5.3, shows an elongation changes in the segments L1 and L3, respectively just before and just after the stent-graft, these values increase from 4.3% to 5.9% in L1 and from 1.4% to 3.7% in L3, the stent region L2 shows a slight length changes from 6.0% to 6.7%.

For patient 7, see table 5.4 and figure 5.4, elongation changes in the aortic arch, segment L2, just before the stent-graft increases from 4.7% pre-TEVAR to 5.2% post-TEVAR. The region covered with the stent-graft, L3, shows an unexpected behaviour and it elongates from 1.2% to 8.0%. This may be due to the fact that L3 is covered by more than one graft and those graft do not overlap each other. The region not covered with stent-graft - have to compensate the stiffness induced by the graft and it lets L3 elongate more.

Last patient is patient 8, see table 5.4 and figure 5.4. Elongation changes in segments L1 and L3, respectively just before and just after the stent-graft increases from 5.6% to 15.6% and from 2.5% to 5.4%, instead the stent region L2 shows a decrease in length changes from 9.5% to 8.8%.
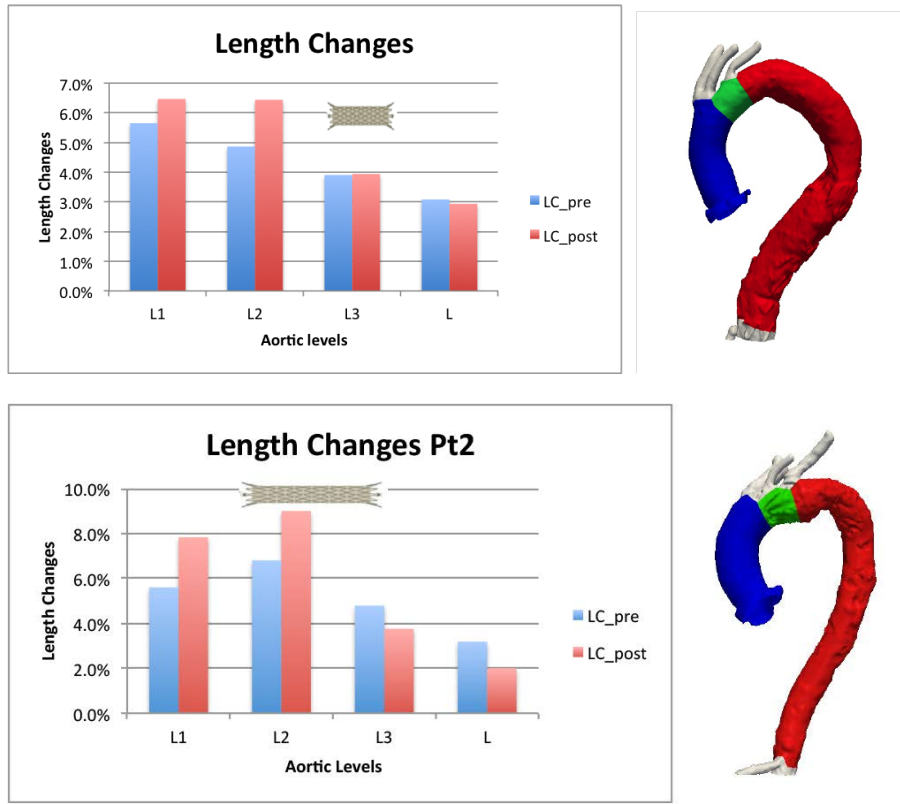
Figure 5.1: Aortic length changes of L, L1, L2 and L3 for patients 1 and 2 before and after TEVAR are depicted in figures.
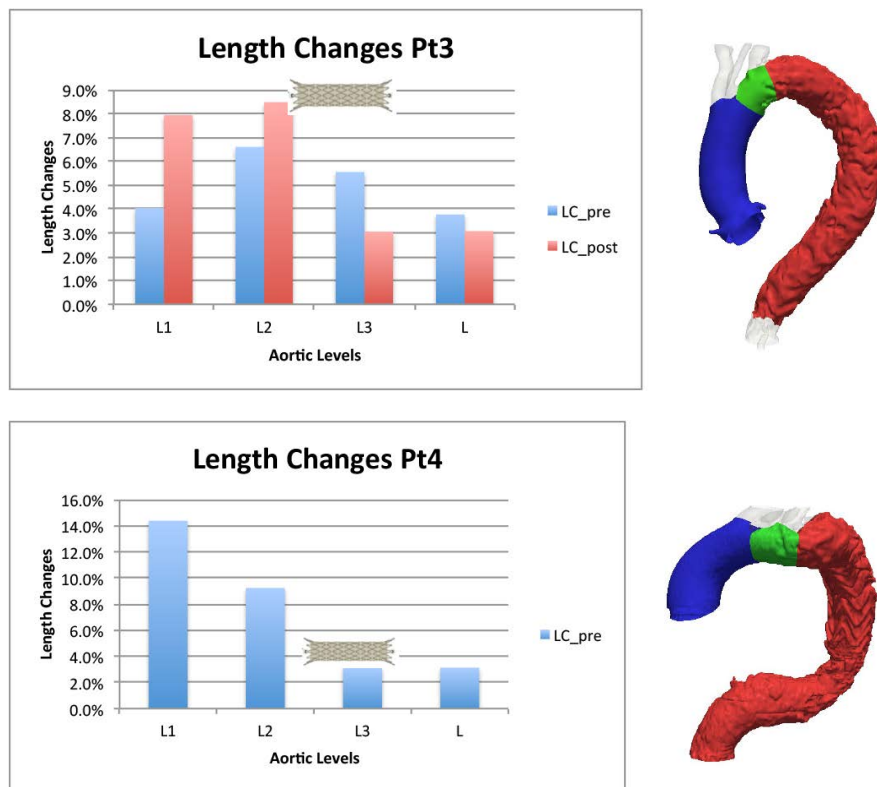
Figure 5.2: Aortic length changes of L, L1, L2 and L3 for patients 3 and 4 before and after TEVAR are depicted in figures. It is worth noting that patient 4 has not been analysed after stent-graft deployment, this is due to the high morphological characteristics of the aorta after-TEVAR that did not permit to perform a precise and reliable analysis.
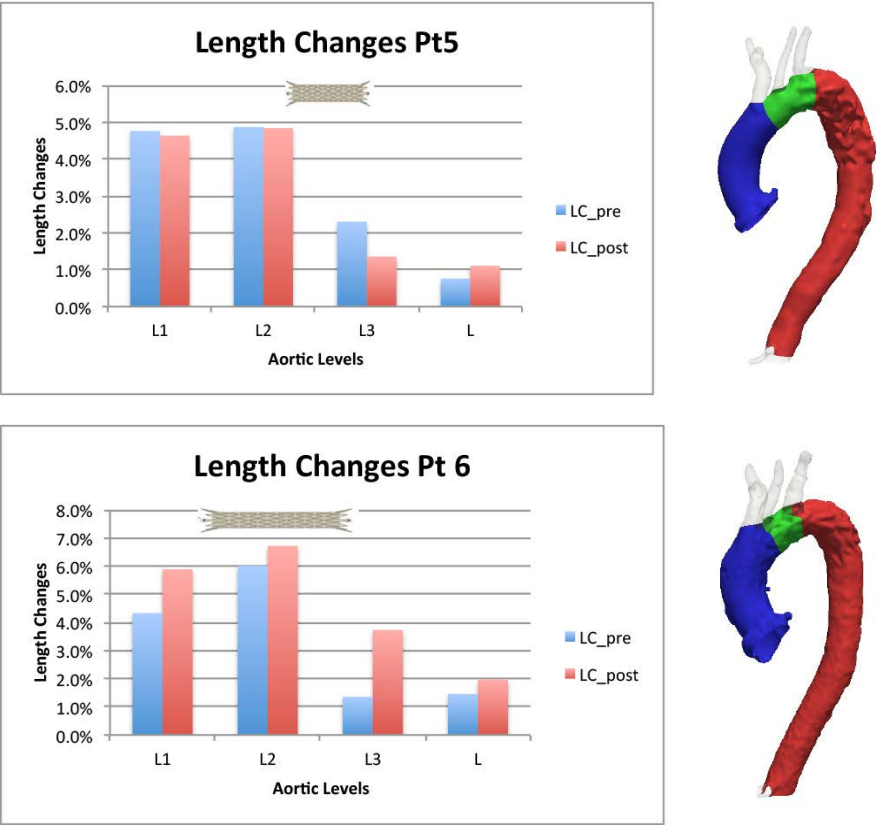
Figure 5.3: Aortic length changes of L, L1, L2 and L3 for patients 5 and 6 before and after TEVAR are depicted in figures.
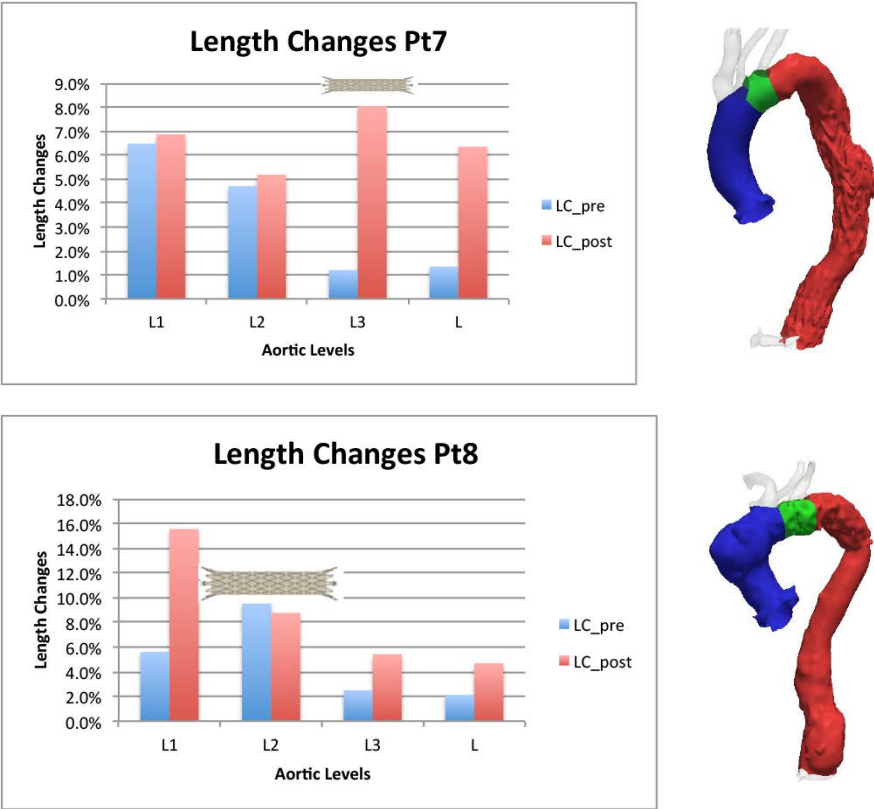
Figure 5.4: Aortic length changes of L, L1, L2 and L3 for patients 7 and 8 before and after TEVAR are depicted in figures.

Table 5.4: Values of length changes pre- and post-TEVAR. The values are stratified based on the stent coverage. Thoracic aorta length changes are displayed as function of stent-graft, we here report length changes before the graft pre- and post-TEVAR, inside the graft, and after the graft for the eight patients affected by thoracic aneurysm.

Patient	before graft			inside graft			after graft		
	location	pre-TEVAR	post-TEVAR	location	pre-TEVAR	post-TEVAR	location	pre-TEVAR	post-TEVAR
1	L2	4.9	6.4	L3	3.9	3.9			
2	L2	6.8	9.0	L3	4.8	3.8			
3	L2	6.6	8.5	L3	5.6	3.0			
4	L2	9.2		L3	3.2				
5	L2	4.9	4.8	L3	2.3	1.4			
6	L1	4.3	5.9	L2	6.0	6.7	L3	1.4	3.7
7	L2	4.7	5.2	L3	1.2	8.0			
8	L1	5.6	15.6	L2	9.5	8.8	L3	2.5	5.4

5.1.5   Mean Shape

The tool computes the mean shape (MS) of the aortic sections A, B, C, D, E, and F. Results are shown in table 5.5. Table 5.5 shows that MS values are slightly higher in the post-TEVAR configuration. We can make a quick consideration: after TEVAR, as figures 5.5 depicts, stent-graft deployment helps maintaining a circular shape to the vessel. The MS index is not changing significantly through the sections considered.
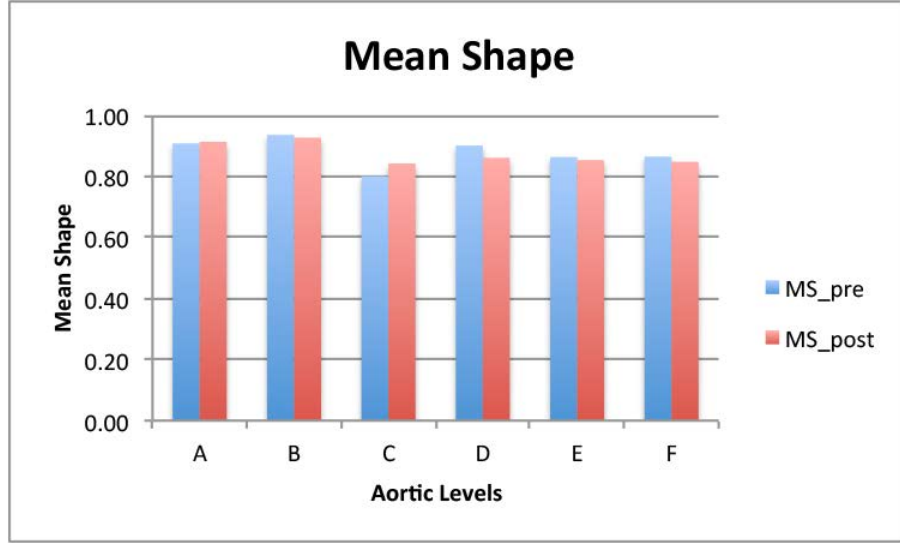
Figure 5.5: Overall Mean Shape (MS) pre- and post-operatively. MS is dimensionless index and ranges between 0 and 1, MS equals to 1 would indicates the perfect circularity of the section. Stent-graft deployment maintains the regularity of the shape of the sections considered (A, B, C, D, E, and F).

5.1.6   Outer Length Changes

Outer length changes - i.e., OLC - are measures that track changes not in time but in space and are reported in table 5.6 and 5.7 for all the hearth cycle intervals. We may notice that OLC values are higher in value for the ascending aorta suggesting that this region is more curve and prone to bending movements. From the single analysis of each patient pre- and post-TEVAR a clear pattern is not emerging. We therefore stratified the patients based on sex or on number of stent-graft received. The stratification as well does not show any significant pattern, but confirm the higher values of OLC for the ascending aorta with respect to the descending aorta and globally reflect a pressure like pattern during the cardiac cycle.

Figures 5.6 5.7 depict the overall changes of the outer length for the ascending and the descending thoracic aorta. OLC measures the differences between maximum and minimum length computed on the outer surface of the thoracic aorta. These measures quantify how much the aorta is bending during the hearth cycle.

Table 5.5: Values of Mean Shape MS for the eight aneurysmatic patients pre-TEVAR (pre) and post-TEVAR (post). A: level of the STJ; B: 1 cm proximal to brachiocephalic trunk; C: left subclavian artery (LSA), D: 10 cm distal to LSA; E: 20 cm distal to LSA, and F: level of celiac bifurcation. We remark that Overall quantities are expression of the mean values per quantity computed.

| Patient | | Mean Shape | | | | | |
		A	B	C	D	E	F
1	pre	0.92	0.95	0.86	0.95	0.89	0.84
	post	0.91	0.97	0.87	0.83	0.78	0.85
2	pre	0.89	0.90	0.64	0.93	0.81	0.88
	post	0.94	0.93	0.90	0.91	0.88	0.84
3	pre	0.96	0.97	0.85	0.76	0.78	0.79
	post	0.92	0.97	0.81	0.77	0.90	0.81
4	pre	0.92	0.96	0.77	0.91	0.90	0.77
	post						
5	pre	0.85	0.97	0.80	0.87	0.90	0.90
	post	0.86	0.95	0.80	0.80	0.90	0.87
6	pre	0.89	0.97	0.90	0.96	0.88	0.93
	post	0.93	0.88	0.79	0.95	0.91	0.91
7	pre	0.92	0.95	0.88	0.91	0.88	0.95
	post	0.92	0.95	0.90	0.85	0.72	0.80
8	pre	0.92	0.82	0.70	0.93	0.86	0.86
	post	0.91	0.85	0.83	0.92	0.89	0.84
Overall pre		0.91	0.94	0.82	0.88	0.86	0.86
Overall post		0.91	0.91	0.83	0.90	0.86	0.88

From the analysis of these quantities two main considerations can be done. First consideration concerns the comparison of overall OLC both pre- and post-TEVAR for the ascending and the descending aorta, see figures 5.6 5.7. In detail OLC of the ascending aorta is double in value with respect to the OLC of the descending aorta in both configurations (pre- and post-TEVAR). Second consideration is that generally ascending and descending aorta decrease their values of OLC after TEVAR. This fact may suggest that the stent-graft contribute to stiffen the aorta and it let bend the post-TEVAR aorta less than the pre-TEVAR aorta.

Stratification of the results does not show any particular behaviour so far.
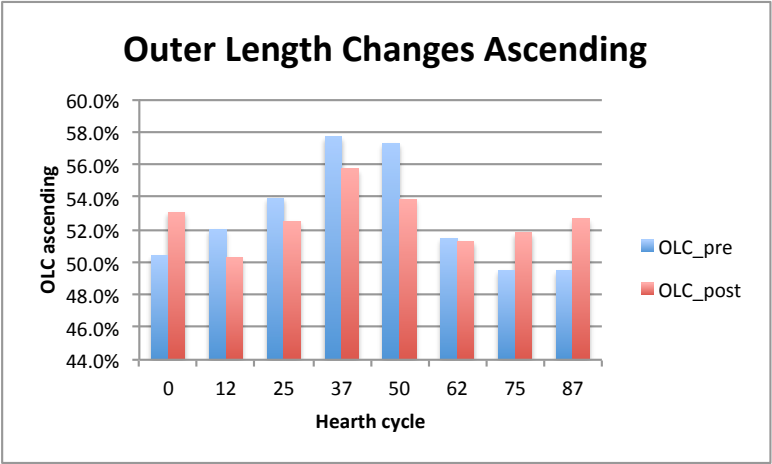
Figure 5.6: Overall OLC Outer Length Changes of the ascending aorta. The x axis carries information on the hearth cycle as percentage of the interval RR, y axis carries information on the percentage of elongation/contraction experienced by the ascending aorta on its outer surface.
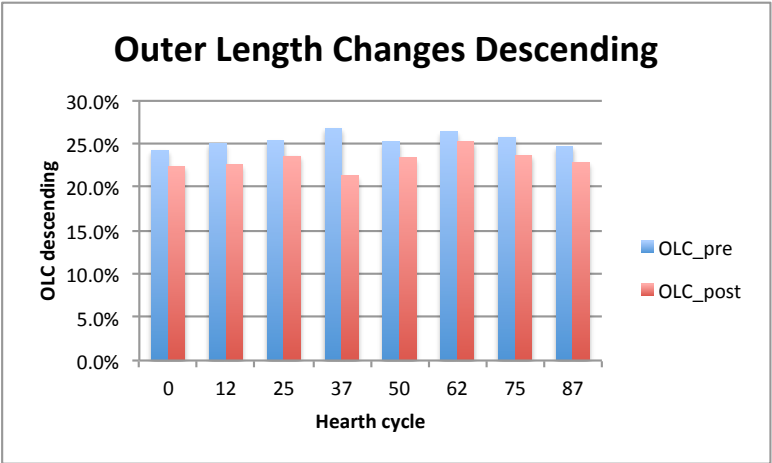
Figure 5.7: Overall OLC Outer Length Changes of the descending aorta. The x axis carries information on the hearth cycle, y axis carries information on the percentage of elongation/contraction experienced by the descending aorta on its outer surface.

Table 5.6: Outer length changes for the eight aneurysmatic patients. Values for each patients and each ascending and descending aortic branch are displayed on the basis of hearth cycle and pre- post-TEVAR configuration.

Patient		Hearth cycle RR%							
		0	12	25	37	50	62	75	87
1 ascending	pre	40.1	43.1	42.3	48.9	40.8	35.9	33.0	40.5
	post	40.3	41.3	42.5	48.1	47.6	43.7	41.6	39.1
1 descending	pre	26.3	25.7	26.0	26.9	24.1	25.0	24.3	24.7
	post	22.9	25.9	24.1	22.3	18.2	35.1	25.0	25.1
2 ascending	pre	38.0	30.0	37.9	42.7	41.1	38.0	35.8	36.6
	post	50.4	53.8	52.3	50.9	57.9	47.4	44.2	50.6
2 descending	pre	21.3	19.5	20.9	21.8	21.4	20.2	21.0	20.9
	post	19.1	21.7	18.0	22.1	22.9	18.9	19.9	16.9
3 ascending	pre	49.6	49.6	49.1	54.0	51.8	49.9	55.7	52.4
	post	42.4	41.8	36.4	38.8	39.2	39.6	39.5	38.6
3 descending	pre	22.3	22.3	29.7	28.2	28.9	28.3	26.8	27.4
	post	23.6	23.4	24.2	22.4	25.2	23.9	25.4	25.7
4 ascending	pre	67.1	76.8	77.6	80.8	87.4	72.1	67.2	63.7
	post	74.9	63.2	75.9	81.5	74.6	72.8	82.8	89.9
4 descending	pre	27.5	36.7	31.4	32.3	33.1	33.5	31.2	30.4
	post								
5 ascending	pre	50.4	49.6	51.4	49.9		50.6	47.9	50.1
	post	48.2	49.2	46.4	47.2	47.5	46.2	47.7	
5 descending	pre	34.3	34.7	33.8	34.5		34.3	34.8	33.1
	post	25.4	24.0	25.5	25.3	23.7	27.3	24.5	24.1
6 ascending	pre	53.0	51.3	52.6	56.5	56.5	51.2	50.3	54.0
	post	62.5	47.3	50.3	45.8	48.8	38.7	47.2	44.6
6 descending	pre	20.6	20.3	20.6	20.9	20.9	20.7	21.0	20.0
	post	23.3	22.4	21.5	18.9	21.7	20.1	21.6	22.8
7 ascending	pre	35.4	37.0	43.2	44.8	41.4	41.0	41.6	34.4
	post	38.6	34.6	40.8		42.5	40.3	40.8	40.4
7 descending	pre	23.3	22.8	20.6	29.0	27.9	27.8	27.9	23.0
	post	24.6	20.2	33.0		33.8	26.1	30.8	26.4
8 ascending	pre	69.5	78.3	77.3	84.1	82.1	73.1	64.6	64.1
	post	67.2	70.7	75.5	77.7	72.9	81.3	70.6	71.3
8 descending	pre	18.0	18.3	19.5	20.6	20.2	21.1	18.6	18.1
	post	17.8	20.2	18.5	16.7	17.9		18.1	18.9
Overall ascending	pre	50.4	52.0	53.9	57.7	57.3	51.5	49.5	49.5
	post	53.1	50.3	52.5	55.7	53.9	51.3	51.8	52.7
Overall descending	pre	24.2	25.0	25.3	26.8	25.2	26.4	25.7	24.7
	post	22.4	22.6	23.5	21.3	23.3	25.2	23.6	22.9

Table 5.7: Outer length changes for the anaurysmatic patients. The results are stratified per gender - ascending and descending - and per number of stent-graft - ascending and descending.

Parameter		Hearth cycle RR%							
		0	12	25	37	50	62	75	87
male ascending	pre	49.7	50.1	51.8	55.5	55.5	49.6	48.3	49.5
	post	53.1	49.5	50.6	52.1	52.6	48.1	50.5	51.6
male descending	pre	25.4	26.5	27.1	27.4	25.7	27.0	26.5	26.1
	post	22.8	23.5	22.7	22.2	22.3	25.1	23.3	22.9
female ascending	pre	52.4	57.7	60.2	64.5	61.8	57.1	53.1	49.3
	post	52.9	52.7	58.2	77.7	57.7	60.8	55.7	55.8
female descending	pre	20.7	20.6	20.0	24.8	24.0	24.5	23.3	20.5
	post	21.2	20.2	25.7	16.7	25.8	26.1	24.4	22.6
one graft ascending	pre	52.7	52.3	54.8	58.3	59.9	53.2	49.6	51.2
	post	57.1	55.3	56.2	55.4	56.8	53.4	52.4	53.3
one graft descending	pre	23.5	23.2	23.7	24.4	20.8	24.1	23.9	23.0
	post	21.4	22.1	20.9	20.7	21.5	22.1	21.0	20.7
more graft ascending	pre	48.1	51.6	53.1	57.1	55.3	49.7	49.4	47.8
	post	49.1	45.3	48.9	56.1	51.0	49.1	51.2	52.0
more graft descending	pre	24.9	26.9	26.9	29.1	28.5	28.7	27.6	26.4
	post	23.7	23.2	27.1	22.3	25.7	28.4	27.1	25.7

5.2 Application of the framework to a 4D dataset: dissected patients and a healthy control case

5.2.1 The dataset

We consider a set of 4-dimensional (4-D) computed tomography angiography (CTA) of the thoracic aorta of two patients acquired before and after the TEVAR surgery and of an healthy control patient, enrolled by the University Medical Centre Utrecht, The Netherlands. The first patient was a 53-year old female with acute thoracic type-b aortic dissection (TBAD), the second patient was a 55-year old male with ruptured TBAD, the healthy control patient was a 49-year old female with no vascular pathology. Two stent grafts were used in both cases. The interval from the TEVAR procedure to the post-TEVAR dynamic CTA imaging was of 6 months. The CTA scans were gained by a retrospective ECG-gated protocol and were performed with a 64-row or 256-row multislice CT system (Philips Medical System, Best, The Netherlands): a three-dimensional scan volume was acquired at 8 equidistant time steps, covering the entire cardiac cycle and providing a 4D data set. The CT images are characterised by a pixel spacing of 0.7×0.7 mm pre-TEVAR for all the three patients, $0.5 \times 0.5 mm$ and $0.8 \times 0.8 mm$ post-TEVAR respectively for the first and the second patient and by a slice thickness of 0.9 mm both pre- and post-TEVAR for the pathological patients and of 1.5 mm for the healthy control patient. For enhanced vessel contrast, each patient received between 90 and 150 mL of a non-ionic contrast medium (Iopromide, Schering, Berlin, Germany), followed by a 60 mL saline chaser bolus. Institutional Review Board approval was obtained for the conduct of this study, and the board waived the need for patient consent.

Table 5.8: Patient and procedural characteristics are demonstrated, including diagnosis, size and brand of the implanted stents graft(s). The size of the implanted stent-grafts was reported as: DP-DD-GL, where DP is the proximal diameter, DD the distal diameter and GL the stent-graft length. All the measures are expressed in mm. Oversizing rates of the stent-graft compared to aortic diameter are listed for each patient.TBAD = thoracic type-B aortic dissection.

Patient	Sex	Age	Diagnosis	stent-graft type	Size graft 1	Size graft 2
1	f	54	TBAD	Endurant Bifurcated, Medtronic	36-36-200	36-36-200
2	m	55	TBAD	Endurant AUI, Medtronic	36-36-150	34-34-200

5.2.2 4D image segmentation

The results of 4D segmentation have been evaluated by visual inspection. The procedure performed well for all the three datasets.

5.2.3   Aortic Diameter and Aortic Area Changes

The aortic diameter and area changes for all patients pre- and post-TEVAR are shown in table 5.9. We may notice (see table 5.9) that thoracic aorta distensibility is preserved or increased after TEVAR if referring to the mean values of the patients affected by TBAD. This observation is no more valid if we inspect more in detail each patient of the dataset, in fact changes in distensibility are more evident in patient 2 (Marfan syndrome).

In particular, analysing patient 1, we can notice that before and after the stent-graft (sections A, B, E, and F) the distensibility is preserved or slightly increased: AC changes from 11.1% to 9.4% in section A, from 5.2% to 5.9% in section B, from 3.4% to 8.4% in section E, and from 8.0% to 13.9% in section F; DC changes from 8.2% to 5.8% in section A, from 3.2% to 3.8% in section B, from 2.6% to 6.2% in section E, and from 4.4% to 6.9% in section F.

Instead in the stent regions (sections C and D) the distensibility shows a decrease: AC changes from 10.7% to 6.1% in section C, and from 7.9% to 5.7% in section D; DC changes from 4.3% to 2.6% in section C, and from 4.0% to 2.9% in section D. After TEVAR the stent segment shows decreased distensibility than the pre-operative aorta suggesting an increase in stiffness possibly induced by the stent-graft apposition. The regions just before and after the graft exhibit preserved or slightly augmented distensibility possibly linked to compensation of graft-induced stiffness.

Furthermore, analysing patient 2, we can notice that before and proximal to the stent-graft the distensibility is increased: AC changes from 8.9% to 11.8% in section A, from 5.0% to 5.4% in section B and from 5.5% to 10.6% in section C; DC changes from 8.2% to 6.0% in section A, from 2.8% to 7.7% in section B and from 4.3% to 5.8% in section C. Instead in the stent and post-stent regions the distensibility shows a high increase; AC changes from 9.3% to 38.0% in section D, from 8.4% to 23.5% in section E and from 1.8% to 22.2% in section F; DC changes from 5.8% to 12.1% in section D, from 5.1% to 9.0% in section E and from 8.2% to 11.5% in section F. This second patient, affected by Marfan syndrome, shows a more variable distensibility at the stent and post-stent regions. This behaviour is compensated by the regions before the stent-graft that, instead, show a more stable distensibility between pre- and post-TEVAR.

5.2.4   Aortic Elongation Changes

The aortic length changes of L, L1, L2 and L3 for all patients before and after TEVAR are shown in table 5.9. The elongation changes at different segments and the percentage of stent-graft coverage are depicted in figure 5.10 and 5.11. The thoracic aorta showed high aortic changes in elongation, most evident in the Marfan patient. Elongation was not preserved after TEVAR in the segments covered with the stent-graft, it instead increased in the segments proximal to the stent-graft. In detail for patient 1, see figure 5.10, elongation changes in the aortic arch increased from 5.9% to

Table 5.9: Values of AC, DC, LC expressed in percentage for the two patients (1 and 2) pre-TEVAR (pre) and post-TEVAR (post) and for the healthy control patient (Healthy). A: level of the STJ; B: 1 cm proximal to brachiocephalic trunk; C: left subclavian artery (LSA), D: 10 cm distal to LSA; E: 20 cm distal to LSA, and F: level of celiac bifurcation. L: region between A nd F; L1: region between A and B; L2: region between B and C; L3: region between C and F. We remark that Overall quantities do not comprehend the healthy control patient.

Patient		AC						DC						LC			
		A	B	C	D	E	F	A	B	C	D	E	F	L	L1	L2	L3
1	pre	11.1	5.2	10.7	7.9	3.5	8.0	8.2	3.2	4.3	4.0	2.6	4.4	2.6	5.9	2.3	3.0
	post	7.0	5.9	6.1	5.7	8.4	13.9	5.8	3.8	2.6	2.9	6.2	6.9	2.2	11.8	10.7	2.4
2	pre	8.9	5.0	5.5	9.3	8.4	1.8	8.2	2.8	4.3	4.0	2.6	4.4	9.4	13.2	9.1	10.3
	post	11.8	5.4	10.6	38.0	23.5	22.2	6.0	7.7	5.8	12.1	9.0	11.5	4.1	7.8	14.9	6.5
Healthy		15.5	7.5	9.3	7.8	9.7	6.5	9.0	3.9	7.3	4.5	5.3	6.0	14.0	8.1	2.9	3.0
Overall pre		10.0	5.1	8.1	8.6	5.9	4.9	8.2	3.0	4.3	4.9	3.8	6.3	6.0	9.6	5.7	6.6
Overall post		9.4	5.6	8.4	21.9	16.0	18.0	5.9	5.8	4.2	7.5	7.6	9.2	3.2	9.8	12.7	4.5

11.8% in L1 and from 2.3% to 10.7% in L2; this observation, besides the fact that the proximal landing zone of the stent-graft is in segments L1 and L2, can lead to the conclusion that aortic length have to compensate the stiffness induced by the stent-graft apposition forcing regions before the stent-graft to elongate more. On the contrary the region (L3) where the stent-graft is deployed shows a decrease in elongation changes from 3.0% to 2.4%. A similar, and even more significant behaviour, is present in the second patient. In fact elongation changes in the aortic arch, segment L2, just before the stent-graft increases from 9.1% to 14.6%. Instead, the stent region, L3, shows a contraction in length from 10.3% to 6.5% (see figure 5.11).

5.2.5   Mean Shape

The tool computes the mean shape of the aortic sections of interest. We can sharply make some quick considerations; one is that patient 1, as figures 5.12 and 5.13 depict, has a circular shape conserved also after TEVAR and this phenomena can be due to the fact that preoperative thrombus confers a tube like shape to the vessel. The second consideration concerns patient 2 to who, see figures 5.12 and 5.13, stent-graft deployment, interesting section D, E and F confers a circular shape and homogenise the index through all of the sections considered.

5.2.6   Outer Length Changes

Outer length changes - i.e., OLC - are reported in table 5.11. We may notice that OLC values are higher in value for the ascending aorta suggesting that this region is more curve and prone to bending movements. From the single analysis of each patient pre- and post-TEVAR a clear pattern is not emerging. Figures 5.8 5.9 depict the overall changes of the outer length for the

Table 5.10: Values of Mean Shape MS for the two dissected patients pre-TEVAR (pre) and post-TEVAR (post) and for the healty control patient. A: level of the STJ; B: 1 cm proximal to brachiocephalic trunk; C: left subclavian artery (LSA), D: 10 cm distal to LSA; E: 20 cm distal to LSA, and F: level of celiac bifurcation. We remark that Overall quantities do not comprehend the healthy control patient.

Patient		MS					
		A	B	C	D	E	F
1	pre	0.93	0.96	0.88	0.86	0.95	0.89
	post	0.95	0.95	0.84	0.91	0.96	0.95
2	pre	0.93	0.97	0.88	0.65	0.71	0.65
	post	0.92	0.92	0.84	0.80	0.89	0.73
Healthy		0.92	0.94	0.87	0.93	0.94	0.94
Overall pre		0.93	0.96	0.88	0.75	0.83	0.77
Overall post		0.93	0.94	0.84	0.86	0.93	0.84

ascending and the descending thoracic aorta. The same considerations made for the OLC of the anaurysmatic patients are valid also for the dissected patients. From the analysis of the results emerge that, see figures 5.6 5.7, OLC of the ascending aorta is double in value with respect to the OLC of the descending aorta in both configurations (pre- and post-TEVAR). In the descending aorta, the region interested by the pathology, shows small values of OLC post-TEVAR with respect to pre-TEVAR configuration and even more visible it shows smaller values of OLC pre- and post-TEVAR with respect to the healthy control patient. This can suggest the fact that the pathology affecting those patients stiffens the descending aorta and lets it bend less with respect to a healthy aorta. Post-TEVAR the analysis of OLC does not show significant difference suggesting that the stent-graft does not introduce particular bending configurations, further investigation are needed and the sample size should be larger.
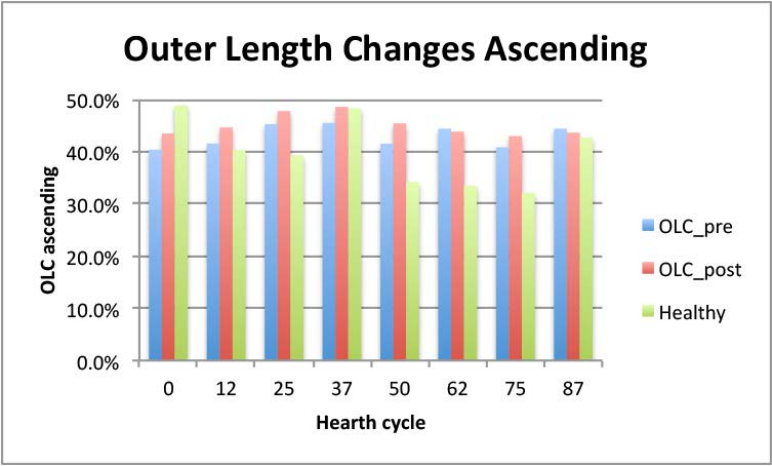
Figure 5.8: Overall OLC Outer Length Changes of the ascending aorta. The x axis carries information on the hearth cycle, y axis carries information on the percentage of elongation/contraction experienced by the ascending aorta on its outer surface.
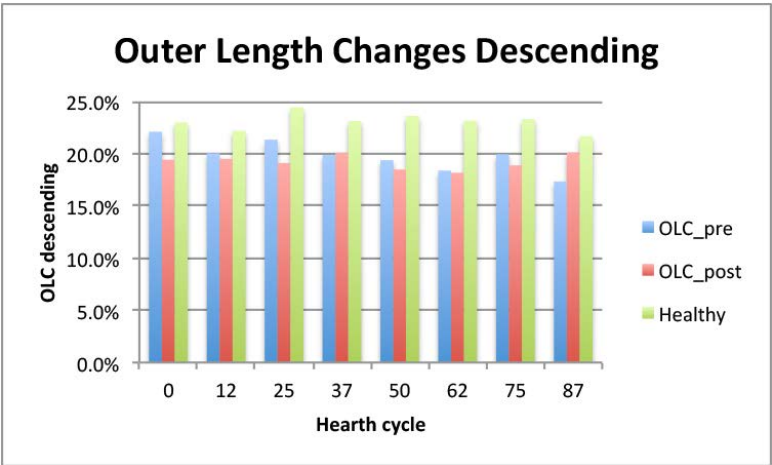
Figure 5.9: Overall OLC Outer Length Changes of the descending aorta. The x axis carries information on the hearth cycle, y axis carries information on the percentage of elongation/contraction experienced by the descending aorta on its outer surface.
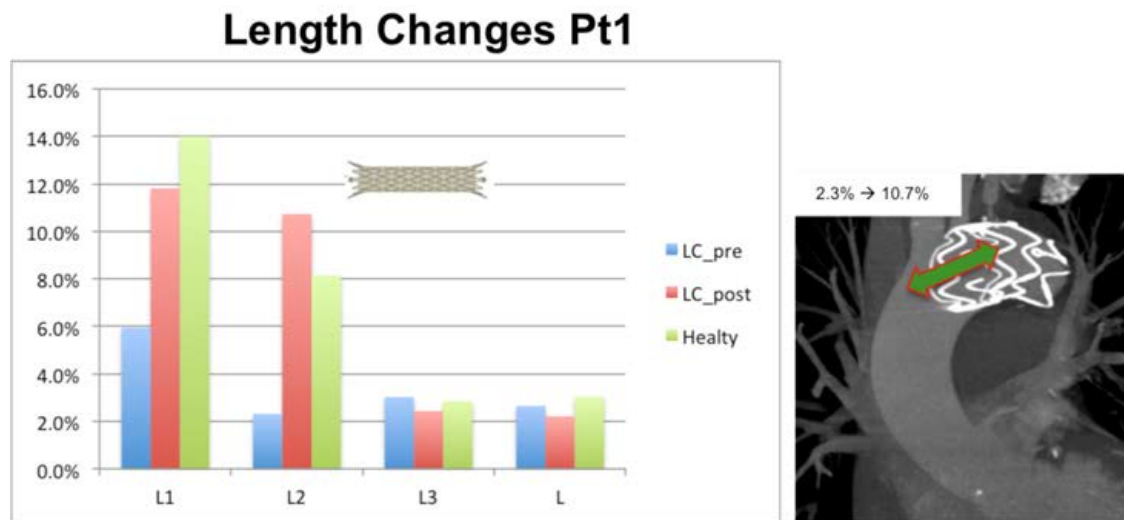
Figure 5.10: Aortic length changes of L, L1, L2 and L3 for patient 1 before and after TEVAR are depicted in left side together with the healthy control patient. The x axis carries information on the stent-graft coverage for the different length segments. We remark that elongation changes in the aortic arch (segment L2) increased from 2.3% to 10.7%. On the right side a figure enhancing the stent-graft proximal landing zone related to the increased in elongation of L2.
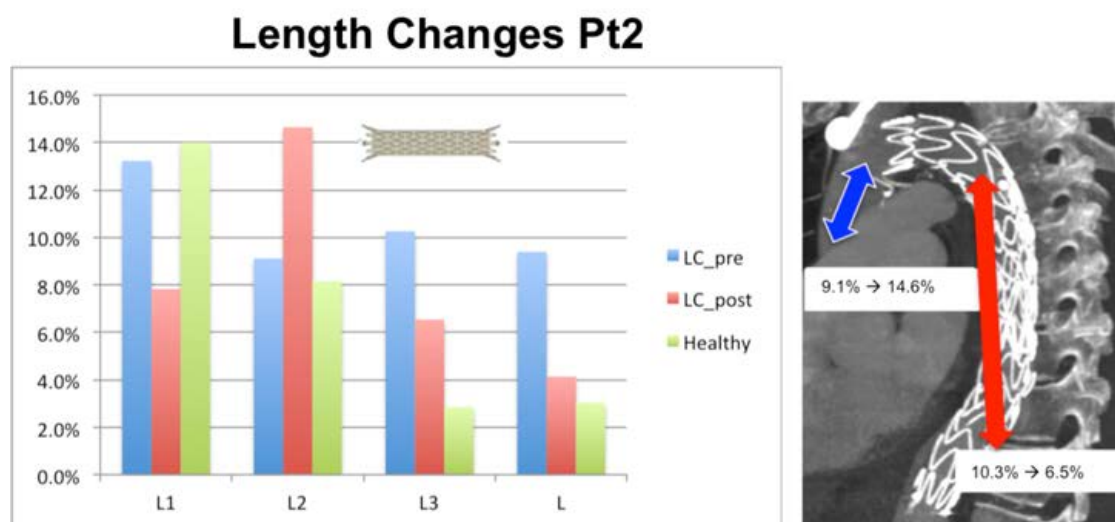
Figure 5.11: Aortic length changes of L, L1, L2 and L3 for patient 2 before and after TEVAR are depicted in left side together with the healthy control patient. The x axis carries information on the stent-graft coverage for the different length segments. We remark that elongation changes in the ascending aorta, segment L2, increases from 9.1% to 14.9%. Furthermore, the stented region, L3, shows a contraction in length from 10.3% to 6.5% . On the right side a figure enhancing the stent-graft region related to the increased in elongation of L2 and the contraction of L3.
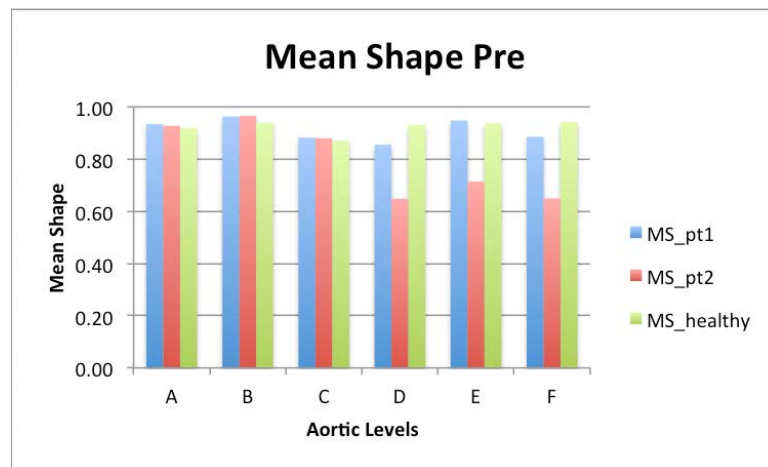
Figure 5.12: Mean Shape (MS) pre-operatively. MS is dimensionless index and ranges between 0 and 1, MS equals to 1 denotes the circular shape of the section. Patient 1 shows a circular shape through all the sections (A, B, C, D, E and F), instead patient 2 shows at the region affected by the dissection pathology (D, E and F) a less regular shape.
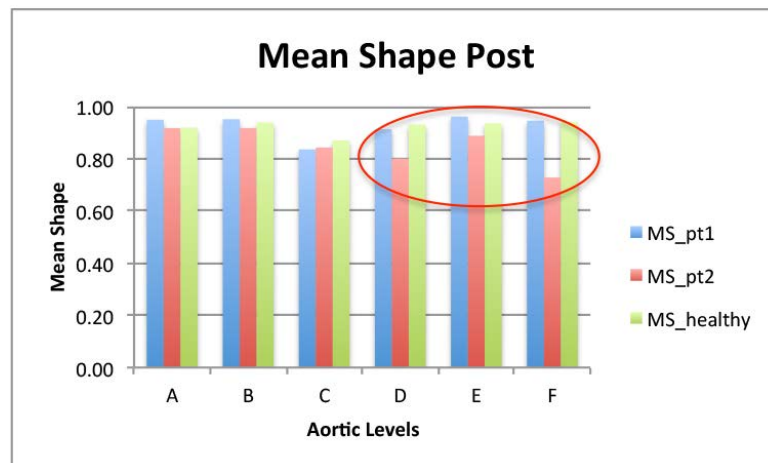
Figure 5.13: Mean Shape (MS) post-operatively. MS is dimensionless index and ranges between 0 and 1, MS equals to 1 denotes the circular shape of the section. It is worth noting that, comparing patient 1 and patient 2, the stent-graft deployment (section D, E and F) confers to those regions a more circular shape and homogenise the index through all of the sections considered.

Table 5.11: Outer length changes for the dissected patients and for the healthy control patient. Values for each patients and each ascending and descending aortic branch are displayed on the basis of hearth cycle and pre- post-TEVAR configuration.

Patient		Hearth cycle RR%							
		0	12	25	37	50	62	75	87
1 ascending	pre	41.1	42.2		47.0	42.6	49.1	42.3	49.2
	post	48.7	47.7	44.5	52.2	46.3	49.8	47.7	51.5
1 descending	pre	16.3	17.2		16.3	16.8	16.1	16.5	15.7
	post	17.8	19.5	16.5	19.0	17.9	18.2	18.5	18.4
2 ascending	pre	39.7	41.0	45.3	44.1	40.5	39.8	39.4	39.6
	post	38.3	41.6	51.1	45.0	44.6	37.9	38.3	35.8
2 descending	pre	28.0	22.8	21.3	23.4	22.0	20.6	23.4	18.9
	post	21.0	19.5	21.7	21.2	19.1	18.1	19.3	21.8
Healthy	ascending	48.9	40.4	39.4	48.3	34.2	33.5	32.2	42.7
	descending	23.0	22.2	24.5	23.1	23.6	23.2	23.3	21.7
Overall ascending	pre	40.4	41.6	45.3	45.5	41.6	44.4	40.9	44.4
	post	43.5	44.7	47.8	48.6	45.4	43.9	43.0	43.6
Overall descending	pre	22.1	20.0	21.3	19.9	19.4	18.4	20.0	17.3
	post	19.4	19.5	19.1	20.1	18.5	18.2	18.9	20.1

Chapter 6

Final remarks

The advancement in diagnostic imaging has enabled CT angiography to be gated with electro-cardiography (ECG) to free images from cardiac pulsation artefacts, allowing reconstruction of specific aortic segments. ECG gated CT allows time-resolved image visualisation, adding a fourth dimension (4-D) to this technology (Fleischmann and Miller, 2007) (Weber et al., 2009). The present study aims at expanding the knowledge in the field of stent-graft behaviour in patients affected by thoracic aortic pathologies. The tool described in this work is designed to provide a work-flow that in an automated and leaned fashion can process medical images, create 3D models, extract geometric features from a given vascular tree in a quantitative manner, and compare these quantities before and after TEVAR. The user interactions within the different assignments along the entire procedure has to be elevated at the highest level possible, in other words the potential users do not have to take decisions that can invalidate repeatability and reproducibility of the results.

6.1 Conclusion

Chapter 1 describes the anatomy, the histology and the pathology of the thoracic aorta. It describe the technique used to analyse the dynamic environment that constitute the aorta, in particular the 4D-CTA, time resolved computed tomography angiography. Moreover the chapter gives an overview of the aortic lesions and the treatment used actually in the surgical settings to treat these specific lesions, the so called Thoracic EndoVascular Aortic Repair (TEVAR). The chapter investigate the limitation of this endovascular technique and the related risks, first of all the still unknown modification induced by a rigid stent-graft to a dynamic environment such as the one of the aorta. The chapter is concluded with a first introduction to the aim of this dissertation.

Chapter 2 contains a review of the literature concerning the geometric characterization of the aorta from patient specific images. The chapter is divided into two main sections: one focusing on the geometric feature extraction from static computed tomography angiography (CTA), the other focusing on the geometric feature extraction from dynamic CTA. The chapter finish with an excursus over the issues that are still open in the field of endovascular aortic repair. This issues claim for a more detailed insight into the pulsatile environment of the thoracic aorta.

Chapter 3 describes the image enhancing and the segmentation techniques exploited in this work. Moreover the chapter describes the workflow implemented in order to obtain a lean and quick 4D segmentation procedure. This means that the pipeline developed gives the possibility to segment an entire 4D CTA dataset in one shot starting from the segmentation only of the first time instant. The first time instant is then exploited to segment the subsequent instant accounting for less user interaction and time consuming.

Chapter 4 is the core of this work. It describes in detail the steps performed to carry on the geometric feature extraction of the thoracic aorta. First the computation of the centerline, the definition of a bifurcation reference system, the branch extraction procedure, and the bifurcation reference system registration. Moreover the chapter gives a description of the measures extracted such as: outer surface length, area and diameter of specific automatic extracted levels of interest, and the length of the centerline between the levels of interest previously identified.

Chapter 5 describes and summarize the results obtained exploiting the tool described in Chapters 3 and 4 applied to two 4D CTA dataset. One dataset is composed of eight aneurysmatic patients, the other is composed of two dissected patients and an healthy patient used as control. The tool has performed well for all patients highlighting interesting findings that lead to the following conclusion. The thoracic aorta showed high aortic changes in both distensibility and elongation, most evident in the Marfan patient (patient 2 see figure 5.11). Distensibility was preserved or increased after TEVAR in the region just distal to the stent-graft. Elongation was not preserved after TEVAR in the segments covered with the stent-graft, it instead increased in the segments proximal to the stent-graft (see figures 5.10 and 5.11). This observation might potentially have implications for stent-graft sizing, design, durability, and related complications. Limitations of our study included the low sample size. Additional studies with larger cohorts are required to test our tool and therefore this study serves as a base for future studies.

6.2 Future work

Although we have approached several aspects regarding the procedure of the automatic segmentation and the geometric feature extraction, this study has still some limitations calling for further developments as discussed in the following. *Image quality and artefacts avoidance*: due to contrast medium and/or presence of medical device in the chest, such as pacemaker or mechanical aortic valve, the acquired CTA of the aorta are not always processable right away. We perform basic enhancement technique but in some cases these are insufficient. There is a clear need of a pre-processing pipeline to improve image quality and to avoid the presence of artefacts overall the metallic one. *Image segmentation*: the pipeline developed for the segmentation of the 4D CTA dataset has some nice advantages that are briefly the less user interference and the speed up of the entire dataset 3D reconstruction. But on the other hand is not integrated yet with the image pre-processing. *The automatic tool for geometric features extraction*: it permits to automatically extract six levels of interest and their related geometric quantities such as area, minimum and maximum diameter, and length. The tool is fast and precise but the identification of the levels of interest has to became more robust especially at the regions where the aorta undergoes the major dynamic displacements as for example at the sinotubular junction. Moreover the tool could be supplied with other measures such as torsion and tortuosity. The supra-aortic branches should be included in the geometric analysis and the outer surface length would be computed also for the aortic arch and not only for ascending and descending aorta. Last but not least the tool would be equipped with a function to register the 3D models of the pre-TEVAR stage onto the models of the post-TEVAR stage in order to supply a comparison in terms of both qualitative - visualization - and quantitative - measures - changes. *Results*: we developed a simple quantitative analysis of the changes experienced by the aorta during the cardiac cycle both pre- and port-TEVAR. The idea to be developed in future work is to perform a statistical analysis of the results obtained on larger dataset to find possible biomarkers able to describe the effect of the stent-graft on a dynamic and complex environment as the one of the thoracic aorta and able to suggest the best practice to the surgeons in order to perform a thoracic endovascular repair with the certainty of a good and stable outcome for the patient.

Appendix A

Virtual TEVAR based on pre-operative images: a computational fluid dynamic study

A.1 Introduction

Thoracic endovascular aortic repair (TEVAR) is a consolidated endovascular procedure to treat thoracic aorta aneurysms[1] or dissections[2] (Erbel et al., 2014) (Fihn et al., 2014). The procedure is performed through a catheter-guided deployment of one or more stent-grafts, which are metallic tubular structures covered with a Dacron skirt. Thanks to its minimally-invasive approach, TEVAR has changed and extended management options of aortic diseases, in particular for those patients who are unsuitable for standard open surgery. Besides being a low-risk treatment, TEVAR has also some not negligible drawbacks; in fact it is associated with in-hospital mortality between 2.6-9.8% and neurological complications between 0.6-3.1% (Tolenaar et al., 2013). Other complications documented after TEVAR are related to the device or procedure, including endoleaks, migration or collapse of the stent graft, development of a false aneurysm and malperfusion of principal and peripheral organs (Grabenwöger et al., 2012). In any case, to assess success and outcomes of procedure, adequate follow up examinations need to be scheduled (Desai et al., 2012) and particular attention has to be taken in considering an adequate landing zone and a small attach angle of the stent-graft to the vessel wall (Grabenwöger et al., 2012). Such aspects of TEVAR procedure call for a quantification and/or prediction of aortic hemodynamics before and

---

[1] An aneurysm is a localized or diffuse dilation of an artery, either saccular or fusiform shaped, with a diameter at least 50% greater than the normal size of the artery.

[2] Aortic dissection occurs when a tear in the inner wall of the aorta causes blood to flow between the layers of the wall of the aorta, forcing the layers apart.

after surgery.

In this context, computational fluid-dynamics (CFD) has proven to be a useful and effective tool to provide insight into patient-specific aortic hemodynamics (Steinman et al., 2003) and to support decision making process (Chung and Cebral, 2015) (Auricchio et al., 2014).

The aim of our work is to provide an advanced method to predict possible post-TEVAR geometrical configurations and the corresponding hemodynamics of the thoracic aorta based on pre-TEVAR computed tomography angiography (CTA) images. Several approaches have been proposed to study the mechanics and the hemodynamics after-TEVAR, but to the best of our knowledge there is still room for innovation. In fact, our approach is different in a sense that, exploiting the centerline of the vessel under investigation, it is possible to reconstruct more than a virtual post-TEVAR model. Moreover, we evaluated the goodness of our models through the comparison of the CFD computed on the virtual post-TEVAR models and the real post-TEVAR configuration.

Among the approaches proposed in the past it is important to cite Lam et al. (2008). They computed the drag force acting on a stent-graft using computational fluid dynamics techniques; they segmented the lumen of the aorta from CT images. Moreover they determined the centerline of the aorta by fitting a cubic spline curve through the centroids of the cross-sections of the segmented aorta lumen. This centerline is used as the template for generating stent-graft models of different settings based on given geometric parameters and using the software Rhinoceros. Cheng et al. and Fung et al., both in 2008, carried on similar studies (Fung et al., 2008) (Cheng et al., 2008). In 2009 Figueroa et al. assess the displacement forces acting on a thoracic stent graft using CFD simulations (Figueroa et al., 2009b). They perform a virtual modification of the pre-TEVAR configuration with the usage of a software *Stanford Virtual Vascular Laboratory* that realizes idealized models of the vascular system with circular cross-sections and these individual artery models are joined to the artery model thrugh boolean union operations.

The framework takes as input the pre-TEVAR CTA images and, based on these images, reconstructs the patient specific 3D model. This model is digitally manipulated to obtain different virtual post-TEVAR configurations to be evaluated through CFD simulations. We perform a comparison between the virtual and the real post-TEVAR configurations from both the geometrical and the haemodynamical point of view in particular focusing on the region of interest that is the saccular aneurysm, where TEVAR can introduce the major modifications. We exploit CFD analysis to confirm the ability of our models to predict real post-TEVAR environment and we discuss on the basis of geometrical measures and hemodynamic measures the reliability of our technique.

A.2 Material and methods

In the following section we describe how to generate the post-TEVAR virtual models from the pre-TEVAR patient-specific image dataset. Moreover, we illustrate the procedure to compare the different models both in term of geometric and computational fluid dynamics analysis with respect to the real post-TEVAR configuration.

A.2.1 Clinical Summary

The patient is a 48-year-old male suffering hypertension and having descending thoracic aortic aneurysm with maximum diameter of 5.5 cm. Given his condition, the patient has been selected for endovascular treatment in order to exclude the aneurysm area using one stent-graft Medtronic Valiant sized 28-24-150 mm, with the proximal landing zone covering the origin of the left subclavian artery and the left common carotid artery. The patient also received a left carotid-subclavian bypass with a Goretex prothesis 6 mm sized. Final angiographic control has been performed after surgery in the absence of endoleaks. The CT scans are composed by two datasets: i) pre-TEVAR scan performed two months before the surgery (ii) post-TEVAR scan performed two months after the surgery, see figure A.1. CT images were acquired using a 16-slice unit (150 mAs, 110 kVp; acquisition thickness 5 mm, pitch 1.5; reconstruction thickness 1.2 mm). The images are characterised by a pixel spacing of 0.8×0.8 mm pre-TEVAR and post-TEVAR, and by a slice thickness of 1 mm both pre- and post-TEVAR. For enhanced vessel contrast, an intravenous administration of 100 mL of iodinated contrast material was given to the patient; the scan started after the contrast medium reached the aortic arch. Institutional Review Board approval was obtained for the conduct of this study, and the board waived the need for patient consent.

A.2.2 Image processing

Medical image processing is one of the key steps of the present framework. In particular, the image processing is composed by two main steps: i) image segmentation and reconstruction of 3D aortic lumen profile; ii) manipulation of the pre-operatie aortic lumen to create the virtual post-TEVAR configuration. In the following, we discuss these two steps.

Image segmentation

We perform image segmentation of the two CTA datasets, image segmentation is typically used to extract objects and boundaries, as in our case the lumen of the vessel, from a background. We perform the image segmentation of the two MSCT scans with the open source tool Vascular Modeling ToolKit (*www.vmtk.org*) and more precisely we exploit the level set technique, that is an implicit non-parametric type of segmentation, whose zero-level iso-surface is the vascular

region of interest (Antiga et al., 2008). The 3D reconstructed model can be exported in .vtp, vtk polygonal data format, or .stl, stereolithography format, such that it can be subsequently elaborated for CFD purpose. It worth nothing that we were able to include a significant portion of the supra-aortic branches, accounting also for the subclavian bypass, only for the post-TEVAR case while only the proximal parts of such aortic branches are included for the pre-TEVAR case due to a limited extension of the scan volume in longitudinal direction, results are depicted in figure A.2. Moreover, the stent-graft segmentation is performed only for visualization purpose; in fact the main interest of this work is to define the surface of the pre- and post-TEVAR aortic lumen.
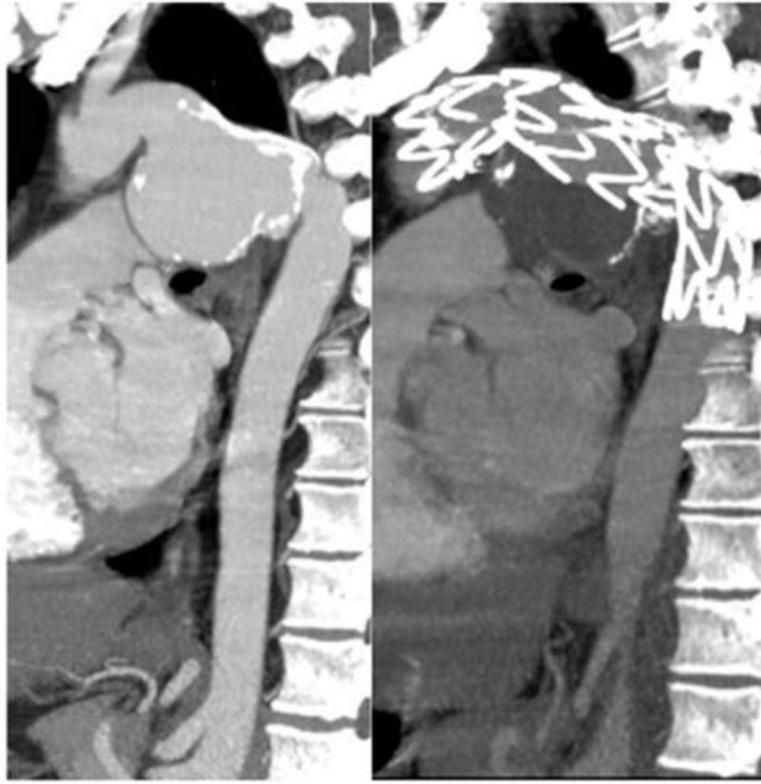
Figure A.1: Computed tomography - CT - with intravenous contrast agent administration. Figure shows thoracic aortic aneurysm on the left panel and aortic remodelling induced by stent-graft apposition on the right panel.

Generation of post-TEVAR models

In order to achieve our goal we need to provide the definition of two fundamental concepts: the concept of centerline and the concept of Voronoi diagram. The centerline of an object is defined as its medial axis that is the locus of centers of maximal spheres inscribed into that specific object. The Voronoi diagram of a set of points P on $\partial\Omega$, given a volume $\Omega \in \mathbb{R}^3$ with boundary $\partial\Omega$, is
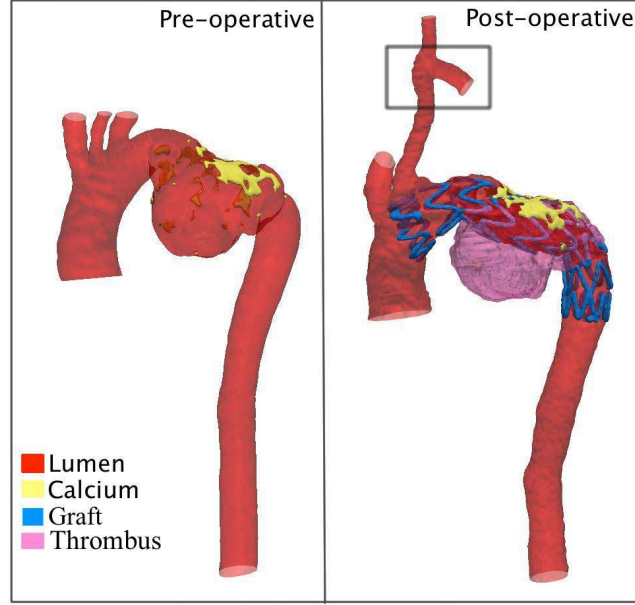
Figure A.2: 3D geometry reconstruction of pre-TEVAR (left panel) and post-TEVAR aorta (right panel). A box contours the bypass graft that has been performed at the left common carotid artery. We show, for visualisation purpose, calcium, thrombus, and the stent-graft.

defined as the union of the regions in $\mathbb{R}^3$ associated with $p \in P$, whose points are closer to p than to any other point of P.

$$V(p) = \{x \in \mathbb{R}^3 | dist(p, x) \leq dist(p, P)\} \tag{A.1}$$

The vertices of the Voronoi diagram represent a subdivision of a volume into a set of partially overlapped spheres. The centerline is traced exploiting the Voronoi diagram and lays on the center of locally largest spheres inscribed in the surface. More in detail, for the computation of the centerline an advanced equation has to be solved, which has to minimize an energy functional. The solution results in the recovery of a path traced between two or more points - i.e., one or more source points and one or more target points provided by the user. This path is minimal for points more internal to the object. Those points are evaluated on the center of maximal inscribed spheres computed through the Voronoi diagram.

From those two definitions it comes up that evaluating the centerline, the envelope of the Voronoi spheres, and by exploiting the marching cubes algorithm it is possible to generate a discrete surface (Ford et al., 2014). For further detail on this part please refer to Antiga's PhD thesis (Antiga, 2002a). The method consists in four steps, see figure A.3:

1. aneurysm removal;

2. centerline generation;

3. voronoi diagram transportation;

4. vessel surface reconstruction.

Step 1 begins with the calculation of two couple of centerlines, four in total. The first couple, which defines the forward direction, is computed using as source point the inlet section of the model and as target points the aneurysm sac dome and the outlet section downstream the aneurysm. The second couple, which defines the backward direction, is computed exploiting as source point the outlet section downstream the aneurysm and as target points the aneurysm sac dome and the inlet section. Once the two cuple of centerlines are calculated it is possible to locate on them the points delimiting the aneurysm sac. The diverging point between the line entering the aneurysm and the one along the vessel is identified for both couple of centerlines and the point one maximal sphere away from the aneurysm is selected as clipping point. The centerline and the Voronoi diagram between the clipping points belonging to the aneurysm sac are removed (Ford et al., 2014). The next step to perform lies on the generation of a new centerline between the clipping points just mentioned. As the centerline is generated the Voronoi diagram can be reconstructed in the region where it has been deleted. This process is performed by transporting the remaining Voronoi points along the new generated centerline exploiting the parallel transport normal system built on these centerlines (Ford et al., 2014). Once the Voronoi Diagram has been transported, the surface is recovered by merging all the maximum inscribed spheres build on the vertexes of the diagram.

We propose two methods slightly different but based on the same workflow described above. In detail the two methods use two different thechnique for the centerline generation. One performs a cubic spline interpolation of the clipped centerlines in the region of the aneurysm sac, the other exploits the centerline of the pre-TEVAR model. We therefore obtain two virtual post-TEVAR models:

- virtualPostI: the post-TEVAR lumen, virtually reconstructed from the pre-TEVAR images interpolating the vessel centerline in the aneurysm region using a cubic spline;
- virtualPostII: the post-TEVAR lumen, virtually reconstructed from the pre-TEVAR images keeping the original vessel centerline as path for the reconstruction of the post-TEVAR scenario.

We compare the two virtual models (virtualPostI and virtualPostII) among them and with respect to the realPost, i.e., the real post-TEVAR lumen profile resulting from the segmentation of the post-TEVAR images of the case under investigation.

A.2.3   Real and virtual post-TEVAR models: geometrical measures

Our aim is to compare geometrically virtualPostI, virtualPostII, and realPost. We therefore introduce three geometric measures to characterize qualitatively and quantitatively the differences
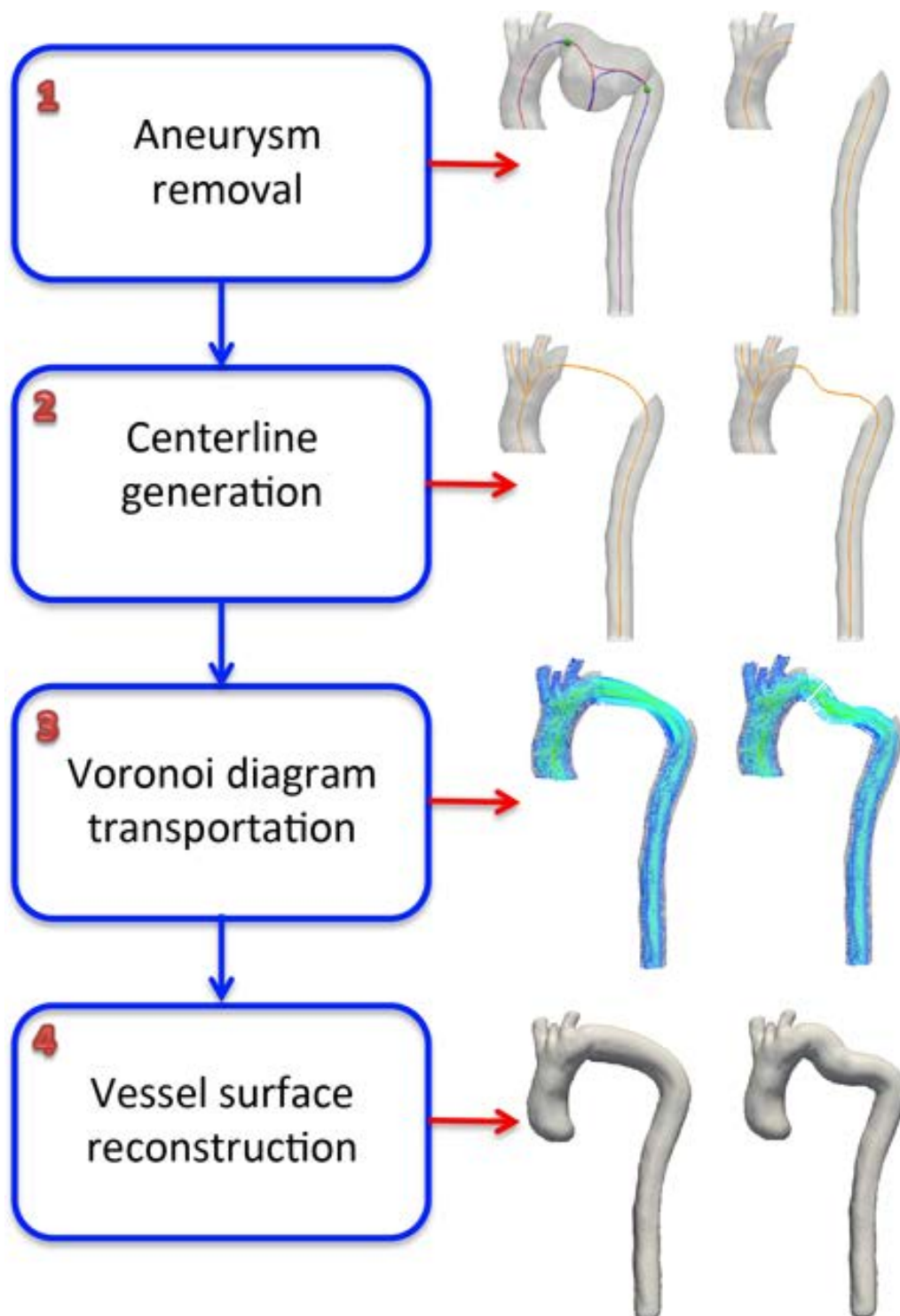
Figure A.3: In figure are depicted the steps performed to obtain 3D models of virtualPostI and virtualPostII from pre-TEVAR patient-specific surface.

between them:

- surface distance (SurfDist);

- gaussian surface curvature (GSC);

- section areas.

To calculate SurfDist we make a registration of the virtualPostI and the virtualPostII 3D models surfaces onto the realPost model. We exploit the iterative closest point method [citare] to carry out the registration of the model surfaces as implemented in *vmtk*. Afterwards, we measure SurfDist, defined as the point-wise minimum euclidean distance of the input surface from a reference surface, in particular we perform the measures between (i) virtualPostI and realPost and between (ii) virtualPostII and realPost. SurfDist is calculated with the following equation:

$$SurfDist(x_1) = \min_{x_2 \in S2}(dist(x_1, x_2)) \qquad \forall x_1 \in S1 \qquad (A.2)$$

where $x1 = (x, y, z)$, $x2 = (x, y, z)$ are coordinates of the points respectively of the surfaces S_1 - virtualPostI or virtualPostII - S_2 - realPost -, and $dist$ is the Euclidean distance. Instead Gaussian Surface Curvature (GSC) at a given point is defined as, the product of the principal curvatures, κ_1 and κ_2 at that point (Kühnel, 2006).

$$GSC = \kappa_1 \kappa_2 \qquad (A.3)$$

The sign of the Gaussian curvature can be used to characterise the surface (figure A.4):

- If $GSC < 0$, the surface will be saddle shaped;

- If $GSC = 0$, the surface is said to have a parabolic point;

- If $GSC > 0$, the surface will be dome like, locally lying on one side of its tangent plane.
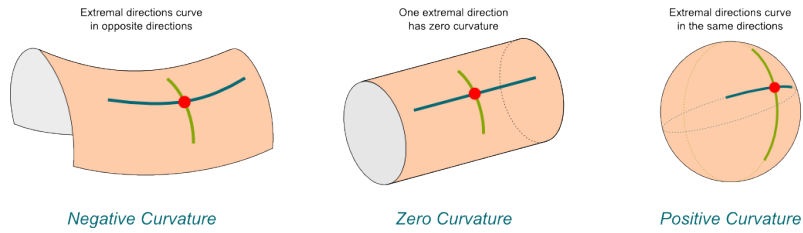
Figure A.4: From left to right: a surface of negative Gaussian curvature (hyperboloid), a surface of zero Gaussian curvature (cylinder), and a surface of positive Gaussian curvature (sphere).

GSC integrate SurfDist helping in catching local phenomena such as the roughness induced by the metallic meshes of the stent-graft on the surface, that SurfDist does not gather.

To ensure a quantitative comparison between the 3D models we decide to introduce specific regions of the aorta (see figure A.5), as previous studies did (Cheng et al., 2014):

- cross-section A, a section perpendicular to the centerline at the mid-ascending aorta;

- cross-section B, a section perpendicular to the centerline after the branching of the left

common carotid artery;

- cross-section C, a section perpendicular to the centerline central to the aortic arch, where the aneurysm has its larger diameter;

- cross-section D, a section perpendicular to the centerline at the aortic arch distal to the left common carotid artery;

- coronal-section E, a longitudinal plane showing the entire aortic arch.

As mentioned before the three investigated models are registered onto each other to permit the robust and precise definition of the aforementioned sections. All the sections are defined with the same procedure, performed with Paraview (Ayachit, 2015). For sections A, B, C, and D we measure the area that is computed triangulating the section of interest and then summing the area of each triangle over the entire section.
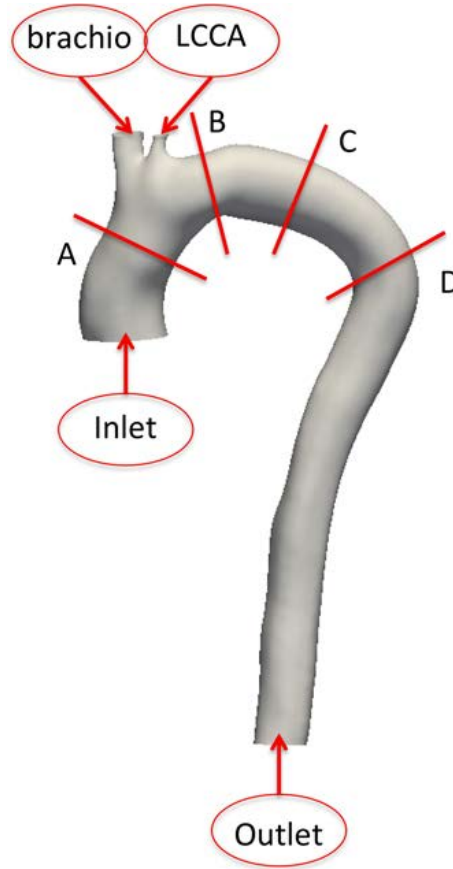
Figure A.5: Specific region of the aorta chosen to evaluate local geometric and fluid dynamic quantities such as cross-sectional area and velocity. Cross-section A, a section perpendicular to the centerline at the mid-ascending aorta, between the Inlet section and the brachiocephalic artery (brachio). Cross-section B, a section perpendicular to the centerline after the branching of the left common carotid artery (LCCA). Cross-section C, a section perpendicular to the centerline central to the aortic arch, where the aneurysm has its larger diameter. Cross-section D, a section perpendicular to the centerline at the aortic arch distal to the LCCA. In figure is also depicted and labelled the Outlet section belonging to the descending aorta.

A.2.4 The CFD cases

In addiction to the geometrical analysis we perform also a fluid dynamic analysis. We performed a CFD study for all the models under investigation focusing on pressure, velocity and wall shear stress (i.e., the numerical output), exploited also in previous biomechanics works, see for example Figueroa et al. (2009b) and Auricchio et al. (2014).

Mesh generation, numerical model, and simulation process

Numerical simulations are carried out by solving the incompressible unsteady $Navier - Stokes$ equations in the region of interest, hereafter denoted by Ω. We assume a Newton rheology - i.e., constant viscosity, commonly considered correct for large and medium size vessels (Formaggia et al., 2010). Let $\mathbf{u}(x, y, z, t)$ and $p(x, y, z, t)$ be blood velocity and pressure, respectively, $\rho = 1.0 \, g/cm^3$ the constant blood density and $\mu = 0.035 \, Poise$ the viscosity. Then the $Navier - Stokes$ equations read

$$\begin{cases} \rho \partial u/\partial t + \rho(u \cdot \nabla)u - \nabla \cdot (\mu(\nabla u + \nabla^T u)) + \nabla p = 0 \\ \nabla \cdot \mathbf{u} = 0 \end{cases} \tag{A.4}$$

for $x, y, z \in \Omega$ and $0 < t \leqslant T$ where $T = 1 \, s$ is the duration of the time interval of interest. The time step was chosen equal to $0.01 \, s$. These equations need to be completed by suitable initial and boundary conditions. The initial conditions are null velocity and pressure fields, corresponding to fluid at rest. As for the boundary conditions, we distinguish three types of boundaries.

- We prescribe null velocity on the lumen, embedding the trace of endografts, assuming that the artery is rigid.

- On the ascending aorta, slightly distal to the aortic valve, we prescribe flow rate by selecting a parabolic velocity profile yielding at each instant the flow wave-form considered in (Morbiducci et al., 2009).

- On the supra-aortic sections and on the descending aorta, we prescribe conditions based on a classical three-element Windkessel modeling of the distal circulation. This means that the peripheral impedance at each outflow section is represented by two resistances R1 and R2 and one compliance C (RCR model). The specific values of these parameters are taken from Kim et al. (2009) and modified for the virtual models as the bypass has not been represented (see Table A.1).

In order to have only the geometry as a degree of freedom, the same values for these boundary conditions were set in all the three models. It is worth reminding that we are predicting post-TEVAR configuration starting from pre-TEVAR 3D model; the bypass is therefore replaced by its equivalent RCR model in the virtualPostI and in the virtualPostII - in detail we adopt

$R_1 = 1180\,dyn\,s\,cm^{-5}$ $R_2 = 8323\,dyn\,s\,cm^{-5}$ and $C = 1.7e^{-4}\,cm^5\,dyn^{-1}$. The bypass is instead taken into account geometrically for the realPost CFD analysis. Moreover, the region of interest is artificially extended, by inserting at the boundary sections, cylindrical regions called flow extensions. The flow extensions are designed to extend the inflow and the outflows of five times the diameter of the section to be extended and their role is to reduce the impact of modeling choices and uncertainties in the boundary conditions on the numerical results in the region of interest (Morbiducci et al., 2009). Flow extensions are added with the open source library *vmtk*. Numerical simulation is based on the finite element method. In this paper we use tetrahedral elements, which are particularly versatile and suited for complex geometries like those considered. Mesh generation is carried out using the tools available in the *vmtk* library. The details of the mesh for each investigated case are reported in Table 1. To perform the simulations, we use the open-source C++ library LifeV (www.lifev.org), a collaborative project including EPF Lausanne, Politecnico di Milano, INRIA Paris, and Emory University. As a trade-off between accuracy and computational costs, we use mixed P1bubble-P1 elements, providing piecewise continuous linear interpolation enriched by a cubic bubble for the velocity, and piecewise continuous linear approximation for the pressure. The CFD simulations are performed with 64 cores (4 AMD opteron 6272 at 2.1GHz) for three cardiac cycles and require 1 week of computing to produce the results. We choose to perform the analysis on three cardiac cycles since the solution in velocity and pressure demonstrate to change not in a significant way from the third cardiac cycle on. The results of the last cycle have been used for the subsequent analysis. For what concern Wall Shear Stress (wss), for Newtonian fluids flowing upon a planar surface, it is determined according to Newton's law by the equation:

$$\tau = \mu \cdot \frac{du}{dy}$$

where μ is the kinetic viscosity, u the fluid velocity, y the distance from the surface and du/dy the velocity gradient, namely the shear rate $\dot{\gamma}$ (sec^{-1}).

Wss parameter is of arising clinical interest, even though actually no written consensus is present. Wall shear stress with pressure seems to play a role in defining the drag forces acting on a stent-graft, see Figueroa et al. (2009b).

A.3   Results

We here present the result of the geometrical measures and the results of the numerical simulations (CFD). When analysing the numerical results, we investigate the output - i.e., velocity, pressure, and wss - overall and in detail for the sections already introduced at a certain relevant time instant

Table A.1: RCR - R expressed in $dyn\,s\,cm^-5$ and C expressed in $cm^5\,dyn^{-1}$ - prescribed at the outflow of the three computational domains. In table brachio refers to brachiocephalic artery and LCCA refers to left common carotid artery, for more deteils refer to figure A.5

BC	R_1	R_2	C
postVirtualI & II			
brachio	1196	8000	$1.6440e^{-4}$
LCCA + bypass	1180	8323	$1.7e^{-4}$
descending	188	2950	$4.82e^{-4}$
realPost			
brachio	1196	8000	$1.6440e^{-4}$
LCCA	1180	18400	$7.7e^{-5}$
bypass	970	15200	$9.340e^{-5}$
descending	188	2950	$4.82e^{-4}$
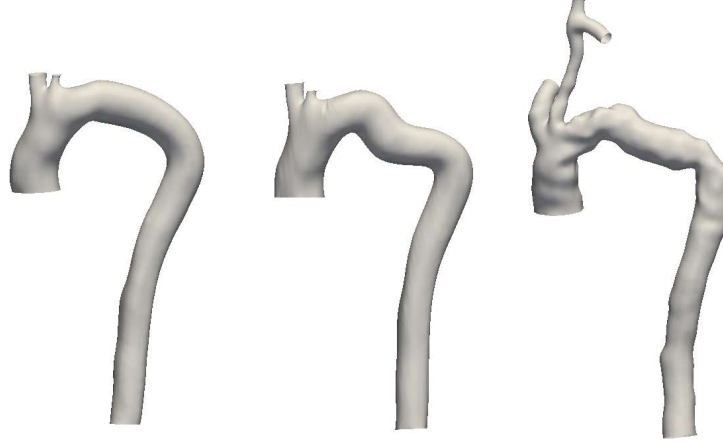
Figure A.6: The three models under investigation; respectively from left to right: virtualPostI, virtualPostII and realPost.

of the cardiac cycle. This specific time instant is related to the systolic peak and is selected at T = 0.2s of the heart cycle.

A.3.1   Post-TEVAR and virtual post-TEVAR models: geometrical measures

In figure A.6 we show the 3D reconstructed models namely, virtualPostI, virtualPostII, and realPost. The results of the surfDist are depicted in figure A.7, related quantitative description of surface distance are carried by Table A.3. By visual inspecting the models, it is clear that aneurysms are completely excluded. The magnitude of surface distance (SurfDist) between virtualPostI and realPost reaches $5.31 \pm 4.15 mm$ (see Table A.3) most evident at the region distal to left subclavian artery, where the distal landing zone of the stent-graft will be deployed (see figure A.7

Table A.2: Mesh details for each investigated cases: realPost, virtualPostI and virtualPostII.

Case	Nodes	Elements	DOFs
realPost	488,519	2,939,806	10,773,494
virtualPostI	490,530	2,963,527	10,852,701
virtualPostII	472,163	2,858,889	10,465,319

Table A.3: Surface distance for the three investigated cases: realPost, virtualPostI and virtualPostII.

SurfDist[mm]	Min	Max	Mean	SD
virtualPostI VS realPost	0.0017	21	5.31	4.15
virtualPostII VS realPost	0.000009	17	2.46	1.87

red region). The magniture of SurfDist between virtualPostII and realPost reaches $2.46 \pm 1.87mm$ (see Table A.3) homogeneously distributed over the entire aorta (see figure A.7 - right).

Gaussian Surface Curvature (GSC) is depicted in figure A.8. GSC shows a smooth and homogeneously distributed pattern for virtualPostI, see figure A.8 left panel, and a similar macroscopic pattern in virtualPostII and postReal; see figure A.8 central and right side of the panel. The saddle region, characterized by a negative GSC, is highlighted in blue and is in the middle of the aortic arch, instead the elliptic regions, characterized by a positive GSC, are located for both models just after the left common carotid artery and at the begin of the descending aorta. The same pattern is not highlighted at the aortic arch of the virtualPostI model that is completely missing the saddle region. It is worth noting that the realPost shows local variation due to the stent-graft mesh that affect the surface of the aorta producing oscillation in GSC; we do not have this local pattern in the virtual models, in fact we reproduce the virtual surgery and not the stent-graft surface modification.

Concerning the area measures at pre-defined sections we can state that area of sections A, B, C, and D changes through the models. It is worth noting that the stent-graft does not expand completely to touch the lumen surface, such an issue results in a thrombotic area surrounding the graft and a reduction in cross-sectional area of the stented aorta (see figure A.6). These differences in area are reported in Table A.4.

A.3.2 CFD cases: velocity

We decide to analyse and compare the magnitude velocity at sections A, B, C, D, and E (see figure A.9) for the three models, virtualPostI, virtualPostII and realPost at time t_{sys}.

In section A at t_{sys} we found that the velocity contours show a similar pattern, i.e. both the three models shows a similar velocity. In section B and D at t_{sys} we can see that the increase

Table A.4: Sections areas for the three investigated cases: realPost, virtualPostI and virtualPostII.

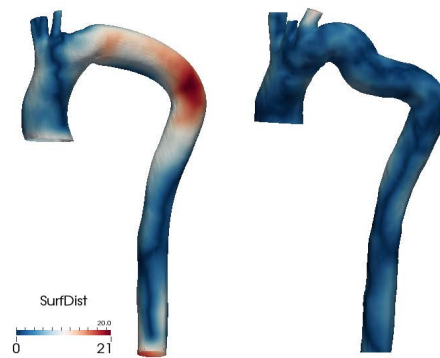| Section Area$[cm^2]$	A	B	C	D
realPre	6.2	10.5 (aneurysm included)	21.1	6.7
realPre	6.2	6 (aneurysm excluded)	21.1	6.7
realPost	6.3	3.5	5.1	2.9
virtualPostI	6.8	6	5.4	5.5
virtualPostII	6.9	6	6.2	4.8

Figure A.7: Point-wise SurfDist expressed in mm from the surfaces of realPost and virtualPostI depicted on the surface of virtualPostI (left); point-wise distance expressed in mm from the surfaces realPost and virtualPostII depicted on the surface of virtualPostII (right).

Figure A.8: GSC for the three models

of velocity for all the three cases is located at the bottom wall of the aorta. Those two sections are extremely peculiar since they correspond to proximal and distal landing zones of the stent-graft. An example is reported in figure A.9 for section B, where we register a maximum velocity magnitude of 80 cm/s for virtualPostI and virtualPostII instead it reaches 110 cm/s for realPost. Section C belongs to the region where the aneurysm has its maximum enlargment pre-TEVAR and is central to the virtual geometrical modifications. This section, always at time t_{sys}, shows a similar pattern of velocity contour for virtualPostII and realPost (see figure A.9), where high values of velocity are attached to the superior part of the aorta's wall. Instead in the model virtualPostI this pattern is completely different, due to the fact that the geometry of the aorta at this region is different for virtualPostI with respect to virtualPostII and realPost, see figure A.6.

In figure A.10 are depicted the velocity streamlines at t_{sys} for the three reconstructed models between sections B and D. Figure A.10 shows that values of velocity increase where the flow undergoes a change in direction in particular at the aortic arch just after the left common carotid artery and at the begin of the descending aorta (figure A.10). It is worth noting that the streamlines after section B behave in a different manner for the three models. Looking closer at that section in virtualPostI we can verify that, due to the smooth reconstruction, no vortexes are present. This remark is not observable for virtualPostII and realPost where just after section B the streamlines highlight a swirling pattern more emphasized for realPost. Globally we register a maximum velocity of 199 cm/s for virtualPostI, of 222 cm/s for virtualPostII and of 251 cm/s for realPost.

It is worth noting that the geometrical shape of the three models is the major parameter influencing the CFD analysis since the set-up for all the cases has been decided univocal and identical.

A.3.3 CFD cases: flow, numerical results

We introduced before, in the section related to image segmentation, that the CTA of the patient has been acquired differently pre- and post-TEVAR (post TEVAR the images include the bypass and a larger portion of the aorta's side branches). Therefore 3D models virtualPostI and virtualPostII fail to represent the exact geometry of brachiocephalic artery and left common carotid artery (see figure A.6). To be sure that those geometric differences does not influence the flow split between branches we measure and display the numerical flow calculated with the CFD. We can notice that at different levels brachiocephalic trunk, left common carotid artery and descending aorta - see figures A.11 - of the aortic arch the flow shows an identical pattern for all the three models investigated, in particular at the brachiocephalic artery where the geometric difference is underlined the most. Moreover at the left common carotid artery we have a slight increase in the flow but not in its shape. The finding is although compensated with the fluxes registered in the descending aorta.
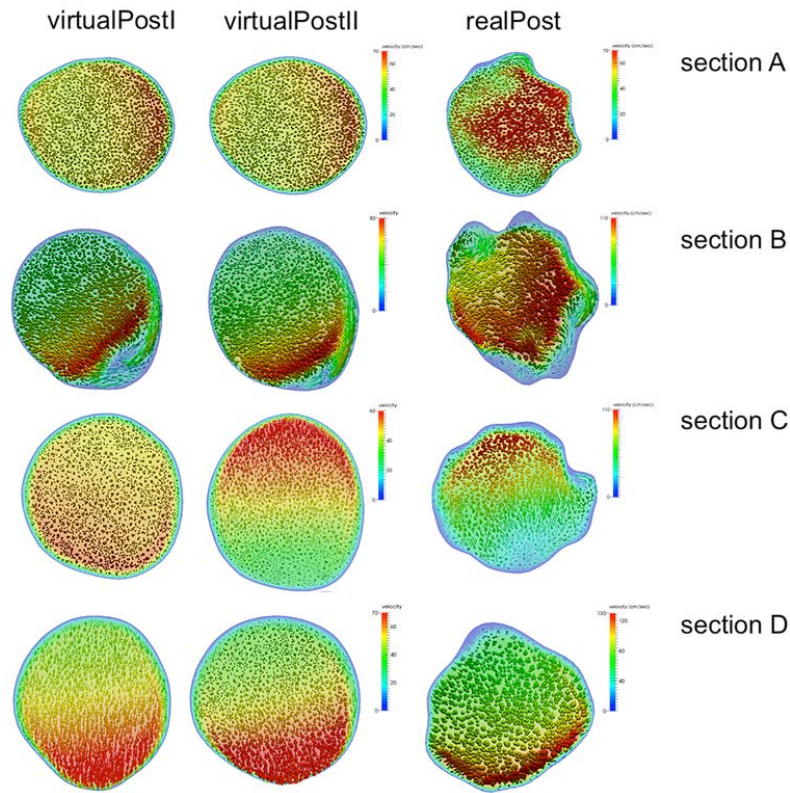
Figure A.9: Velocity contour plot for the investigated cases at section A (first row), B (second row), C (third row), and D (fourth row). Time t_{sys} equals to 0.2 s the systolic peak is considered. The corresponding velocity magnitude (cm/s) is used to color the sections. First column refers to virtualPostI, second column to virtualPostII, and third column to realPost models respectively.
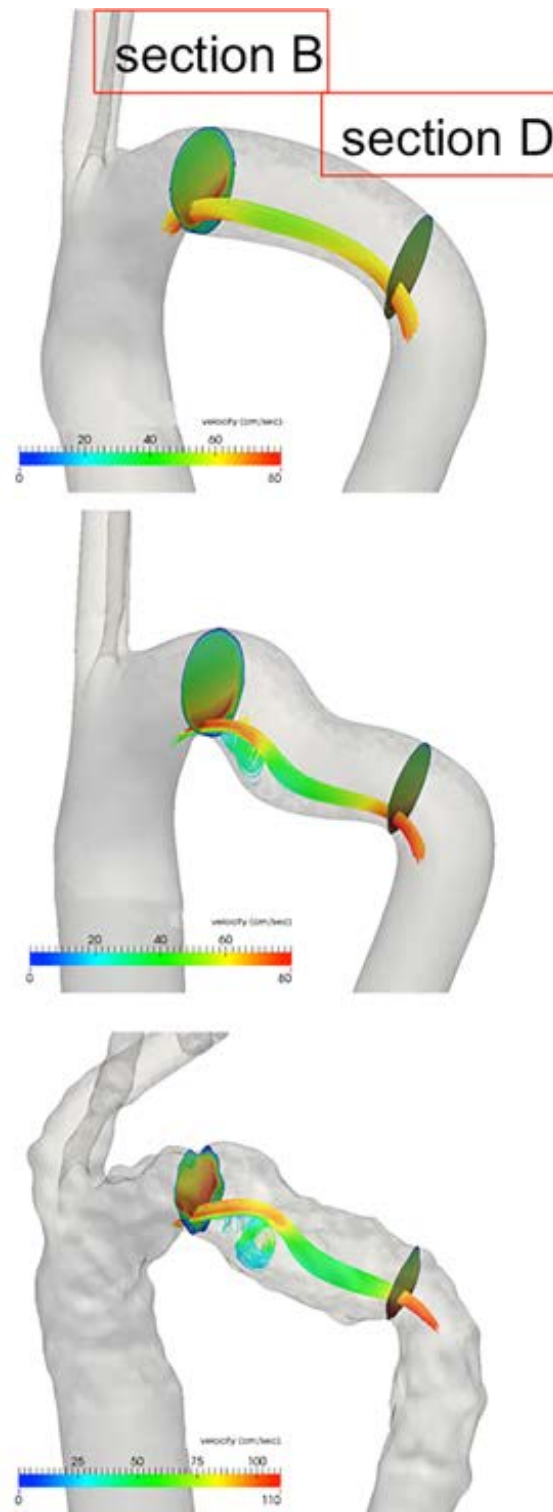
Figure A.10: Streamlines of the velocity field for the investigated cases at t_{sys} the systolic peak. Streamlines are computed between sections B and D that are the proximal and distal landing zones for the deployment of the stent-graft. The cases are depicted respectively from left to right: virtualPostI, virtualPostII, and realPost. Velocity is expressed in cm/s.
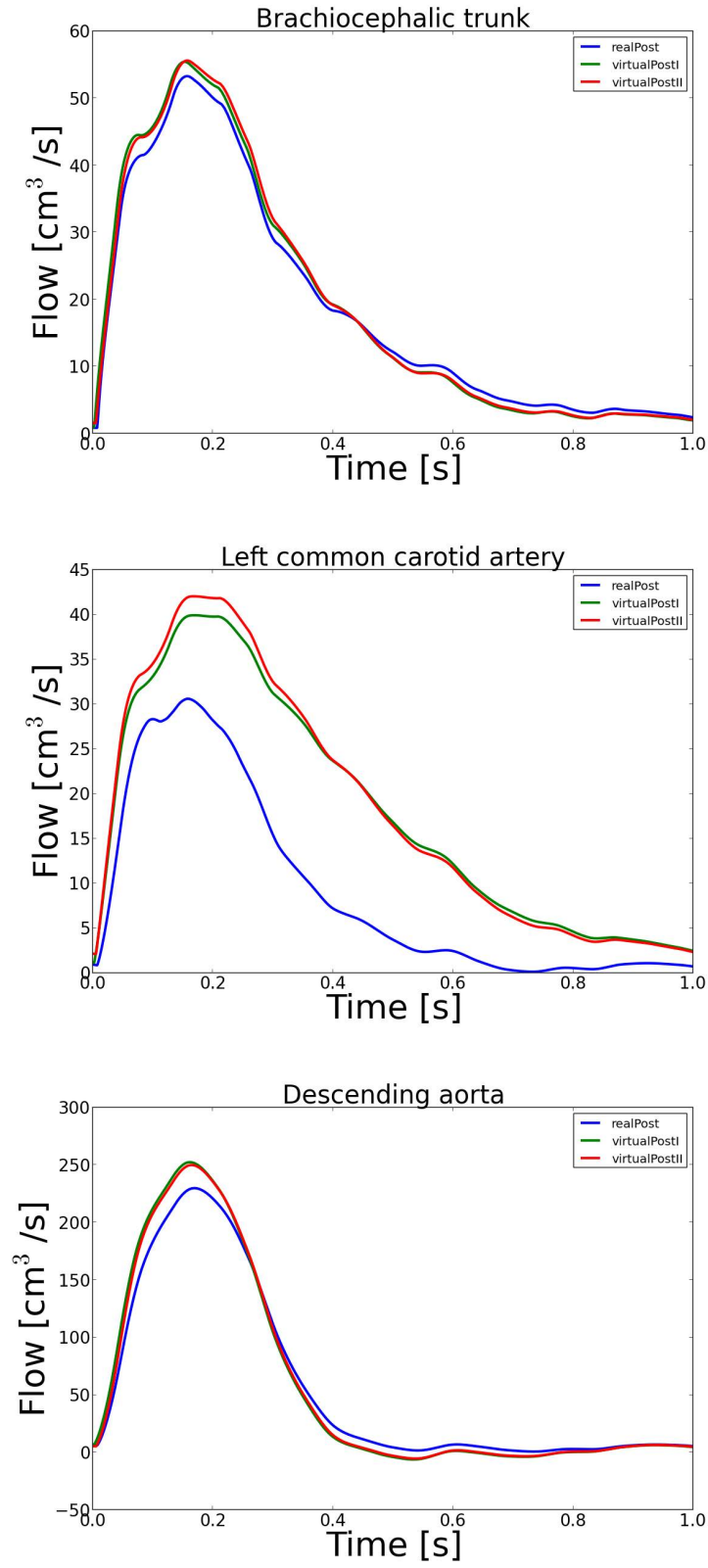
Figure A.11: Comparison of the numerical flows at different levels of the aortic arch for the three different models taken into account for the analysis (realPost, virtualPostI and virtualPostII). From top to bottom, flow profile in the brachiocephalic artery, left common carotid artery, and descending aorta.

A.3.4 CFD cases: pressure

In figure A.12 is depicted the pressure along the aorta at the systolic peak for the three cases under investigation. It is worth noting that at the level of the left common carotid artery a significant drop in pressure of 20 mmHg is induced in all the three cases analyzed. Instead the pressure all along the aortic arch is homogeneous except for the area were the aneurysm was located in which is possible to register a pressure drop of 5 mmHg. This drop is present particularly in the realPost case where it is enlightened a double drop in pressure one at each kink of the arch. This pressure behavior is notable in realPost and virtualPostII but not in virtualPostI that shows a smoother pattern.
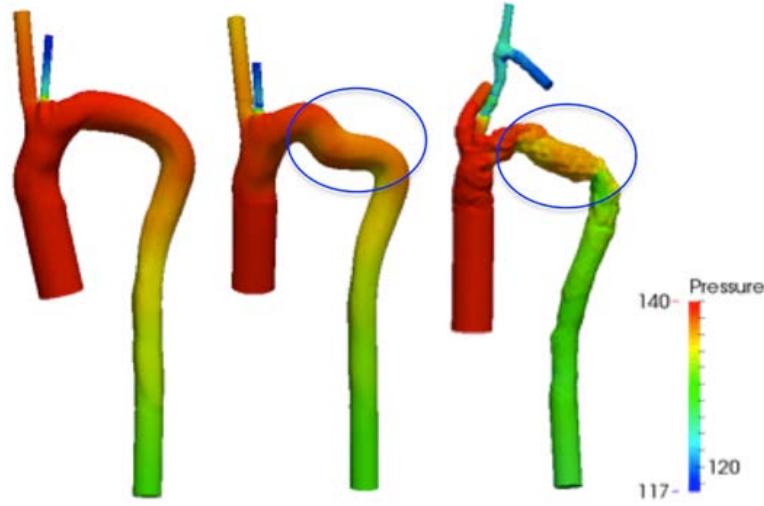
Figure A.12: Contour plot representing the distribution of blood pressure (mmHg) along the aorta in the three investigated cases at the systolic peak. We highlight the similar pattern both in virtualPostII and in realPost (blue circles).

A.3.5 CFD cases: wss

In figure 9 is depicted at t_{sys}, the wall shear stress distribution over the entire aorta (wss). This parameter is of arising clinical interest, we therefore report it briefly for sake of completeness. Figure A.13 shows a pattern of wss similar for virtualPostII and realPost. In fact, at section B and D virtualPostII and realPost have an increase of wss at the inferior part of the aorta. At section C, wss undergoes a decrease still at the inferior part of the aorta's wall. It is worth noting that realPost has a geometry that is superficially wrinkled, due to the stent-graft insertion in contact with the wall, this characteristic is influencing the CFD analysis inducing more noise at the computed quantities with respect to the virtual models.
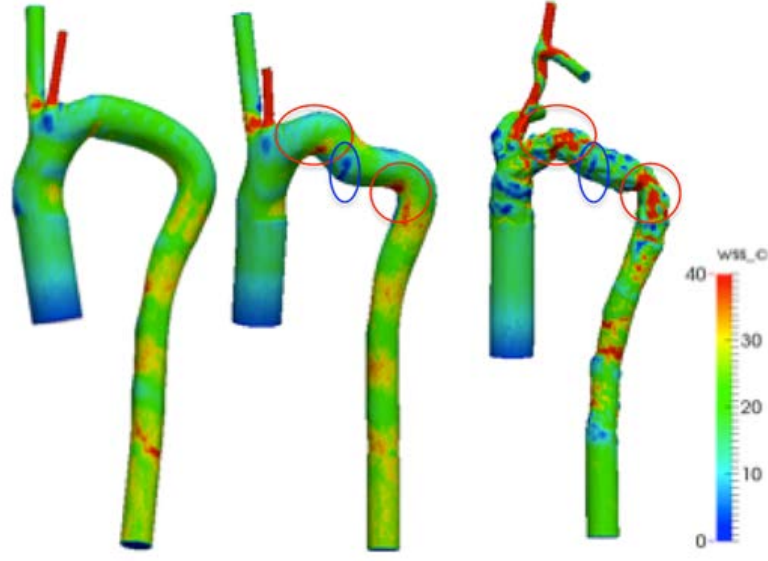
Figure A.13: Wall Shear Stress (wss) distribution along the aorta in the three investigated cases at the systolic peak. Red and blue circles highlight the remarkable patterns that occur both in virtualPostII and in realPost, more emphasized in realPost due to the wrinkled structure of the stent-graft.

A.4 Discussion

With this study we present a quantitative and qualitative comparison analysis of the aortic hemodynamic after virtual and real TEVAR. We analyse a single clinical case, focusing on a patient specific post-TEVAR geometrical model derived from medical image analysis and on two virtual post-TEVAR models created from pre-TEVAR images. We impose the boundary conditions already described in the section concerning simulation process and we observe the differences of the geometrical and numerical output of the two virtual models (virtualPostI and virtualPostII) in comparison with the real post-TEVAR model (realPost). The results of our analysis suggest interesting considerations especially between realPost and virtualPostII. In fact this work shows how virtual surgery could be a tool to sustain the decision making process in surgery procedure. Comparing the cases under investigation we saw in a way that, besides the more smooth pattern, pressure and velocity contours of virtual post-TEVAR models behave in a similar manner as the real post-TEVAR model does especially for the virtualPostII model compared to the realPost. Velocity contour at the sections A, B, C, and D shows the same pattern for realPost and virtualPostII. Also for pressure is observable a slight drop exactly in the same areas. It is worth noting that the more smoothed version virtualPostI lead also to a more smooth velocity and pressure dynamic. Need to be remarked that vessel area at the aforementioned sections is bigger in virtualPostI-II than in realPost, this has to be taken into account for the analysis of the results, that can be affected by this difference. It is remarkable also that, given same initial boundary

conditions, geometrical differences in general between the three models and in particular the geometrical differences present at the interface with the stent-graft, (see wrinkle surface in realPost model) may affect the simulation results not overall but locally at the scale of the stent-graft structures. Moreover the fact that CFD analysis has been carried on with inflow condition taken from the literature can explain high velocity values, further investigation are needed in this direction. At last, our findings are revealing the potential of numerical simulation in clinical practice in predicting aorta hemodynamic conditions after TEVAR. In fact this field of interest is growing with the aim to support daily clinical practice.

A.5 Limitations

The present study addresses a real clinical problem and is based on the analysis of geometrical and fluid-dynamics quantities performed on a patient specific 3D model. The restriction of the analysis to a unique case limits the generalization of the results especially to be exported to the clinical field. It is worth noting that this cases are so rare and complex that is difficult to collect a large amount of data and it is not straightforward to assembly all the necessary knowledge and group of interdisciplinary actors as clinicians and engineers/researchers. In any cases this study poses the bases to proceed in studying larger dataset. From the geometrical point of view, the 3D reconstructions obtained manipulating the pre-TEVAR patient-specific 3D model with dedicated computer tool is not reproducible in reality with surgical procedure and the virtual model is dramatically simplified with respect to the post-TEVAR patient-specific model. In fact the aortic curvature in the virtual model is smoother and do not reproduce the U-shaped curvature that the aneurysm introduces and that is maintained also after TEVAR. To avoid this problem, we also perform a 3D model using pre-TEVAR aorta centerline as guide to reconstruct the vessel without the aneurysm sac. Even though we reconstruct a more realistic 3D model (vrtualPostII), virtual procedure need to take into account the size of the stent-graft and other modification likely to be introduced by TEVAR surgery.

From the computational point of view, need to be said that patient under investigation underwent surgery two days after hospitalization, instead to obtain first results from a computational fluid dynamics simulation takes at least one week; computational time needs to be reduced in order to be really affective in this direction. Another relevant aspect to be further investigated is the validation of the proposed results with the use of patient-specific boundary conditions and the comparison of the results with the magnetic resonance images. Moreover a heavy limitation is that the simulations are carried out using rigid artery despite this is a common approach, a more accurate model would include the interaction of fluid and structure, but the computational costs would be significantly higher and the accuracy advantage questionable because the structural

model for the arterial wall (differently from the blood model given by the Navier-Stokes equations) is affected by several uncertainties.

As final remark, our computational tool is an *open* system, in other words it is not able to set itself taking into account the numerical output of the previous cardiac cycle and therefore to face changes that may arise at peripheral regions (Balossino et al., 2009). Hopefully such limitation will be addressed in future studies.

A.5.1   Conclusions

With this study we made a comprehensive investigation of the aortic geometry and hemodynamic for a specific, complex clinical case through patient-specific computational fluid dynamics. The post-TEVAR case has been investigated with literature boundary conditions and a comparison with virtual post-TEVAR scenarios has been performed. The numerical results suggest that the virtual scenarios can give a prediction of what effects of surgery could bring to the overall hemodynamics and morphology of the aorta. The tool addressed here can help surgeon during the clinical decision making process. Besides the clinical relevance of these specific findings, this study clearly demonstrates how CFD analyses allow observation of important flow effects resulting from the specificities of patient vessel geometries. Consequently, our results are reinforcing the potential impact of the translation of knowledge from computational biomechanics to clinical practice and vice-versa.

Appendix B

Definition of indexes used in the geometry quantification approach

B.1 1D Size Indexes

D_{max}: Maximum transverse diameter for all cross sections within the AAA sac.

$D_{neck,p}$: Proximal neck diameter immediately below the renal arteries.

$D_{neck,d}$: Distal neck diameter.

Arterial cross-sections are typically non-circular in shape, therefore the definition used for calculating D_{max}, $D_{neck,p}$, and $D_{neck,d}$ is the following:

$$D_i = \frac{4A_i}{P_i}$$

where A_i the cross-sectional area and P_i the perimeter of the same cross section.

H_{sac}: is the height of AAA sac. L_{sac}: the centerline length of AAA sac. H_{neck}: the height of AAA neck. L_{neck}: the centerline length of AAA neck. H_b: the bulge height. d_c: the distance between the lumen centroid and the centroid of the cross section where D_{max} is located.

B.2 2D Size Indexes

DH_r: The diameter–height ratio, an expression of the fusiform shape of the AAA sac.
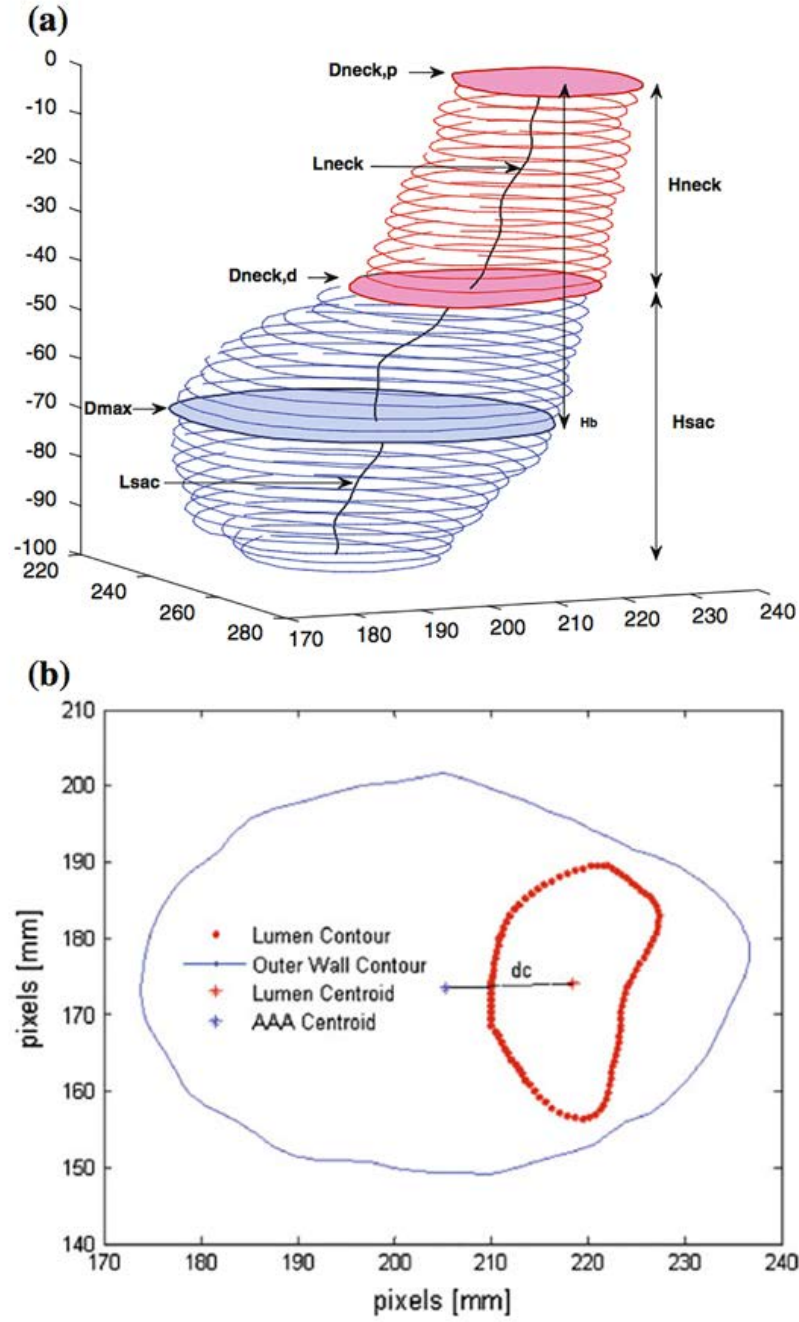
Figure B.1: (a) 1D size indices: D_{max}, $D_{neck,p}$, $D_{neck,d}$, H_{sac}, H_{neck}, L_{sac}, L_{neck}, H_b; (b) 1D size index d_c.

$$DH_r = \frac{D_{max}}{H_{neck} + H_{sac}}$$

DD_r: Diameter–diameter ratio.

$$DD_r = \frac{D_{max}}{D_{neck,p}}$$

H_r: Height ratio, an assessment of the relative neck height in comparison with the AAA height.

$$H_r = \frac{H_{neck}}{H_{neck} + +H_{sac}}$$

BL: Bulge location, provides a measure of the relative position of the maximum transverse dimension with respect to the neck.

$$BL = \frac{H_b}{H_{neck} + +H_{sac}}$$

β: Asymmetry factor.

$$\beta = 1 - \frac{d_c}{D_{max}}$$

T: Tortuosity.

$$T = 1 - \frac{L_{neck} + L_{sac}}{d}$$

where d is the Euclidean distance from the centroid of the cross section where $D_{neck,p}$ is located on the centroid of the cross section at the AAA distal end.

B.3   3D Size Indexes

V: Vessel volume.

S: Vessel surface area.

V_{ILT}: Volume of intraluminal thrombus contained within AAA sac.
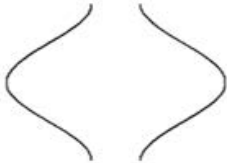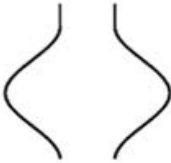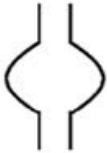
2D Shape Index	Low	High
DHr		
DDr		
Hr		
BL		
β		
T		

Figure B.2: Schema of 2D shape indexes providing an approximate measure to understand the AAA shape.

γ: Ratio of AAA ILT volume.

$$\gamma = \frac{V_{ILT}}{V}$$

B.4   3D Shape Indexes

IPR: Isoperimetric ratio.

$$IPR = \frac{S}{V^{2/3}} \tag{B.1}$$

NFI: Non-fusiform index.

$$NFI = \frac{SV^{2/3}}{S_{fusiform}V_{fusiform}^{2/3}} = \frac{IPR}{IPR_{fusiform}} \tag{B.2}$$

B.5   Second-Order Curvature-Based Indices

(Calculation Described in Detail in Martufi et al. (2009))

GAA: Area averaged Gaussian curvature.

$$GAA = \frac{\sum_{allelements} K_j S_j}{\sum_{allelements} S_j} \tag{B.3}$$

MAA: Area averaged Mean curvature.

$$MAA = \frac{\sum_{allelements} M_j S_j}{\sum_{allelements} S_j} \tag{B.4}$$

GLN: L2 norm of the Gaussian curvature.

$$GLN = \frac{1}{4\pi} \sqrt{\sum_{allelements} S_j \sum_{allelements} (K_j^2 S_j)} \tag{B.5}$$

MLN: L2 norm of the Mean curvature.

$$MLN = \frac{1}{4\pi} \sqrt{\sum_{allelements} (M_j^2 S_j)} \tag{B.6}$$

B.6   Wall Thickness Indices

$t_{w,min}$: Minimum wall thickness.

$t_{w,max}$: Maximum wall thickness.

$t_{w,ave}$: Average wall thickness.

Bibliography

Angenent, S., S. Haker, A. R. Tannenbaum, and R. Kikinis (1999). On the laplace–beltrami operator and brain surface flattening.

Antiga, L. (2002a). Patient-specific modeling of geometry and blood flow in large arteries. *Politecnico di Milano*.

Antiga, L. (2002b). *Patient-specific modeling of geometry and blood flow in large arteries.* Politecnico di Milano.

Antiga, L., B. Ene-Iordache, and A. Remuzzi (2003). Computational geometry for patient-specific reconstruction and meshing of blood vessels from mr and ct angiography. *Medical Imaging, IEEE Transactions on 22*(5), 674–684.

Antiga, L., M. Piccinelli, L. Botti, B. Ene-Iordache, A. Remuzzi, and D. A. Steinman (2008). An image-based modeling framework for patient-specific computational hemodynamics. *Medical & biological engineering & computing 46*(11), 1097–1112.

Antiga, L., D. Steinman, et al. (2004). Robust and objective decomposition and mapping of bifurcating vessels. *Medical Imaging, IEEE Transactions on 23*(6), 704–713.

Arko, F. R., E. H. Murphy, C. M. Davis, E. D. Johnson, S. T. Smith, and C. K. Zarins (2007). Dynamic geometry and wall thickness of the aortic neck of abdominal aortic aneurysms with intravascular ultrasonography. *Journal of vascular surgery 46*(5), 891–897.

Auricchio, F., M. Conti, A. Lefieux, S. Morganti, A. Reali, F. Sardanelli, F. Secchi, S. Trimarchi, and A. Veneziani (2014). Patient-specific analysis of post-operative aortic hemodynamics: a focus on thoracic endovascular repair (tevar). *Computational Mechanics 54*(4), 943–953.

Ayachit, U. (2015). The paraview guide: A parallel visualization application.

Balossino, R., G. Pennati, F. Migliavacca, L. Formaggia, A. Veneziani, M. Tuveri, and G. Dubini (2009). Computational models to predict stenosis growth in carotid arteries: Which is the role

of boundary conditions? *Computer methods in biomechanics and biomedical engineering 12*(1), 113–123.

Bankman, I. (2008). *Handbook of medical image processing and analysis*. academic press.

Bell, V., W. A. Mitchell, S. Sigurðsson, J. J. Westenberg, J. D. Gotal, A. A. Torjesen, T. Aspelund, L. J. Launer, A. de Roos, V. Gudnason, et al. (2014). Longitudinal and circumferential strain of the proximal aorta. *Journal of the American Heart Association 3*(6), e001536.

Bishop, R. L. (1975). There is more than one way to frame a curve. *American Mathematical Monthly*, 246–251.

Chan, T. F., L. Vese, et al. (2001). Active contours without edges. *Image processing, IEEE transactions on 10*(2), 266–277.

Cheng, S. W., E. S. Lam, G. S. Fung, P. Ho, A. C. Ting, and K. W. Chow (2008). A computational fluid dynamic study of stent graft remodeling after endovascular repair of thoracic aortic dissections. *Journal of vascular surgery 48*(2), 303–310.

Cheng, Z., C. Juli, N. Wood, R. Gibbs, and X. Xu (2014). Predicting flow in aortic dissection: Comparison of computational model with pc-mri velocity measurements. *Medical engineering & physics 36*(9), 1176–1184.

Choke, E., G. Cockerill, W. Wilson, S. Sayed, J. Dawson, I. Loftus, and M. Thompson (2005). A review of biological factors implicated in abdominal aortic aneurysm rupture. *European Journal of Vascular and Endovascular Surgery 30*(3), 227–244.

Chung, B. and J. R. Cebral (2015). Cfd for evaluation and treatment planning of aneurysms: Review of proposed clinical uses and their challenges. *Annals of biomedical engineering 43*(1), 122–138.

Cohen, L. D., E. Bardinet, and N. Ayache (1993). Surface reconstruction using active contour models.

Desai, N. D., K. Burtch, W. Moser, P. Moeller, W. Y. Szeto, A. Pochettino, E. Y. Woo, R. M. Fairman, and J. E. Bavaria (2012). Long-term comparison of thoracic endovascular aortic repair (tevar) to open surgery for the treatment of thoracic aortic aneurysms. *The Journal of thoracic and cardiovascular surgery 144*(3), 604–611.

Draney, M. T., F. R. Arko, M. T. Alley, M. Markl, R. J. Herfkens, N. J. Pelc, C. K. Zarins, and C. A. Taylor (2004). Quantification of vessel wall motion and cyclic strain using cine phase contrast mri: in vivo validation in the porcine aorta. *Magnetic resonance in medicine 52*(2), 286–295.

Erbel, R., V. Aboyans, C. Boileau, E. Bossone, R. Di Bartolomeo, H. Eggebrecht, A. Evangelista, V. Falk, H. Frank, O. Gaemperli, et al. (2014). 2014 esc guidelines on the diagnosis and treatment of aortic diseases. *European heart journal 35*(41), 2873–2926.

Faries, P. L., G. Agarwal, R. Lookstein, J. W. Bernheim, N. S. Cayne, H. Cadot, J. Goldman, K. C. Kent, L. H. Hollier, and M. L. Marin (2003). Use of cine magnetic resonance angiography in quantifying aneurysm pulsatility associated with endoleak. *Journal of vascular surgery 38*(4), 652–656.

Field, D. A. (1988). Laplacian smoothing and delaunay triangulations. *Communications in applied numerical methods 4*(6), 709–712.

Figueroa, C. A., C. A. Taylor, A. J. Chiou, V. Yeh, and C. K. Zarins (2009a). Magnitude and direction of pulsatile displacement forces acting on thoracic aortic endografts. *Journal of Endovascular Therapy 16*(3), 350–358.

Figueroa, C. A., C. A. Taylor, A. J. Chiou, V. Yeh, and C. K. Zarins (2009b). Magnitude and direction of pulsatile displacement forces acting on thoracic aortic endografts. *Journal of Endovascular Therapy 16*(3), 350–358.

Fihn, S. D., J. C. Blankenship, K. P. Alexander, J. A. Bittl, J. G. Byrne, B. J. Fletcher, G. C. Fonarow, R. A. Lange, G. N. Levine, T. M. Maddox, et al. (2014). 2014 acc/aha/aats/pcna/scai/sts focused update of the guideline for the diagnosis and management of patients with stable ischemic heart disease: a report of the american college of cardiology/american heart association task force on practice guidelines, and the american association for thoracic surgery, preventive cardiovascular nurses association, society for cardiovascular angiography and interventions, and society of thoracic surgeons. *Journal of the American College of Cardiology 64*(18), 1929–1949.

Fillinger, M. F., J. Racusin, R. K. Baker, J. L. Cronenwett, A. Teutelink, M. L. Schermerhorn, R. M. Zwolak, R. J. Powell, D. B. Walsh, and E. M. Rzucidlo (2004). Anatomic characteristics of ruptured abdominal aortic aneurysm on conventional ct scans: implications for rupture risk. *Journal of vascular surgery 39*(6), 1243–1252.

Fleischmann, D. and D. Miller (2007). Clinical 3d and 4d imaging and of the thoracic aorta. *Diseases of the Heart, Chest Breast: Diagnostic imaging and interventional techniques. Springer: Milan*, 119–30.

Flora, H. S., N. Woodhouse, S. Robson, and M. Adiseshiah (2001). Micromovements at the aortic aneurysm neck measured during open surgery with close-range photogrammetry: implications for aortic endografts. *Journal of Endovascular Therapy 8*(5), 511–520.

Ford, M., Y. Hoi, M. Piccinelli, L. Antiga, and D. Steinman (2014). An objective approach to digital removal of saccular aneurysms: technique and applications. *The British journal of radiology*.

Formaggia, L., A. Quarteroni, and A. Veneziani (2010). *Cardiovascular Mathematics: Modeling and simulation of the circulatory system*, Volume 1. Springer Science & Business Media.

Fung, G. S., S. Lam, S. W. Cheng, and K. Chow (2008). On stent-graft models in thoracic aortic endovascular repair: A computational investigation of the hemodynamic factors. *Computers in biology and medicine 38*(4), 484–489.

Ganten, M.-K., U. Krautter, H. von Tengg-Kobligk, D. Böckler, H. Schumacher, W. Stiller, S. Delorme, H.-U. Kauczor, G. W. Kauffmann, and M. Bock (2008). Quantification of aortic distensibility in abdominal aortic aneurysm using ecg-gated multi-detector computed tomography. *European radiology 18*(5), 966–973.

Giannoglou, G., G. Giannakoulas, J. Soulis, Y. Chatzizisis, T. Perdikides, N. Melas, G. Parcharidis, and G. Louridas (2006). Predicting the risk of rupture of abdominal aortic aneurysms by utilizing various geometrical parameters: revisiting the diameter criterion. *Angiology 57*(4), 487–494.

Grabenwöger, M., F. Alfonso, J. Bachet, R. Bonser, M. Czerny, H. Eggebrecht, A. Evangelista, R. Fattori, H. Jakob, L. Lönn, et al. (2012). Thoracic endovascular aortic repair (tevar) for the treatment of aortic diseases: a position statement from the european association for cardiothoracic surgery (eacts) and the european society of cardiology (esc), in collaboration with the european association of percutaneous cardiovascular interventions (eapci). *European Journal of Cardio-Thoracic Surgery*, ezs107.

Halier, S., S. Angenent, A. Tannenbaurn, and R. Kikinis (2000). Nondistorting flattening maps and the 3-d visualization of colon ct images. *Medical Imaging, IEEE Transactions on 19*(7), 665–670.

Hanson, A. J. and H. Ma (1995). Parallel transport approach to curve framing. *Indiana University, Techreports-TR425 11*, 3–7.

Kaladji, A., R. Spear, A. Hertault, J. Sobocinski, B. Maurel, and S. Haulon (2013). Centerline is not as accurate as outer curvature length to estimate thoracic endograft length. *European Journal of Vascular and Endovascular Surgery 46*(1), 82–86.

Kass, M., A. Witkin, and D. Terzopoulos (1988). Snakes: Active contour models. *International journal of computer vision 1*(4), 321–331.

Kim, H. J., I. E. Vignon-Clementel, C. A. Figueroa, J. F. LaDisa, K. E. Jansen, J. A. Feinstein, and C. A. Taylor (2009). On coupling a lumped parameter heart model and a three-dimensional finite element aorta model. *Annals of biomedical engineering 37*(11), 2153–2169.

Kleinstreuer, C., Z. Li, C. Basciano, S. Seelecke, and M. Farber (2008). Computational mechanics of nitinol stent grafts. *Journal of biomechanics 41*(11), 2370–2378.

Kühnel, W. (2006). *Differential geometry: curves-surfaces-manifolds*, Volume 16. American Mathematical Soc.

L. Ibanez, W. Schroeder, L. N. J. C. (2005). *The ITK software guide.* (2nd ed.). Kitware Inc.

Lam, S., G. S. Fung, S. W. Cheng, and K. Chow (2008). A computational study on the biomechanical factors related to stent-graft models in the thoracic aorta. *Medical & biological engineering & computing 46*(11), 1129–1138.

Leung, J., R. D. Nyilas, S. M. Ng, and X. Y. Xu. Towards a new geometric approach to assess the risk of rupture of abdominal aortic aneurysms using patient specific modelling. *Stress 10000*(5000), 5000.

Lindblad, B., N. Dias, M. Malina, K. Ivancev, T. Resch, F. Hansen, and B. Sonesson (2004). Pulsatile wall motion (pwm) measurements after endovascular abdominal aortic aneurysm exclusion are not useful in the classification of endoleak. *European journal of vascular and endovascular surgery 28*(6), 623–628.

Long, A., L. Rouet, A. Bissery, P. Rossignol, D. Mouradian, and M. Sapoval (2004). Compliance of abdominal aortic aneurysms: evaluation of tissue doppler imaging. *Ultrasound in medicine & biology 30*(9), 1099–1108.

Lorensen, W. E. and H. E. Cline (1987). Marching cubes: A high resolution 3d surface construction algorithm. In *ACM siggraph computer graphics*, Volume 21, pp. 163–169. ACM.

Malina, M., T. Länne, K. Ivancev, B. Lindblad, and J. Brunkwall (1998). Reduced pulsatile wall motion of abdominal aortic aneurysms after endovascular repair. *Journal of vascular surgery 27*(4), 624–631.

Martufi, G., E. S. Di Martino, C. H. Amon, S. C. Muluk, and E. A. Finol (2009). Three-dimensional geometrical characterization of abdominal aortic aneurysms: image-based wall thickness distribution. *Journal of biomechanical engineering 131*(6), 061015.

Midulla, M., R. Moreno, A. Baali, M. Chau, A. Negre-Salvayre, F. Nicoud, J.-P. Pruvo, S. Haulon, and H. Rousseau (2012). Haemodynamic imaging of thoracic stent-grafts by computational

fluid dynamics (cfd): presentation of a patient-specific method combining magnetic resonance imaging and numerical simulations. *European radiology 22*(10), 2094–2102.

Moore, J. E., C. Xu, S. Glagov, C. K. Zarins, and D. N. Ku (1994). Fluid wall shear stress measurements in a model of the human abdominal aorta: oscillatory behavior and relationship to atherosclerosis. *Atherosclerosis 110*(2), 225–240.

Morbiducci, U., R. Ponzini, G. Rizzo, M. Cadioli, A. Esposito, F. De Cobelli, A. Del Maschio, F. M. Montevecchi, and A. Redaelli (2009). In vivo quantification of helical blood flow in human aorta by time-resolved three-dimensional cine phase contrast magnetic resonance imaging. *Annals of biomedical engineering 37*(3), 516–531.

Morrison, T. M., G. Choi, C. K. Zarins, and C. A. Taylor (2009). Circumferential and longitudinal cyclic strain of the human thoracic aorta: age-related changes. *Journal of vascular surgery 49*(4), 1029–1036.

Muhs, B. E., A. Teutelink, M. Prokop, K. L. Vincken, F. L. Moll, and H. J. Verhagen (2006). Endovascular aneurysm repair alters renal artery movement: a preliminary evaluation using dynamic cta. *Journal of Endovascular Therapy 13*(4), 476–480.

Muhs, B. E., K. Vincken, J. Van Prehn, M. Stone, L. Bartels, M. Prokop, F. Moll, and H. Verhagen (2006). Dynamic cine-ct angiography for the evaluation of the thoracic aorta; insight in dynamic changes with implications for thoracic endograft treatment. *European journal of vascular and endovascular surgery 32*(5), 532–536.

Muhs, B. E., K. L. Vincken, A. Teutelink, E. L. Verhoeven, M. Prokop, F. L. Moll, and H. J. Verhagen (2008). Dynamic cine-computed tomography angiography imaging of standard and fenestrated endografts: differing effects on renal artery motion. *Vascular and endovascular surgery 42*(1), 25–31.

O'Flynn, P. M., G. O'Sullivan, and A. S. Pandit (2007). Methods for three-dimensional geometric characterization of the arterial vasculature. *Annals of biomedical engineering 35*(8), 1368–1381.

Pappu, S., A. Dardik, H. Tagare, and R. J. Gusberg (2008). Beyond fusiform and saccular: a novel quantitative tortuosity index may help classify aneurysm shape and predict aneurysm rupture potential. *Annals of vascular surgery 22*(1), 88–97.

Pedersen, E. M., S. Oyre, M. Agerbaek, I. Kristensen, S. Ringgaard, P. Boesiger, and W. Paaske (1999). Distribution of early atherosclerotic lesions in the human abdominal aorta correlates with wall shear stresses measuredin vivo. *European journal of vascular and endovascular surgery 18*(4), 328–333.

Perera, A. H., N. Rudarakanchana, M. Hamady, E. Kashef, M. Mireskandari, A. Uebing, N. J. Cheshire, and C. D. Bicknell (2014). New-generation stent grafts for endovascular management of thoracic pseudoaneurysms after aortic coarctation repair. *Journal of vascular surgery 60*(2), 330–336.

Piccinelli, M., A. Veneziani, D. Steinman, A. Remuzzi, L. Antiga, et al. (2009). A framework for geometric analysis of vascular structures: application to cerebral aneurysms. *Medical Imaging, IEEE Transactions on 28*(8), 1141–1155.

Raaz, U., A. M. Zöllner, I. N. Schellinger, R. Toh, F. Nakagami, M. Brandt, F. C. Emrich, Y. Kayama, S. Eken, M. Adam, et al. (2015). Segmental aortic stiffening contributes to experimental abdominal aortic aneurysm development. *Circulation*, CIRCULATIONAHA–114.

Redheuil, A., W.-C. Yu, C. O. Wu, E. Mousseaux, A. de Cesare, R. Yan, N. Kachenoura, D. Bluemke, and J. A. Lima (2010). Reduced ascending aortic strain and distensibility earliest manifestations of vascular aging in humans. *Hypertension 55*(2), 319–326.

Rengier, F., T. F. Weber, V. Henninger, D. Böckler, H. Schumacher, H.-U. Kauczor, and H. von Tengg-Kobligk (2012). Heartbeat-related distension and displacement of the thoracic aorta in healthy volunteers. *European journal of radiology 81*(1), 158–164.

Sacks, M. S., D. A. Vorp, M. Raghavan, M. P. Federle, and M. W. Webster (1999). In vivo three-dimensional surface geometry of abdominal aortic aneurysms. *Annals of biomedical engineering 27*(4), 469–479.

Sethian, J. A. (1999a). Fast marching methods. *SIAM Review 41*(2), 199–235.

Sethian, J. A. (1999b). *Level set methods and fast marching methods: evolving interfaces in computational geometry, fluid mechanics, computer vision, and materials science*, Volume 3. Cambridge university press.

Shum, J., G. Martufi, E. Di Martino, C. B. Washington, J. Grisafi, S. C. Muluk, and E. A. Finol (2011). Quantitative assessment of abdominal aortic aneurysm geometry. *Annals of biomedical engineering 39*(1), 277–286.

Shum, J., A. Xu, I. Chatnuntawech, and E. A. Finol (2011). A framework for the automatic generation of surface topologies for abdominal aortic aneurysm models. *Annals of biomedical engineering 39*(1), 249–259.

Steinman, D. A., J. S. Milner, C. J. Norley, S. P. Lownie, and D. W. Holdsworth (2003). Image-based computational simulation of flow dynamics in a giant intracranial aneurysm. *American Journal of Neuroradiology 24*(4), 559–566.

Suh, G.-Y., R. E. Beygui, D. Fleischmann, and C. P. Cheng (2014). Aortic arch vessel geometries and deformations in patients with thoracic aortic aneurysms and dissections. *Journal of Vascular and Interventional Radiology 25*(12), 1903–1911.

Taubin, G., T. Zhang, and G. Golub (1996). *Optimal surface smoothing as filter design.* Springer.

Taylor, C. A., T. J. Hughes, and C. K. Zarins (1998). Finite element modeling of three-dimensional pulsatile flow in the abdominal aorta: relevance to atherosclerosis. *Annals of biomedical engineering 26*(6), 975–987.

Teutelink, A., B. E. Muhs, K. L. Vincken, L. W. Bartels, S. A. Cornelissen, J. A. van Herwaarden, M. Prokop, F. L. Moll, and H. J. Verhagen (2007). Use of dynamic computed tomography to evaluate pre-and postoperative aortic changes in aaa patients undergoing endovascular aneurysm repair. *Journal of Endovascular Therapy 14*(1), 44–49.

Teutelink, A., A. Rutten, B. E. Muhs, M. Olree, J. A. Van Herwaarden, A. M. De Vos, M. Prokop, F. L. Moll, and H. J. Verhagen (2006). Pilot study of dynamic cine ct angiography for the evaluation of abdominal aortic aneurysms: implications for endograft treatment. *Journal of Endovascular Therapy 13*(2), 139–144.

Tolenaar, J. L., G. H. van Bogerijen, K. A. Eagle, and S. Trimarchi (2013). Update in the management of aortic dissection. *Current treatment options in cardiovascular medicine 15*(2), 200–213.

Tzilalis, V. D., D. Kamvysis, P. Panagou, I. Kaskarelis, M. K. Lazarides, T. Perdikides, P. Prassopoulos, and H. Boudoulas (2012). Increased pulse wave velocity and arterial hypertension in young patients with thoracic aortic endografts. *Annals of vascular surgery 26*(4), 462–467.

Upchurch, G. R. and T. A. Schaub (2006). Abdominal aortic aneurysm. *Am Fam Physician 73*(7), 1198–1204.

van Herwaarden, J. A., L. W. Bartels, B. E. Muhs, K. L. Vincken, M. Y. Lindeboom, A. Teutelink, F. L. Moll, and H. J. Verhagen (2006). Dynamic magnetic resonance angiography of the aneurysm neck: conformational changes during the cardiac cycle with possible consequences for endograft sizing and future design. *Journal of vascular surgery 44*(1), 22–28.

van Herwaarden, J. A., B. E. Muhs, K. L. Vincken, J. Van Prehn, A. Teutelink, L. W. Bartels, F. L. Moll, and H. J. Verhagen (2006). Aortic compliance following evar and the influence of different endografts: determination using dynamic mra. *Journal of Endovascular Therapy 13*(3), 406–414.

Van Keulen, J., J. Van Prehn, M. Prokop, F. Moll, and J. van Herwaarden (2009). Dynamics of the aorta before and after endovascular aneurysm repair: a systematic review. *European Journal of Vascular and Endovascular Surgery 38*(5), 586–596.

van Prehn, J., L. W. Bartels, G. Mestres, K. L. Vincken, M. Prokop, H. J. Verhagen, F. L. Moll, and J. A. van Herwaarden (2009). Dynamic aortic changes in patients with thoracic aortic aneurysms evaluated with electrocardiography-triggered computed tomographic angiography before and after thoracic endovascular aneurysm repair: preliminary results. *Annals of vascular surgery 23*(3), 291–297.

van Prehn, J., F. Schlösser, B. Muhs, H. Verhagen, F. Moll, and J. van Herwaarden (2009). Oversizing of aortic stent grafts for abdominal aneurysm repair: a systematic review of the benefits and risks. *European Journal of Vascular and Endovascular Surgery 38*(1), 42–53.

Van Prehn, J., K. Vincken, S. Sprinkhuizen, M. Viergever, J. Van Keulen, J. Van Herwaarden, F. Moll, and L. Bartels (2009). Aortic pulsatile distention in young healthy volunteers is asymmetric: analysis with ecg-gated mri. *European Journal of Vascular and Endovascular Surgery 37*(2), 168–174.

van Prehn, J., K. L. Vincken, B. E. Muhs, G. K. Barwegen, L. W. Bartels, M. Prokop, F. L. Moll, and H. J. Verhagen (2007). Toward endografting of the ascending aorta: insight into dynamics using dynamic cine-cta. *Journal of Endovascular Therapy 14*(4), 551–560.

Von Allmen, R., A. Anjum, and J. Powell (2013). Incidence of descending aortic pathology and evaluation of the impact of thoracic endovascular aortic repair: a population-based study in england and wales from 1999 to 2010. *European Journal of Vascular and Endovascular Surgery 45*(2), 154–159.

Vorp, D. A. (2007). Biomechanics of abdominal aortic aneurysm. *Journal of biomechanics 40*(9), 1887–1902.

Vorp, D. A., M. Raghavan, and M. W. Webster (1998). Mechanical wall stress in abdominal aortic aneurysm: influence of diameter and asymmetry. *Journal of Vascular Surgery 27*(4), 632–639.

Vos, A., W. Wisselink, J. Marcus, R. Manoliu, and J. Rauwerda (2002). Aortic aneurysm pulsatile wall motion imaged by cine mri: a tool to evaluate efficacy of endovascular aneurysm repair? *European journal of vascular and endovascular surgery 23*(2), 158–161.

Vos, A. F., W. Wisselink, J. T. Marcus, A. C. Vahl, R. A. Manoliu, and J. A. Rauwerda (2003). Cine mri assessment of aortic aneurysm dynamics before and after endovascular repair. *Journal of Endovascular Therapy 10*(3), 433–439.

W. Schroeder, K. Martin, B. L. (2005). *The visualization toolkit, an object oriented approach to 3D graphics.* (4th ed.). Kitware Inc.

Weber, T. F., M.-K. Ganten, D. Böckler, P. Geisbüsch, H.-U. Kauczor, and H. von Tengg-Kobligk (2009). Heartbeat-related displacement of the thoracic aorta in patients with chronic aortic dissection type b: quantification by dynamic cta. *European journal of radiology 72*(3), 483–488.

Weber, T. F., M.-K. Ganten, D. Böckler, P. Geisbüsch, A. Kopp-Schneider, H.-U. Kauczor, and H. von Tengg-Kobligk (2009). Assessment of thoracic aortic conformational changes by four-dimensional computed tomography angiography in patients with chronic aortic dissection type b. *European radiology 19*(1), 245–253.

Weber, T. F., T. Müller, A. Biesdorf, S. Wörz, F. Rengier, T. Heye, T. Holland-Letz, K. Rohr, H.-U. Kauczor, and H. von Tengg-Kobligk (2014). True four-dimensional analysis of thoracic aortic displacement and distension using model-based segmentation of computed tomography angiography. *The international journal of cardiovascular imaging 30*(1), 185–194.

White, G. H., J. May, R. Waugh, J. P. Harris, X. Chaufour, W. Yu, and M. S. Stephen (1999). Shortening of endografts during deployment in endovascular aaa repair. *Journal of endovascular surgery 6*(1), 4–10.

Wörz, S., H. von Tengg-Kobligk, V. Henninger, F. Rengier, H. Schumacher, D. Böckler, H.-U. Kauczor, and K. Rohr (2010). 3-d quantification of the aortic arch morphology in 3-d cta data for endovascular aortic repair. *Biomedical Engineering, IEEE Transactions on 57*(10), 2359–2368.

Ziou, D., S. Tabbone, et al. (1998). Edge detection techniques-an overview. *Pattern Recognition and Image Analysis C/C of Raspoznavaniye Obrazov I Analiz Izobrazhenii 8*, 537–559.